Universidad Politécnica de Madrid

Escuela Técnica Superior de
Ingenieros de Caminos, Canales y Puertos

Experimental and computational micromechanical study of fiber-reinforced polymers

Tesis doctoral

Luis Pablo Canal Casado
Licenciado en Ciencias Físicas
Ingeniero de Materiales

2011

Departamento de Ciencia de Materiales

Escuela Técnica Superior de Ingenieros de
Caminos, Canales y Puertos

Universidad Politécnica de Madrid

Experimental and computational micromechanical study of fiber-reinforced polymers

Tesis doctoral

Luis Pablo Canal Casado
Licenciado en Ciencias Físicas
Ingeniero de Materiales

Directores de la tesis

Carlos González Martínez
Dr. Ingeniero de Caminos, Canales y Puertos
Profesor Titular de Universidad

Javier Segurado Escudero
Dr. Ingeniero de Materiales
Profesor Titular de Universidad

2011

Contents

Agradecimientos

En primer lugar, quiero expresar mi sincero agradecimiento a mis directores de tesis, Javier Segurado y Carlos González, por las numerosas enseñanzas transmitidas durante el transcurso de esta tesis. A pesar de que a lo largo de este periodo sus obligaciones profesionales y personales se han visto sensiblemente incrementadas, siempre han sabido demostrar una plena dedicación, disponibilidad y proximidad.

Deseo agradecer a Javier LLorca la oportunidad de trabajar en el grupo de materiales compuestos, la orientación científica y su inestimable ayuda en la realización de este trabajo.

Este agradecimento debo extenderlo a todos y cada uno de los miembros del Departamento de Ciencia de Materiales, por su amabilidad y su ayuda en incontables ocasiones. Deseo mencionar y agradecer todos los buenos momentos compartidos con mis compañeros y amigos Joaquín, José Miguel, Bea, Borja, Álex, Els, Mónica, Fran, Gustavo, Elena y a muchos otros que he podido olvidar en esta lista, pero que también merecen estar. En especial, agradezco a David, Álvaro y Konstantina por su gran amistad, apoyo, consejo y mucha ayuda durante la realización de esta tesis.

Agradezco a Jon Molina, del Instituto IMDEA-Materiales, su gran colaboración para la realizar los ensayos in situ. En la misma institución quiero mencionar a Marcos y a Sergio por su ayuda con el nanoindentador y las simulaciones, pero sobre todo por su compañerismo y gran amistad.

Quiero mencionar también a todos los amigos fuera del ámbito laboral, por todo lo que hemos compartido durante estos años.

A mi familia por su apoyo en todo momento.

Resumen

Los materiales compuestos de matriz polimérica reforzados por fibras tienen propiedades mecánicas muy adecuadas para su utilización en aplicaciones estructurales. Estos materiales, debido a los altos valores de rigidez y resistencia específica, están desplazando a materiales convencionales en numerosas aplicaciones en las que se requiere la mejor relación entre las prestaciones mecánicas y el peso. Hoy en día, en el diseño de estructuras con materiales compuestos se utilizan criterios de fallo con base fenomenológica que requieren de un gran número de ensayos experimentales para obtener todos los parámetros del material necesarios y garantizar la seguridad de los componentes construidos. Este inconveniente en la aplicación de materiales compuestos se debe a la complejidad de su comportamiento mecánico, que está gobernado por diversos procesos que ocurren a nivel microscópico. Este es el caso, por ejemplo, de procesos como la concentración de tensiones y deformaciones, las decohesiones entre las distintas fases del compuesto o el fallo de los microconstituyentes, que determinan las propiedades finales del material.

En esta tesis se estudia la influencia de la microestructura y las propiedades de los microconstituyentes en el comportamiento mecánico en la dirección perpendicular al refuerzo de un laminado unidireccional de fibras de vidrio embebidas en una matriz epoxi. Las propiedades mecánicas de la matriz polimérica y de las intercaras fibra/matriz se caracterizaron mediante técnicas de nanoindentación y push-out, respectivamente. Los mecanismos de deformación y daño desarrollados en la microestructura del material compuesto se analizaron mediante la realización de ensayos mecánicos de compresión y flexión en tres puntos en el interior de un microscopio electrónico de barrido. Como resultado, se encontró que el daño del material com-

puesto sometido a cargas en la dirección perpendicular al refuerzo comenzaba en las intercaras fibra/matriz y se propagaba a través de la unión de las intercaras dañadas mediante la rotura de los ligamentos de matriz entre fibras decohesionadas.

El comportamiento mecánico del laminado hasta rotura se modeló mediante la simulación por elementos finitos de modelos micromecánicos que representaban la microestructura real del material. Siguiendo las observaciones experimentales, el modelo numérico incluía la decohesión de las intercaras y la rotura de la matriz. Los resultados de las simulaciones mostraron un buen acuerdo con los experimentos tanto en su respuesta macroscópica como en los mecanismos de deformación y daño microscópicos.

El modelo numérico desarrollado sirvió para obtener la envolvente de fallo del material compuesto bajo cargas normales en la dirección perpendicular al refuerzo y cortante fuera de plano. Los resultados obtenidos de las simulaciones se compararon con las predicciones de los criterios de Hashin y Puck para el fallo de laminados.

Abstract

Fiber-reinforced polymers (FRPs) exhibit outstanding mechanical properties, ideal for their use in structural applications. Due to the high specific values of stiffness and strength, these composites are replacing conventional materials in applications where a superior mechanical performance in combination with weight saving is necessary. However, the lack of reliable and experimentally contrasted models to accurately predict the failure strength of FRPs makes the optimization process of composite structures to be carried out by means of a costly and time-consuming trial-and-error approach, which requires an immense burden of testing and restricts the promising improvements of the use of composites. This difficulty in the simulation of mechanical behavior and damage of composites is due to the fact that an accurate model should account for the phenomena which take place at the micron scale, which is in the size of the reinforcement. This is the case, for instance, of the stress and strain concentration, decohesion of the reinforcement and damage of the material constituents.

This thesis studies the influence of the microstructure and the properties of the microconstituents in the mechanical behavior of a unidirectional laminate of glass fiber embedded in a matrix of epoxy resin, for the transverse loading cases. To this end, the mechanical properties of the polymeric matrix and the fiber/matrix interfaces have been experimentally characterized by means of nanoindentation and push-out techniques, respectively. The deformation and damage mechanisms developed in the microstructure of the composite have been analyzed through compression and three-point bending tests carried out inside the scanning electron microscope. It was found that the damage process began by the decohesion of the fiber/matrix interfaces,

and continues with the subsequent propagation of the damage by the link up of the interface fractures by breaking the matrix ligaments between debonded fibers.

The mechanical behavior of the unidirectional laminate until final fracture was modeled by the finite element simulation of micromechanical models which represented the microstructure of the real material. Following the previous experimental observation, the interface decohesion and the failure of the matrix were included in the computational model. The simulation results were in very good agreement with the experiments in terms of the macroscopic response and of the microscopic mechanisms.

Finally, the numerical model was also employed to obtain the failure envelope of the composite under transverse loads and out-of-plane shear. The model results were assessed with the predictions of the Hashin and Puck's crieria for the failure of laminate.

Chapter 1

Introduction

1.1 Background

Composite materials are created by the combination of two or more different constituents or phases which remain separate and distinct within the composite microstructure. The combination of the different mechanical properties of each individual constituent brings the opportunity to tailor a specific material with the required properties for a given application. For this reason, composite materials are playing nowadays an increasing role in technological industries such as aerospace, automobile, construction, energy or biomedical. It is possible to find good examples of technological applications with ceramic matrix and metal matrix composites in cutting tools, armors for military vehicles, disc brakes for sport cars or gas turbine components. However, among all the high performance composite materials, fiber-reinforced polymers (FRPs) are the most extensively used for lightweight structural applications.

FRPs are made by a polymeric matrix reinforced with high performance fibers (carbon, glass, aramid, PBO, etc). The fibers can be weaved, knitted or braided to created a textile sheet which make easier the composite manufacturing. However, for high strength applications, structures are assembled from thin plies of unidirectional fibers which have been pre-impregnated with the polymeric matrix. The individual plies are successively laid down, creating a laminate. Each ply can be oriented to tailor a specific laminate to fulfill the design requirements. The fibers are the load-

bearing phase, while the matrix is mainly used to maintain the fibers oriented in the design direction. Due to their outstanding specific mechanical properties and the mature level of the processing and quality control techniques, FRPs are extensively used nowadays in structural applications where weight saving is a mandatory requirement. Good examples of the FRPs applications can be found in the aerospace industry: the A380, the last civil Airbus aircraft, contains up to 25% in weight of composite materials (used for wings, fuselage sections and tail surfaces) or the Boeing 787 Dreamliner which claims to be the first airliner with a fully composite fuselage manufactured with advanced carbon components technologies. Nowadays, engineers have excellent tools for predicting the load distribution throughout the structure when the material behavior is linear-elastic, but predictions become problematic once damage begins. The fundamental difficulty is that damage in these engineering materials involves extremely complicated nonlinear processes acting at different scales, from the atomic to the structure level.

The standard strategy to tackle the failure predictions in FRPs starts from a numerical analysis of the whole structure in a *top-bottom* approach. This initial evaluation identifies hot spots in which damage is likely to occur, and these regions are subjected to further refined analysis. Nonlinear constitutive models based on phenomenological approaches are used to predict the material behavior until fracture. Although this strategy focuses on engineering necessities, it has also important limitations. An extensive experience and costly testing campaigns are necessary to calibrate these models employed in the critical regions. Innovations in materials are limited because of the lack of reliable data to assess the onset and propagation of damage upon loading. And finally, the extrapolation of current knowledge to different loading/environmental conditions is problematic due to the phenomenological nature of the models.

Recent developments in multiscale simulations, together with increased computational power and improvements in modeling tools, are enabling an alternative strategy that overcomes the limitations of the *top-bottom* approach. Nowadays, it is beginning to be possible to predict accurately, and without adjustable parameters, the behavior until failure of composite coupon specimens and simple components. This strategy, a

new hierarchical, *bottom-up* approach is being developed to carry out virtual tests of composite materials and structures (LLorca and González, 2011). The overall multiscale simulation scheme is depicted in Fig.1.1 and takes advantage from the fact that composite structures are made up of laminates which in turn are obtained by stacking individual plies with different fiber orientation. This leads to three different entities (ply, laminate and component) whose mechanical behavior is characterized by three different length scales, namely fiber diameter, ply and laminate thickness, respectively. Fiber diameters are of the order of 5-20 μm, while ply thicknesses are in the range 100-300 μm and standard laminates are several mm in thickness and above. This clear separation of length scales is very useful to carry out multiscale modeling by computing the properties of one entity (e.g. individual plies) at the relevant length scale, homogenizing the results into a constitutive model, and passing this information to the simulations at the next length scale to determine the mechanical behavior of the larger entity (e.g. laminate). Thus, multiscale modeling is carried out through the transfer of information between different length scales rather than by coupling different simulation techniques.

Virtual testing of composites up to the component level is thus carried out in three successive steps within the framework of the finite element method, assuming that continuum mechanics describes the behavior even for the smaller scales. In the first one, computational micromechanics is used to predict the ply properties from the thermo-mechanical properties of the constituents (fiber, matrix and interfaces), together with the volume fraction and spatial distribution of the fibers within an individual ply. Fiber properties (stiffness, strength, coefficients of thermal expansion) are usually provided by the fiber manufacturer, which carries out a thorough characterization of the fiber properties as part of the optimization process. On the contrary, matrix and interface properties depend on the consolidation process (time, pressure and temperature, effect of fiber dispersion) and have to be characterized in situ by means of nanomechanics. Starting from the homogenized ply properties and information about the laminate lay-up as well as the interply behavior, computational mesomechanics is then used to determine the homogenized behavior of laminates.

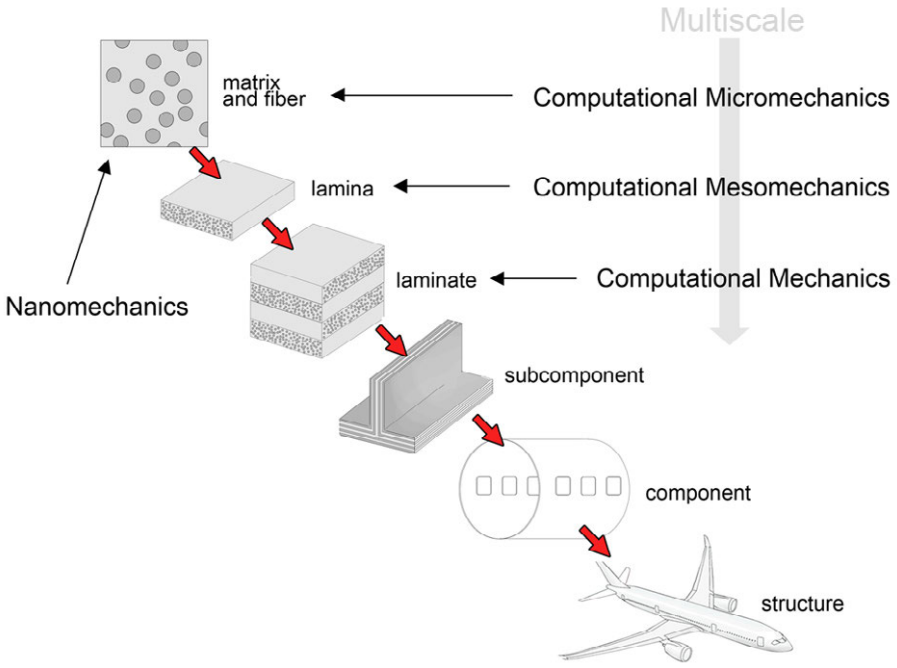

Figure 1.1: Multiscale bottom-up simulation strategy to carry out virtual mechanical tests of composite materials and structures.

These results are finally used within the framework of computational mechanics to obtain the response until fracture of structural components made of composites.

1.2 Damage mechanisms in FRPs

Most structural materials present one dominant physical failure process upon deformation (e.g., void nucleation, growth and coalescence in ductile metals or shear bands formation in polymers) and the simulation of failure only has to include this micromechanism. On the contrary, FRPs present several different physical failure mechanisms and the dominant one depends on the loading conditions (see Fig. 1.2 for unidirectional composites). Fracture due to tensile stresses parallel to the fibers is controlled by the tensile fracture of the fibers, while compressive stresses along the fibers lead to fracture by fiber kinking in compression, a mechanism which mainly depends on the fiber misorientation and the matrix shear strength. Tensile fracture perpendicular to the fibers is brittle and controlled by the fracture of the polymeric matrix and of the fiber-matrix interface, while fracture caused by compressive stresses perpendicular to the fibers or by shear is accompanied by large deformations as a result of the non-linear response of the matrix when subjected to compression and/or shear. Finally, interply delamination is another typical failure mechanism in FRPs due to the thermo-elastic mismatch between adjacent plies with different orientation. Hence, accurate models of fracture of FRPs have to include all these micromechanisms and the complex interaction among them because they coexist in the same laminate subjected to one type of load as a result of the different orientation of the fibers in each ply (Fig. 1.3). For instance, intraply matrix cracks (which propagate parallel to the fibers) are very often the origin of interply delaminations (Fig. 1.3), while it is well known that the compressive strength parallel to the fibers is severely reduced in the presence of shear stresses.

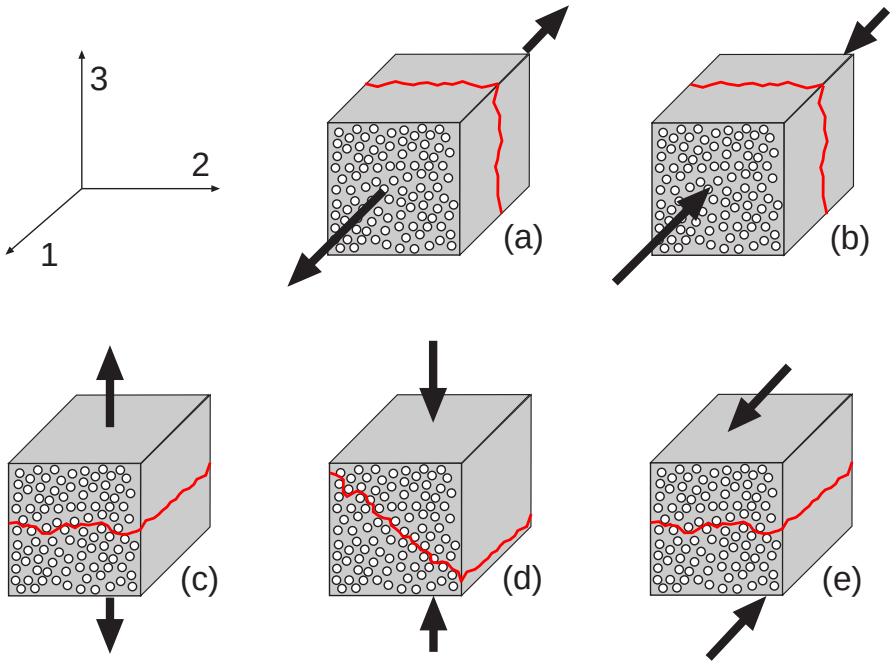

Figure 1.2: Diagram of the different failure micromechanisms in FRPs as a function of the loading conditions. (a) Longitudinal tension. (b) Longitudinal compression. (c) Transverse tension. (d) Transverse compression. (e) Longitudinal shear.

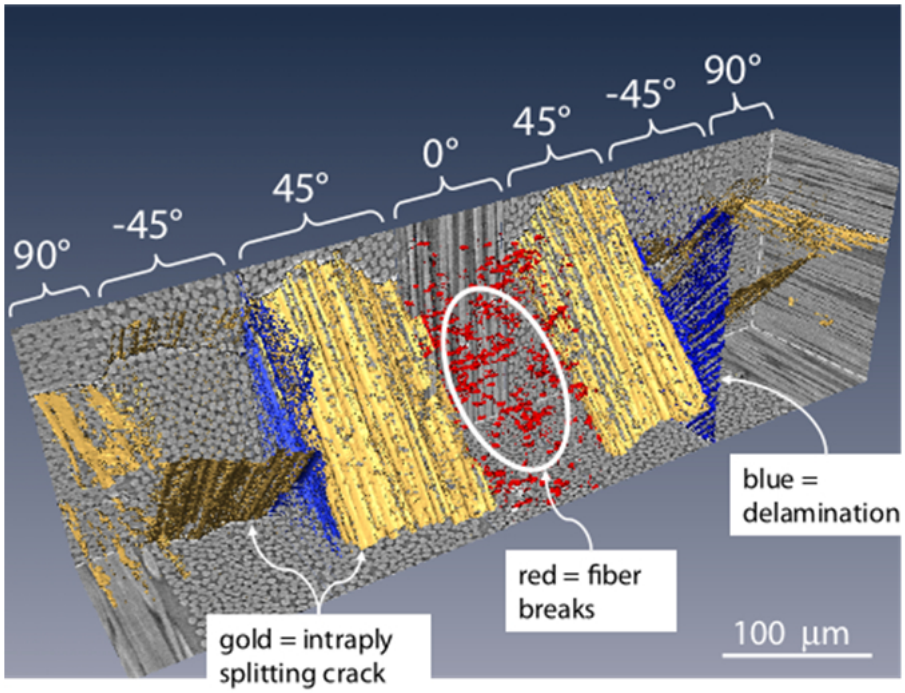

Figure 1.3: X-ray computed tomography showing different failure micromechanisms in a $[90/-45/45/0/45/-45/90]$ composite laminate loaded in tension parallel to the plies with fibers oriented at 0°. Fiber fracture is dominant in the 0° plies, while matrix cracking parallel to the fibers dictates the failure of the 90° and 45° plies. In addition, matrix cracks led to interface delamination between 45° and −45° plies. Adapted from Wright et al. (2008).

1.3 Failure criteria in FRPs

The failure criteria for composites are often used just in the initial calculations to size a component. Beyond that point, experimental tests on coupons or structural elements are required to determine the global design allowables. In order to reduce the manufacturing time and the costs of new components, there is a need to establish the level of confidence in the methods for failure prediction of FRPs. To this end,Hinton et al. (2004) carried out the worldwide failure exercise (WWFE), assessing nineteen different theoretical approaches for predicting the deformation and failure response of FRPs. The experimental results for the strength of the FRPs subjected to complex stress states showed significant differences with the predictions of many theories, even when analyzing simple laminates.

Failure in composite structures is commonly predicted through phenomenologically based failure criteria implemented in the finite element analysis of the structure. Hashin (1980) was the pioneer in the identification of the different failure mechanisms in unidirectional laminates and incorporate them separately in a piecewise smooth failure surface. Two different mechanisms were considered, one related to the fiber failure and the other to the matrix failure. The criteria assumed a quadratic interaction between tractions acting on the plane of failure (Fig. 1.4). However, Hashin's model was not able to determine the actual orientation of the fracture plane. For this reason, the criteria did not capture the experimental results in the case of matrix and fiber compression.

Puck and Schürmann (2002) proposed modifications to Hashin's model to improve its predictive capabilities. The key element of Puck's criteria is the calculation of the angle of the fracture plane in the case of matrix failure modes. Thus, transverse tension loads produce a fracture in a plane which is normal to the loading direction and parallel to the fibers. Meanwhile, transverse compression stresses produce a fracture plane in an angle which varies between 38° and 55°, depending on the in-plane shear (Fig.1.5).

Puck's predictions correlated very well with the experimental assessments in the WWFE. However, these criteria use several non-physical parameters which can be difficult to quantify without considerable experience in a particular material. To

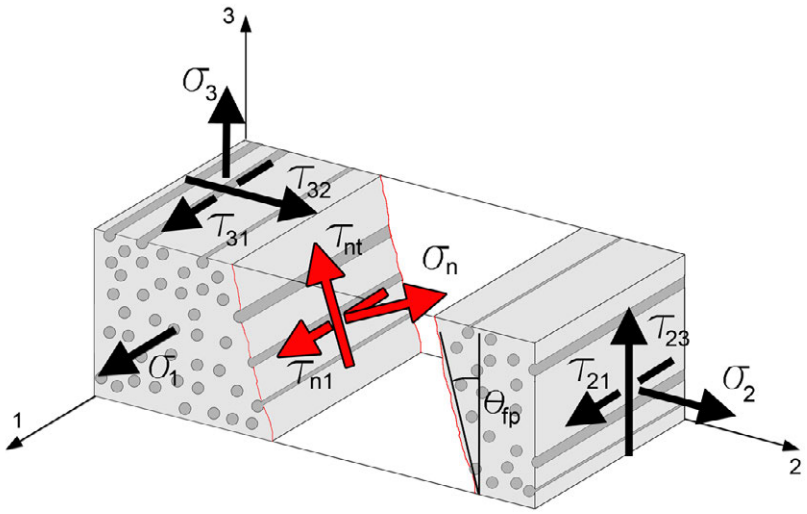

Figure 1.4: Three-dimensional stresses on a UD composite element. The (1,2,3) coordinate system is fixed to fiber direction (1), laminate (2) and thickness direction (3). The (1,n,t) coordinate system is rotated by the fracture angle θ_{fp}, from the (2) direction to the (n) direction which is normal to the fracture plane.

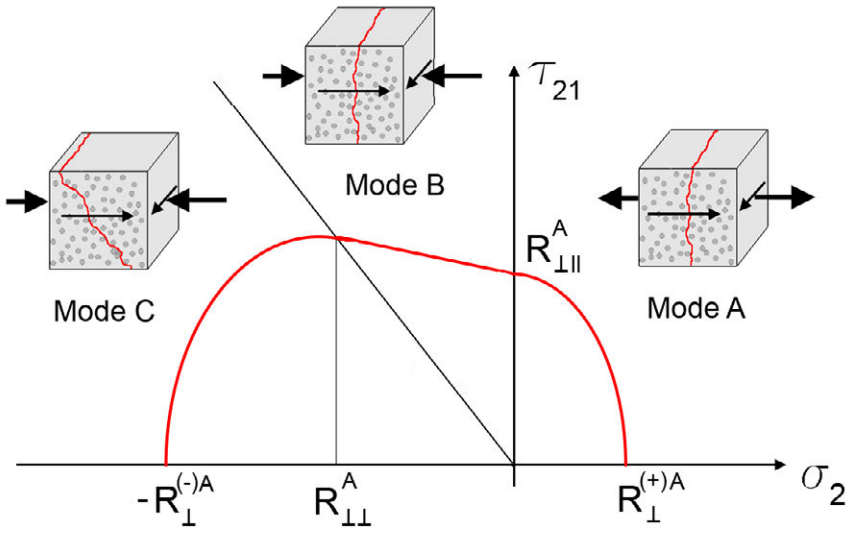

Figure 1.5: Predictive failure curve derived from Puck's criterion for the matrix failure modes and their fracture angles.

overcome this drawback, Dávila et al. (2005) proposed a non-empirical set of failure criteria, denoted as LaRC03. It was based on the fracture mechanics analysis of cracked plies (Dvorak and Laws, 1987) and Puck's action plane concept. The experimental assessment of the LaRC03 criteria showed a significant improvement over the commonly used Hashin's criteria, but it also fails to follow some experimental results. This fact indicates that the existing knowledge on failure mechanisms of FRPs needs further development.

1.4 Micromechanical models of composite materials

The main objective of the micromechanics of composite materials is the prediction of the effective or macroscopical properties (elastic modulus, strength, thermal expansion coefficient, etc) from the mechanical properties of its constituents and their distribution inside the material.

The relation between the constituents and the effective properties of the material can be obtained by studying the microstructure at different length scales. In metals, ceramics, polymers and other homogeneous materials, the deformation mechanisms usually involve micro- and nanometric level processes. Thus, their mechanical behavior can be obtained through detailed models of atomic and molecular processes by means of quantum mechanics and molecular dynamics. However, in FRPs the deformation and fracture processes take place at a scale of microns, and at this microscopic level, the composite constituents can be considered as continuum media and their behavior are described by continuum mechanics.

Besides the prediction of the effective properties of the composite, the micromechanical models have different applications. They can also be used to obtain constitutive equations to simulate, in the framework of computational mechanics, the behavior of structural components, and to study the damage evolution within the composite microstructure.

The micromechanical study of composites is a complex task and is necessary to

employ some approximations. Thus, micromechanical methods can be classified on the basis of these assumptions (Böhm, 1998)

- Analytical methods
  - Mean field approach
  - Variational bounding method
- Computational methods
  - Periodic microfield approach
  - Embedded cell method

Homogenization and variational bounding methods are well-established, accurate theories to compute analytically the overall or *effective* properties of inhomogeneous materials in the elastic regime (Nemat-Nasser and Hori, 1999; Torquato, 2001). Additionally, they often provide solutions for the constitutive equation of these materials, which can be included as materials models in structural analysis codes to assess the mechanical response of components. Nevertheless, the extension to the non-linear regime is more complex and the accuracy of the results is not always guaranteed (Castañeda and Suquet, 1998). These limitations have been overcome with the rapid development of computational micromechanics in the last decade. The high computational cost of the periodic and embedded cell methods can still be a major drawback, but this cost has been reduced by the increasing power of the digital computers and the robustness of the finite elements codes. The different micromechanical approaches are briefly discussed in the next sections.

1.5 Analytical micromechanics

1.5.1 Mean field approaches

These models consider that the stress and strain fields within each constituent of an inhomogeneous material can be approximated by their volumetric phase averages,

$\bar{\boldsymbol{\epsilon}}_m$ and $\bar{\boldsymbol{\sigma}}_m$ for the matrix and $\bar{\boldsymbol{\epsilon}}_r$ and $\bar{\boldsymbol{\sigma}}_r$ for the reinforcement. Considering V_m and V_r as the volume occupied by the matrix and reinforcement, respectively. The volumetric phase averages can be calculated as

$$\begin{aligned} \bar{\boldsymbol{\sigma}}_m &= \frac{1}{V_m}\int_{V_m} \boldsymbol{\sigma}_m(\mathbf{x})dV \quad \text{and} \quad \bar{\boldsymbol{\epsilon}}_m = \frac{1}{V_m}\int_{V_m} \boldsymbol{\epsilon}_m(\mathbf{x})dV \\ \bar{\boldsymbol{\sigma}}_r &= \frac{1}{V_r}\int_{V_r} \boldsymbol{\sigma}_r(\mathbf{x})dV \quad \text{and} \quad \bar{\boldsymbol{\epsilon}}_r = \frac{1}{V_r}\int_{V_r} \boldsymbol{\epsilon}_r(\mathbf{x})dV \end{aligned} \tag{1.1}$$

where $V_m + V_r = V$ is the representative volume of the inhomogeneous material and $\mathbf{x}$ is the vector which indicates the position of a material point.

Considering the matrix and the reinforcement phases as elastic solids, the relation between the averages stresses and strains can be described as,

$$\bar{\boldsymbol{\sigma}}_m = L_m\bar{\boldsymbol{\epsilon}}_m \text{ and } \bar{\boldsymbol{\sigma}}_r = L_r\bar{\boldsymbol{\epsilon}}_r \tag{1.2}$$

being L_m and L_r the fourth order stiffness elastic tensors for each constituent phase.

The homogenization relations provide the effective or overall fields from the averaged strains and stress of each phase,

$$\bar{\boldsymbol{\sigma}} = (1-\xi)\bar{\boldsymbol{\sigma}}_m + \xi\bar{\boldsymbol{\sigma}}_r \text{ and } \bar{\boldsymbol{\epsilon}} = (1-\xi)\bar{\boldsymbol{\epsilon}}_m + \xi\bar{\boldsymbol{\epsilon}}_r \tag{1.3}$$

where ξ stands for the volume fraction of the reinforcement.

The phase averaged strains and stresses can be related to the effective fields through their corresponding concentration tensors, $\mathbf{A}$ and $\mathbf{B}$, referred to the phase stress and strain concentration tensors, respectively.

$$\bar{\boldsymbol{\sigma}}_m = \mathbf{B}_m\bar{\boldsymbol{\sigma}} \quad \text{and} \quad \bar{\boldsymbol{\epsilon}}_m = \mathbf{A}_m\bar{\boldsymbol{\epsilon}} \tag{1.4}$$

$$\bar{\boldsymbol{\sigma}}_r = \mathbf{B}_r\bar{\boldsymbol{\sigma}} \quad \text{and} \quad \bar{\boldsymbol{\epsilon}}_r = \mathbf{A}_r\bar{\boldsymbol{\epsilon}} \tag{1.5}$$

The concentration tensors should fulfill the relations

$$(1-\xi)\mathbf{A}_m + \xi\mathbf{A}_r = I \text{ and } (1-\xi)\mathbf{B}_m + \xi\mathbf{B}_r = I \tag{1.6}$$

where I is the fourth-rank identity tensor. The effective elastic properties of the composite is directly linked with the properties of the phases and one of the four

concentration tensors. Therefore, the elastic problem is reduced to obtain a concentration tensor as a function of the composite microstructure and the phase properties. These methods have been highly successful in describing the elastic response of inhomogeneous materials (Eshelby, 1957; Mori and Tanaka, 1973; Kroner, 1958). Their use for modeling nonlinear composites is nowadays a subject of active research (Castañeda, 1991; Pettermann et al., 1999; González and LLorca, 2000; López-Pamiés and Ponte-Castañeda, 2006).

1.5.2 Variational bounding methods

These methods use variational principles to obtain upper and lower bounds on the overall elastic and physical properties of inhomogeneous materials. Bounds are important tools for assessing other micromechanical approaches. Furthermore, in many cases one of the bounds provides by itself good estimates for the physical property under consideration. The uniform stress and strain conditions lead to the simplest variational bounding expressions, the upper bounds of Voigt (1889) and the lower bounds of Reuss (1929), which are also known as the Hill bounds (Hill, 1952). These limits are very easy to calculate, but they are also too slack to provide good predictions since the only information regarding to the microstructure is the volume fraction of reinforcement. Further developments in this technique have obtained more accurate bounds which offer good predictive capabilities when additional information of the microstructure is included (Hashin and Shtrikman, 1963; Torquato, 1991).

1.6 Computational micromechanics

1.6.1 Periodic microfield approaches

In these methods, the inhomogeneous material is approximated by an infinitely model made by a periodic phase arrangement. The resulting periodic microfields are evaluated by analyzing the repeating cells of the microstructure describing microgeometries ranging from rather simplistic to highly complex representations of the real microstructure of the composite. Periodic microfield approaches are often used to

obtain constitutive equations for composite materials in the non-linear range. The resolution at the microscale provided by this approach can be also useful for studying the onset and progression of damage within the microstructure (Totry et al., 2008a,b; Canal et al., 2009).

Several strategies have been developed to handle the analysis of heterogeneous materials at the microlevel. The pioneer approach was the Method of cells (Aboudi, 1997). In this proposal, an analytical approximation is used to obtain the stress and strain fields in a microstructure that corresponds to a square arrangement of fibers. Another examples of analytical methods to solve the unit cell problem are the Transformation field analysis (Dvorak, 1992) or the High-fidelity generalized methods of cells (Aboudi, 2004). Although these analytical approximations use highly idealized microstructures and provide limited information of the microscopic fields, they can be used to obtain constitutive models with low computational cost, which is mandatory for the mechanical analysis of large composite structures. Besides the previous simplistic approximations, the analysis of composites through periodic microfield approaches is usually tackled with more complex and realistic cells which are solved by numerical tools such as the finite differences and the finite elements method.

Representative volume element

The mechanical behavior of composite materials can be studied through the finite elements simulation of a representative volume element (RVE) of the microstructure. The RVE was defined by Drugan and Willis (1996) as the smallest material volume element of an heterogeneous material for which the average stress and strain microfields converge to an asymptotically constant value which is size independent and represents the effective macroscopic constitutive response. Therefore, the RVE should exceed a minimum size to ensure that the simulation results are independent of the size and the spatial distribution of the reinforcements within the microstructe. There are no procedures to predict the size of the RVE for the analysis of a particular composite, but it should be confirmed by *a posteriori* assessment of the statistical error. The size of the RVE is usually an important drawback for this kind of simulations. If a large size of the RVE were needed to represent the composite, it would

make impossible to perform the numerical computation. Fortunately, it was demonstrated that only a few dozens of fibers or particles should be included in a RVE to simulate accurately the mechanical behavior of metal matrix composites and FRPs in elasto-plastic regime (Eckschlager et al., 2002; Segurado et al., 2003; Totry et al., 2010).

Microstructure generation

In the multiparticle cell models, the computational micromechanical process to simulate the behavior of composites begins with the creation of a RVE, which is is usually taken as a cubic cell of side L. The microstructure of a composite is idealized as a dispersion of spheres, ellipsoids, fibers, cubes or any other geometrical entity which represents the shape of the inclusions.

To analyze the transverse behavior of unidirectional FRPs, assuming infinitely long fibers, the microstructure can be idealized as a dispersion of circles of radius r which represent the section of the fibers. This fiber distribution should be representative of the actual transverse section microstructure of the studied material (Totry et al., 2010, 2009), many different methodologies have been proposed to attain this goal. Thus, there are techniques based on the replication of the images of the microstructure (Trias, 2005), on the reproduction of statistical spatial descriptors (t. J. Vaughan, 2011) or a direct technique which generates an idealized isotropic and random microstructure (Segurado and LLorca, 2002). The later technique was employed in this work to generate artificial microstructures of the FRPs, and the description of this method is given below.

The positions of the inclusions were created randomly and sequentially with the random sequential adsorption algorithm (RSA) (Segurado and LLorca, 2002). The fiber diameter, D, was determined from the total number of fibers N and the volume fraction ξ. The generation algorithm propose a center of fiber, i, which is accepted if the distance between this fiber and all the fibers previously accepted $j = 1, ..., i-1$ exceeded a minimum value, $1.035D$, imposed by the feasibility of creating an adequate finite elements mesh. If the fiber i cuts any of the square unit cell sides, this condition has to be checked with the particles near the opposite surface because

the microstructure of the composite is periodic (Fig.1.6). If $\vec{x}^i$ stands for the center coordinates of circle i these conditions are expressed by

$$\min\left\{||\vec{x}^i - \vec{x}^j + \vec{h}||\right\} \geq 1.035D \tag{1.7}$$

for any value of $\vec{h} = (k, l)$ where k and l can take the values $0, L, -L$, leading to 5 conditions which should be checked for each pair of fibers. Moreover, to avoid distorted finite elements during meshing, the fiber surface should not be very close to the cell faces, and this led to an extra condition

$$||x_k^i - r|| \geq 0.045D \; ; \; k = 1, 2 \tag{1.8}$$

$$||x_k^i + r - L|| \geq 0.045D \; ; \; k = 1, 2 \tag{1.9}$$

Boundary conditions

The RVE together with the boundary conditions must generate valid tilings for the underformed and the deformed states. Thus, gaps or overlaps between neighboring cells and unphysical constraints should be avoided in the problem solution as they lead to continuum mechanics inconsistencies. In order to achieve this, the applied boundary conditions should generate the appropriate deformation modes for the studied load cases. The most commonly employed boundary conditions are the symmetry and periodicity.

Symmetric boundary conditions

Periodic microfield approaches can be employed to study composites through very simplistic arrangements of inhomogeneities. Simple cubic, face centered cubic or body centered cubic arrangements can be good approximations for three dimensional studies of particle reinforced composites, and rectangular or hexagonal distributions of inhomogeneities are often used for the two dimensional study. In theses cases, it is possible to choose a unit cell in which the faces of the cell coincide with the symmetry planes of the phase arrangement (Fig. 1.7), and symmetric boundary conditions can be easily applied (Fig. 1.8).

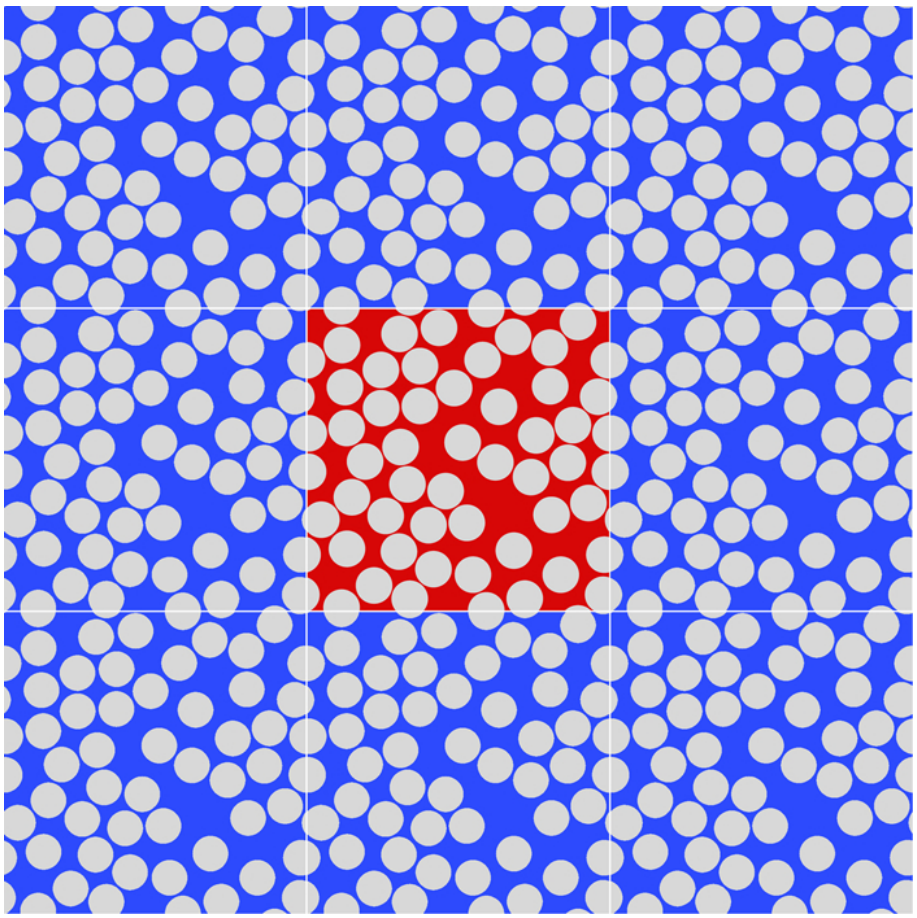

Figure 1.6: Unit cell containing a RVE of 30 fibers randomly distributed in a square domain and the periodic microstructure generated by the repetition of the unit cell.

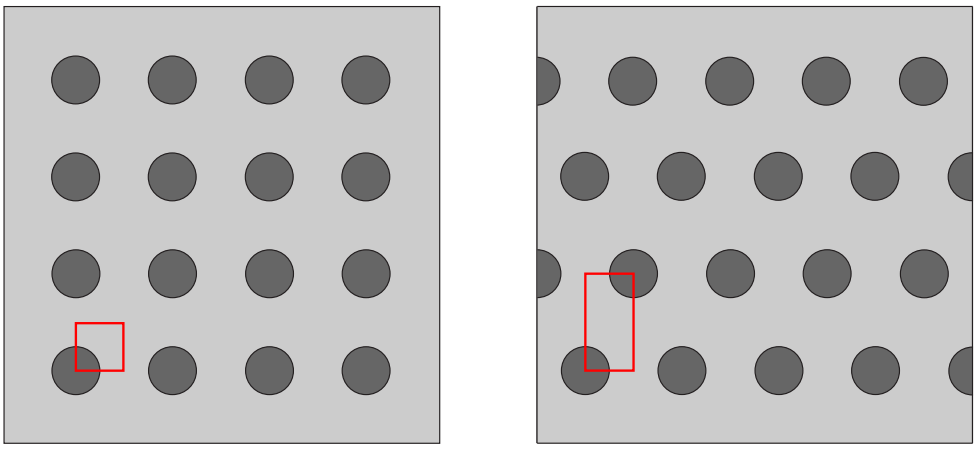

Figure 1.7: Periodic square and hexagonal fiber arrangement and its units cells (Pettermann and Suresh, 2000).

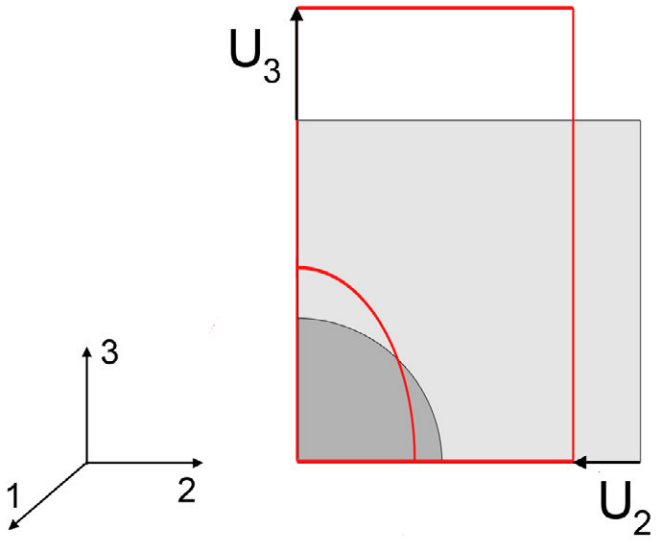

Figure 1.8: Diagram of symmetric boundary conditions in a rectangular two dimensional model.

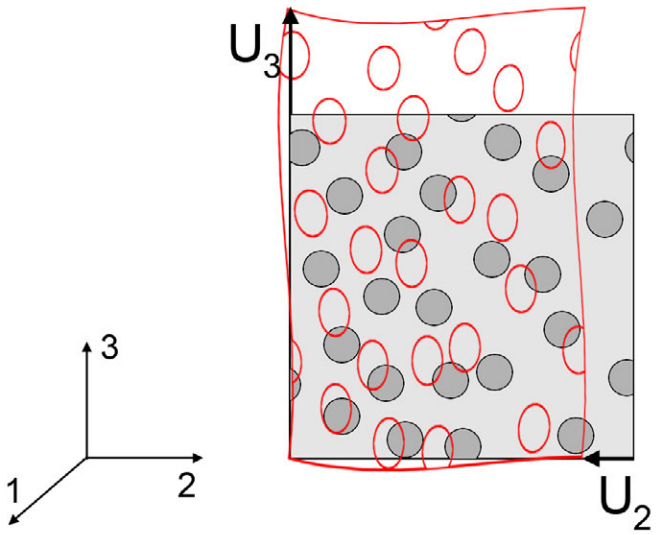

Figure 1.9: Diagram of periodic boundary conditions in a rectangular two dimensional model.

Symmetric boundary conditions are typically very useful for describing simple microgeometries, they are fairly easy to use and have very low computational cost. However, the load cases that can be handled by symmetric boundary conditions are limited to homogeneous thermal loads, mechanical loads acting in directions normal to one or more pairs of faces, and combinations of them.

Periodic boundary conditions

Periodic boundary conditions are considered the more general way to introduce a far-field stress and strain into the RVE. The application of periodic boundary conditions to the edges of the RVE ensures the continuity between neighboring RVEs, which deform like jigsaw puzzles (Fig. 1.9).

The periodic boundary conditions in a general three dimensional unit cell can be expressed in terms of the displacement vectors $\vec{U}_1, \vec{U}_2$ and $\vec{U}_3$ between opposite faces of the RVE

$$\vec{u}(0, x_2, x_3) - \vec{u}(L_1, x_2, x_3) = \vec{U}_1 \quad (1.10)$$

$$\vec{u}(x_1, 0, x_3) - \vec{u}(x_1, L_2, x_3) = \vec{U}_2 \quad (1.11)$$

$$\vec{u}(x_1, x_2, 0) - \vec{u}(x_1, x_2, L_3) = \vec{U}_3. \quad (1.12)$$

where L_1, L_2 and L_3 are the dimensions of the RVE along their coreresponding directions.

Periodic boundary conditions can be used to introduce any physically homogeneous deformation state within the unit cell. For example, a uniaxial tension along the x_3 axis is imposed with $\vec{U}_3 = (0, 0, \delta_t)$, where δ_t stands for the imposed tensile displacement. The components of $\vec{U}_1$ and $\vec{U}_2$ are chosen so that the all the normal and shear forces acting on the RVE surfaces are zero (besides those corresponding to the imposed transverse tension). The corresponding logarithmic strain is given by $\epsilon_3 = \ln(1 + \delta_t/L_3)$, and the corresponding Cauchy normal stress (σ_3) can be computed from the resultant normal forces acting on the RVE faces divided by the actual cross-section.

An important drawback of periodic boundary conditions is the high computational cost when they are applied in a finite elements code because of the multipoint constraints required for their implementation.

1.6.2 Embedded cells

The embedded cell consist in a model representing either a raw material or a specimen with two different microstructural descriptions. First of all, a core, where the microstructure is resolved with a high level of detail (including the matrix, reinforcement and interfaces). This domain is embedded in an outer region where the microstructure is roughly resolved or even considered as a homogeneous domain. Through this simulation strategy is possible reproduce in the core the stress and strain fields developed at the microstructural level, while the embedding outer region is responsible to transmit the far-field loads to the core. The schematic of a three-point bending specimen is plotted in Fig. 1.10, where the high stress and strain region

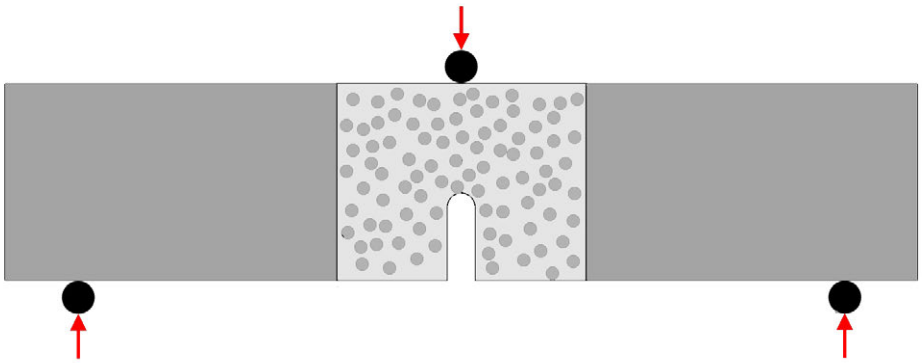

Figure 1.10: Schematic of an embedded cell approach to simulate the three-point bending test of a notched beam specimen.

is modeled in detail while the remaining beam is considered to be an homogeneous material.

Depending on the considered outer region, Böhm (1998) classified the embedded cell approaches in three basic types:

- Models which employ discrete microstructures for the core and the embedding regions, but discretized with different element size (Sautter et al., 1993). This model can easily reproduce a full sample with a refined mesh in some regions of interest, avoiding the usual layer effects produced at the interfaces between the core and the outer region. However, this strategy has an important drawback in the very high computational cost.

- Models which take into account the outer region as a homogeneous material with a constituve law defined a priori based on empirical or micromechanical approaches. These models are specially suited to study the localization and growth of cracks in inhomogeneous materials (Wulf et al., 1996; González and LLorca, 2007b) or the stress concentrations near the crack tips (Aoki et al., 1996) or around local defects (Xia et al., 2001).

- Embedded cell approaches which obtain the effective behavior of the outer region from the homogenized response of the core through a self-consistent

scheme. In a first step, trial properties are impose to the outer region, the stress and strain fields are computed in the microstructure of the core. In the following steps, the homogeneous response of the core is used for the constitutive behavior of the outer region. This process is repeated until the convergence is achieved. These models have been mainly employed for material characterization (Yang et al., 1994; Chen, 1997). They are easily used in elastic regime, but they can be very complex when dealing with elastoplastic behavior.

1.7 Constitutive models for FRPs microconstituents

A critical issue in computational micromechanics is to account for the actual deformation and failure micromechanisms of each phase and this is carried out normally through the appropriate constitutive equations at the constituent level. In the particular case of unidirectional composites loaded in the transverse plane, the behavior under compression is controlled by the shear yielding of the matrix and the decohesion of the fiber-matrix interfaces. Moreover, under transverse tension loads the brittle decohesion of the interfaces triggers the final failure of the material, leading to a brittle behavior of the composite. The different processes have to be taken into account in the numerical analysis to provide realistic results.

The polymer matrix in FRPs is usually a thermoplastic or thermoset resin and their mechanical properties depend on the chemico-physical characteristics and the manufacturing processes. Thermoset resins are made from molecules with relatively small molecular weight called prepolymers. Since the length of these molecules is short, the material is initially a liquid of low viscosity at room temperature and, therefore, they are specially suited for processing of FRPs. The liquid resin is injected or infused into the fibers preforms and easily flows through the reinforcement, obtaining good impregnation of the fibers with low porosity. Once the fiber reinforcement is completely saturated, the resin is cured to make it solid. In order to cure the thermoset, the prepolymers must be tied together with other molecules. This process, known as cross-linking, occurs under the appropriate conditions of temperature and pressure. Thus, the resin is finally transformed into a solid, by the 3D chaining

network created between the prepolymers. Since the cross-linking is a nonreversible process, the shape of the created component cannot be changed after curing.

The most common polymeric matrices for high performance and aircraft grade composites are the epoxy resins. They have been extensively used due to their excellent properties such as good adhesion, good corrosion resistance, low shrinkage and processing versatility. On the other hand, epoxy resins present some important drawbacks, such as their cost and higher viscosity than other thermosetting resins, which results in more intricate and costly manufacturing processes. Therefore, the epoxy is only employed in high added-value applications such as aircraft, sports, etc.

The matrix-fiber interfaces of FRPs are widely studied in different fields. Chemistry and molecular physics study topics as the nature of the bonds, surface density or their ranges of action at molecular level (Fowkes, 1987; Mittal, 1995). However, from a technical viewpoint, the most relevant problems of the interfaces are the stress transfer efficiency, their strength and the process of decohesion (see Fig. 1.11) (Zhandarov and Mäder, 2005).

1.7.1 Plastic behavior of the matrix

The highly linked 3D network structure of a cured epoxy resin provides the solid material with outstanding mechanical properties. As any polymeric system, its initial deformation is dominated by the viscoelastic phenomena. However, due to the extensively entangled of its macromolecules, these time dependent effects can be neglected and modeled as an isotropic linear elastic solid until yielding.

The yield behavior of polymers depends on temperature and strain rate. However, the conventional yield criteria can accurately describe the plastic behavior of polymers by controlling the test conditions. Following this strategy, many studies of the yield behavior of epoxies have bypassed the question of strain rate and temperature and sought to establish a yield criterion (Cherry and Thomson, 1981; Kinloch and Young, 1983).

In tension at room temperature, epoxy resins usually fail at very low strain prior to any yielding, but in contrast, they exhibit yielding during uniaxial compression test, even at relatively low temperatures (Yamini and Young, 1980). The yield stress

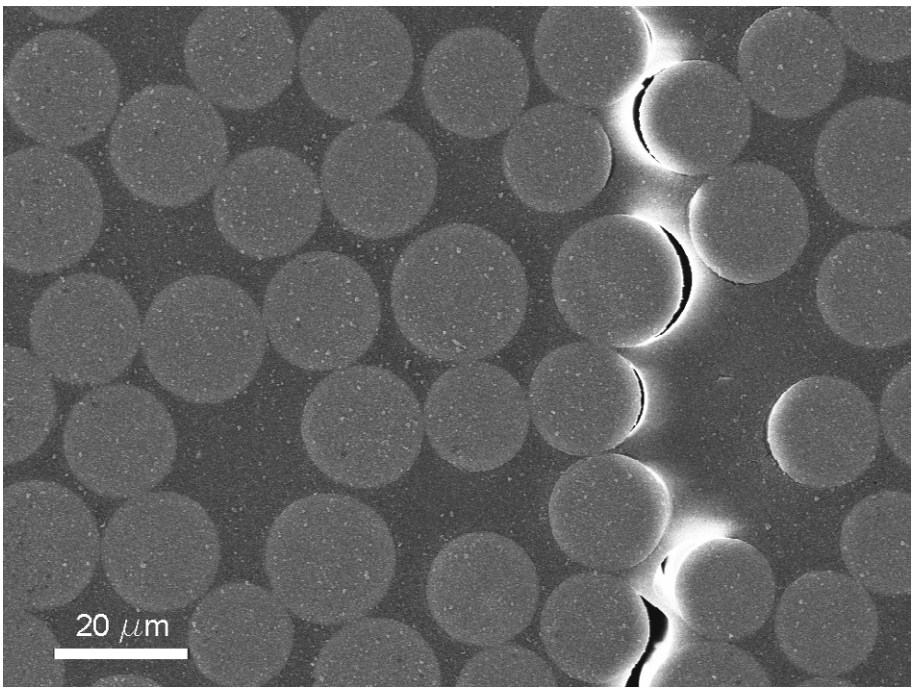

Figure 1.11: Scanning electron micrograph obtained during a three-point bending test of a glass/epoxy composite.

in these materials is often defined as the point of maximum load, at which that the subsequent deformation occurs without further increase in stress (Yee et al., 2000). Moreover, the yield behavior of epoxies is pressure-sensitive, and yield stress decreases with hydrostatic tension and increases with hydrostatic compression. This dependence is taken into account by pressure-dependent yield criteria like Mohr-Coulomb or Drucker-Prager, which were initially developed to characterize the plastic flow of soils and rocks.

Mohr-Coulomb yield criterion

The Mohr-Coulomb criterion assumes that yielding takes place when the shear stress acting on a specific plane, τ_t, reaches a critical value, which depends on the normal stress, σ_n, acting on that plane. This can be expressed as

$$\tau_t = c - \sigma_n \tan\phi \tag{1.13}$$

where c and ϕ stand, respectively, for the cohesion and the friction angle, two materials parameters which control the plastic behavior of the material. Physically, cohesion c represents the yield stress under pure shear loading while the friction angle takes into account the effect of hydrostatic pressure. When $\phi = 0°$ Mohr-Coulomb model is reduced to the pressure-independent Tresca model while $\phi = 90°$ leads to the "tension cut-off" Rankine model. The value of both parameters for an epoxy can be approximated from the strength, σ_{yc}, and the orientation of the shear bands, θ, in uniaxial compression tests. They are given by

$$\sigma_{yc} = 2c\frac{\cos\phi}{1-\sin\phi} \text{ and } \theta = 45 + \phi/2 \tag{1.14}$$

where θ is the shear band angle, typically $50° < \theta < 60°$ for uniaxial compression loads in epoxy matrices (Puck and Schürmann, 2002; Pinho et al., 2006; Aragonés, 2007; Totry et al., 2008a).

The yield surface of the Mohr-Coulomb model can be rewritten in terms of the maximum and minimum principal stresses (σ_I and σ_{III})

$$F_{MC}(\sigma_I, \sigma_{III}) = (\sigma_I - \sigma_{III}) + (\sigma_I - \sigma_{III})\sin\phi - 2c\cos\phi = 0 \tag{1.15}$$

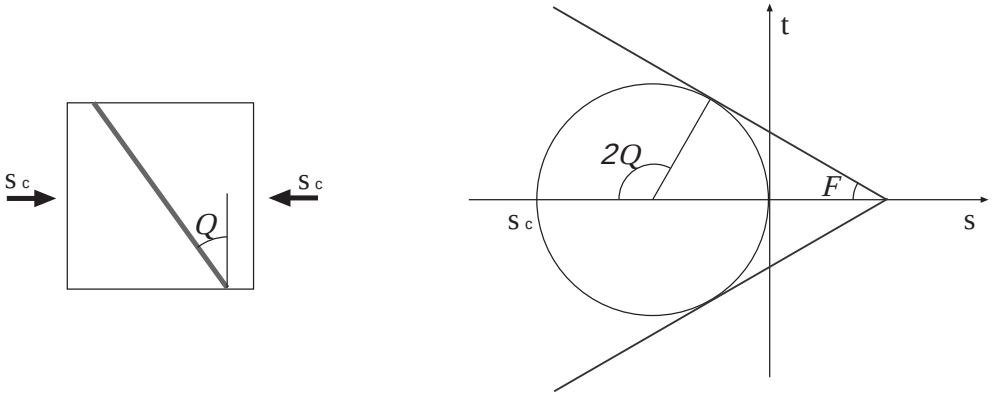

Figure 1.12: Shear band created by a uniaxial compression stress and Mohr's circle for this stress state.

The Mohr-Coulomb criterion presents two important drawbacks for its practical application. First, it does not depend on the intermediate principal stress, $\sigma_I I$, which underestimates the yield strength of the material in many cases (Mogi, 1971). Second, the yield surface in Fig. 1.13 shows sharp corners which impairs its numerical implementation.

Drucker-Prager yield criterion

The criterion was initially proposed to deal with the plastic deformation of soils (Drucker and Prager, 1952). However, this yield criterion and its subsequent modifications have been extensively applied to other pressure-dependent materials like rocks (Zhang and P. Cao, 2010), concrete (Arslan, 2007) or polymers (Quinson et al., 1997).

The linear Drucker-Prager yield function can be expressed as

$$F_{DP}(J_1, J'_2, \alpha) = \sqrt{\frac{3}{2}J'_2} + J_1\alpha - d = 0 \tag{1.16}$$

where J_1 is the first invariant of the stress tensor, J'_2 is the second invariant of the deviatoric stress tensor, d is the yield stress of the material under pure shear loading

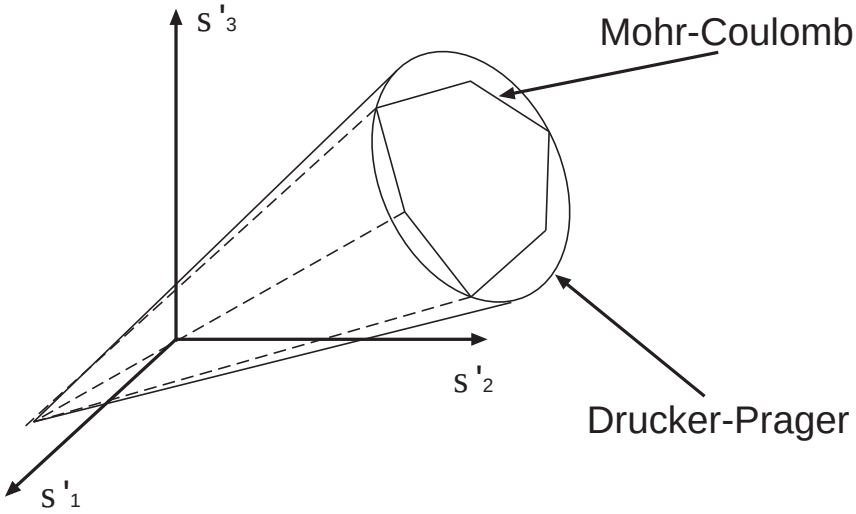

Figure 1.13: Mohr-Coulomb and Drucker-Prager yield surfaces in the deviatoric stress space.

and α is the pressure sensitivity parameter, which, according to experimental results, is in the range 0.10-0.30 for glassy polymers (Kinloch and Young, 1983).

The Drucker-Prager yield criterion can also be rewritten in terms of the principal stresses, as in the case of the Mohr-Coulomb criterion,

$$F_{DP}(\sigma_I, \sigma_{II}, \sigma_{III}) = \sqrt{\frac{(\sigma_I - \sigma_{II})^2 + (\sigma_{II} - \sigma_{III})^2 + (\sigma_{III} - \sigma_I)^2}{2}} + (\sigma_I + \sigma_{II} + \sigma_{III})\alpha - d = 0 \quad (1.17)$$

Interrelationship between Mohr-Coulomb and Drucker-Prager parameters

Mohr-Coulomb and Drucker-Prager criteria are commonly used to describe the yield behavior of granular materials. In many cases, the available experimental data are given for one of such criterion, being necessary to obtain the relation between them. In this situation, the Drucker-Prager yield surface can be matched with the

Mohr-Coulomb surface by the selection of the parameters α and d, through the following relations (Jiang and Xie, 2011)

$$\alpha = \frac{-\sin\phi}{\cos\eta - (1/\sqrt{3})\sin\eta\sin\phi} \tag{1.18}$$

$$d = \frac{c\cos\phi}{\cos\eta - (1/\sqrt{3})\sin\eta\sin\phi} \tag{1.19}$$

where η is the Lode angle, which is controlled by the relationship of the intermediate principal stress and the major and minor principal stresses, providing different possibilities to match the Drucker-Prager and Mohr-Coulomb criteria (Fig. 1.14). If both surfaces match along the compressive meridian ($\eta = -30°$), the Drucker-Prager cone represents an outer bound cone of the Mohr-Coulomb hexagonal pyramid. When $\eta = 0°$ the surfaces match along shear meridian, and the inner cone of the Mohr-Coulomb yield surface coincides with Drucker-Prager at $\eta = 30°$.

1.7.2 Matrix damage behavior

The epoxy resins employed in the matrix of FRPs exhibit large deformations and plastic yielding under compressive loads, while tension stresses lead to sudden failure. The characterization of the fracture behavior of the matrix is an essential step to study the mechanical behavior of the FRPs.

Inglis (1913) made the first attempt to study mathematically the fracture in materials by analyzing the case of an elliptical hole in a plate subjected to a remote tensile stress perpendicular to the major axis of the notch. He showed that the maximum stress occurs at the vertex of the major axis, where the radius of curvature is minimum. Moreover, when the elliptical notch is collapsed into a perfect crack, the stress field is singular. Since real materials only support finite stresses, this result indicated that a cracked component cannot sustain any loading if a criterion of maximum stress is applied, which contradicts the experimental observations. Griffith (1921) applied energy conservation principles to study the cracks propagation. Griffith postulated that solids possess a surface energy, and in order to propagate a crack, the externally added energy should exceed the surface energy associated with

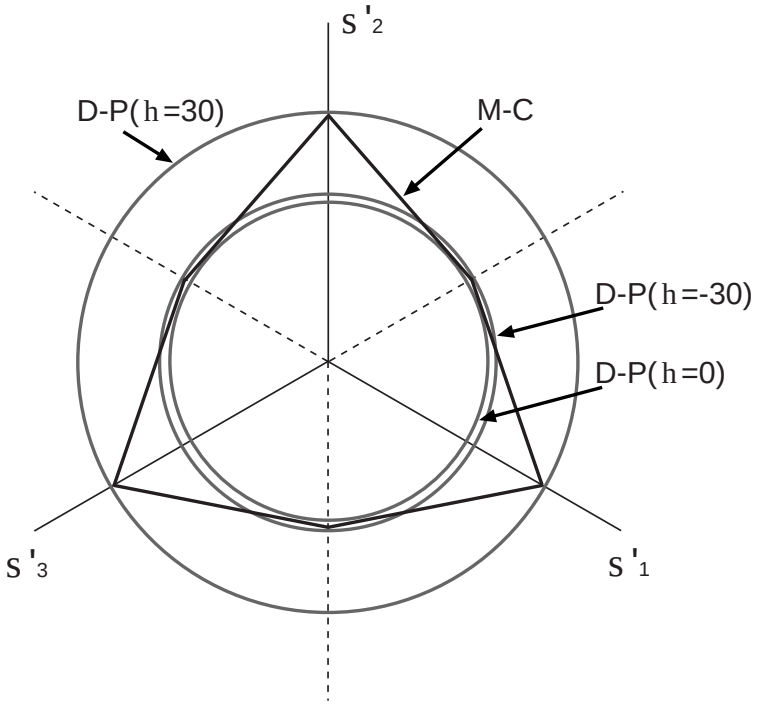

Figure 1.14: Matching between the Mohr-Coulomb and Drucker-Prager yield surfaces in the deviatoric plane.

the new area created during the crack propagation. Griffith introduced the concept *fracture energy* of a material G_f, only applicable to perfectly brittle materials and the experimental measurements of the energy necessary to propagate a crack were orders of magnitude higher than the theoretical estimations. Experimental observations of the crack surfaces showed that plastic deformation takes place at the notch of the tip, even for brittle materials. This led to Irwin (1948) and Orowan (1955) to adopt the concept of the *fracture process zone* for the region surrounding the crack tip. This zone was characterized by a progressive softening, for which the stress decreases at increasing deformation. The fracture process zone is surrounded by a nonsoftening nonlinear region characterized by plasticity, for which the stress remains constant at increasing deformation. In addition, Irwin estimated the size of the fracture process zone through a parameter called characteristic length, which was defined by Hilleborg et al. (1976) as

$$l_{ch} = \frac{EG_f}{{\sigma_t}^2} \tag{1.20}$$

in which E is the elastic modulus and ${\sigma_t}^2$ is the tensile strength of the material. It is possible to distinguish between three types of fracture behavior depending on the ratio between the size of the structure and the characteristic length (D/l_{ch})(Fig. 1.15).

When the characteristic length is small compared to the structure size, fracture takes place in a very small region. Linear elastic fracture mechanics (LEFM) is specially suited for this case and is typically applied to brittle materials like glasses or ceramics. The second type of behavior includes situations in which the nonlinear zone is due to the plastic yielding of the material, and the size of the actual fracture process zone takes place still in a small region. This kind of behavior is typical in ductile metals, and its usually treated by means the elasto-plastic fracture mechanics (EPFM). Finally, the third type of behavior includes situations in which a major part of the nonlinear zone exhibits damage with material softening, due to crazing, void formation, interface breakages and other similar phenomena. This kind of behavior is observed in many materials like concrete, rocks or toughened ceramics, which are known as *quasi-brittle* materials (Bažant and Planas, 1998).

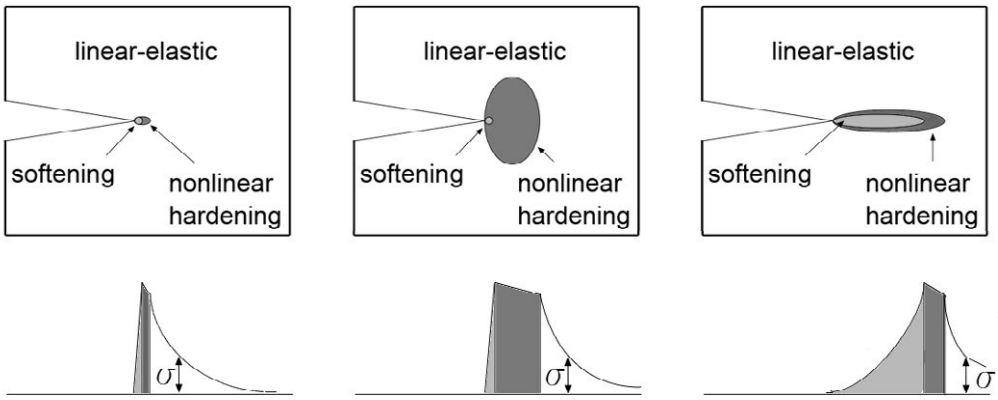

Figure 1.15: Types of fracture process zone. Diagrams at the bottom show the trends of the stress distributions along the crack line. From Bažant and Planas (1998).

Epoxies fail in tension exhibiting very limited elongation and this brittle behavior has been classically treated by means of LEFM (Kinloch and Young, 1983). However, the theoretical fracture toughness, considering a perfectly brittle material, usually underestimates the experimental measurements (Berry, 1964). This fact has been confirmed by fractografic observations were massive plastic deformations by shear banding and crazing around the crack tip were observed (Patrick, 1973). These findings confirmed that toughening mechanisms are operating during the fracture of the epoxy resin and they can be also treated as *quasibrittle materials*. The fracture process in these materials can be properly described by two simplified approaches: cohesive crack models and continuum damage models.

Cohesive crack models

This is the simplest model that can completely describe the progressive fracture process. The cohesive crack approach was initially proposed by Dugdale (1960) to represent the nonlinear processes located at the front of a pre-existing crack in metals and has been extended to quasibrittle materials like concrete, rocks, composites, etc (Hilleborg et al., 1976; Bažant and Oh, 1983; Planas et al., 2003; Sancho et al., 2007;

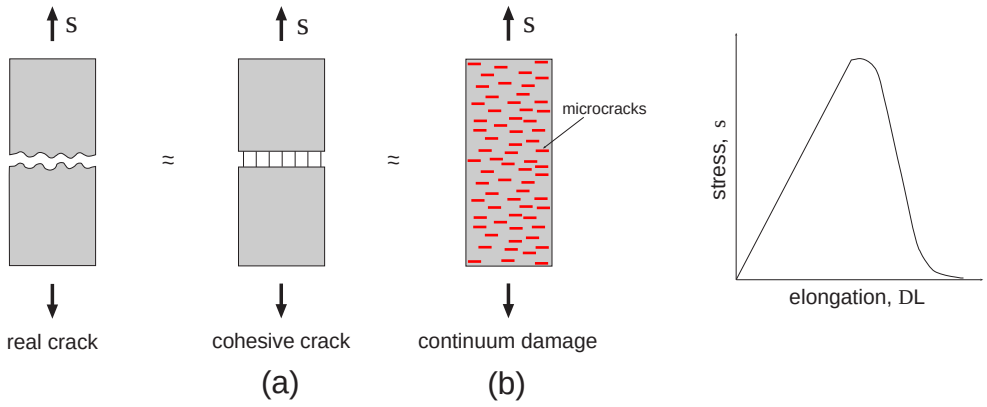

Figure 1.16: Real rough crack idealized as a cohesive crack and a continuum damage model. Stress-elongation curve for the idealized stable tension test.

Fang et al., 2011). In this model the entire fracture process zone is lumped into the crack line and is characterized in the form of a stress-displacement law which exhibits softening (Fig. 1.16(a)). Thus, a cohesive crack is a fictitious crack able to transfer stresses from one face to the other, according to a softening function which is considered a material property. The cohesive crack can be implemented in finite elements codes by means of different methods like extended finite elements, cohesive elements, strong embedded discontinuities, etc. These strategies have been employed to simulate the fracture behavior epoxy resins (Diehl, 2008; Campilho et al., 2011; Y. T. Kim, 2011).

The progressive interface fracture upon loading can be taken into account through the cohesive crack model at the interface between dissimilar materials (Camanho and Dávila, 2002; Segurado and LLorca, 2004). The mechanical behavior of the cohesive crack was expressed in terms of a traction-separation law which relates the displacement jump across the interface with the traction vector acting on it. The initial response of the cohesive elements is linear in absence of damage. Therefore, for a two dimensional cohesive element, the traction-separation law could be written as

$$t_n = K\delta_n \qquad \text{and} \qquad t_s = K\delta_s \tag{1.21}$$

where t_n, t_s, δ_n and δ_s stand for the normal and tangential tractions and displacement jumps across the interface respectively. The linear behavior ends at the onset of damage, which is dictated by a maximum stress criterion expressed mathematically as

$$max\{\frac{\langle t_n \rangle}{N}, \frac{t_s}{S}\} = 1 \tag{1.22}$$

in which $\langle\rangle$ stand for the Macaulay brackets indicate that does not develop when the interface is under compression. N and S are the normal and tangential interfacial strengths, respectively. Once damage begins, the stress transferred through the crack is reduced depending on the interface damage parameter d, which evolves from 0 (in the absence of damage) to 1 (no stresses transmitted across the interface), as shown in Fig. 1.17. The corresponding traction-separation law is expressed by

$$\begin{aligned} t_n &= (1-d)K\delta_n \quad \text{if} \quad \delta_n > 0 \\ t_n &= K\delta_n \qquad\quad \text{if} \quad \delta_n \leq 0 \\ t_s &= (1-d)K\delta_s \end{aligned} \tag{1.23}$$

For a linear softening law, the evolution of the damage parameter is controlled by an effective displacement, $\bar{\delta}$, defined as the norm of the displacement jump vector across the interface as

$$\bar{\delta} = \sqrt{< \delta_n >^2 + \delta_s^2}, \tag{1.24}$$

and d depends on the maximum effective displacement at the interface attained during the loading history at each material integration point $\bar{\delta}^{max}$ according to

$$d = \frac{\bar{\delta}^f(\bar{\delta}^{max} - \bar{\delta}^0)}{\bar{\delta}^{max}(\bar{\delta}^f - \bar{\delta}^0)} \tag{1.25}$$

where $\bar{\delta}^0$ and $\bar{\delta}^f$ stand for the effective displacement at the onset of damage ($d = 0$) and when the interface has failed completely ($d = 1$), respectively. In this cohesive

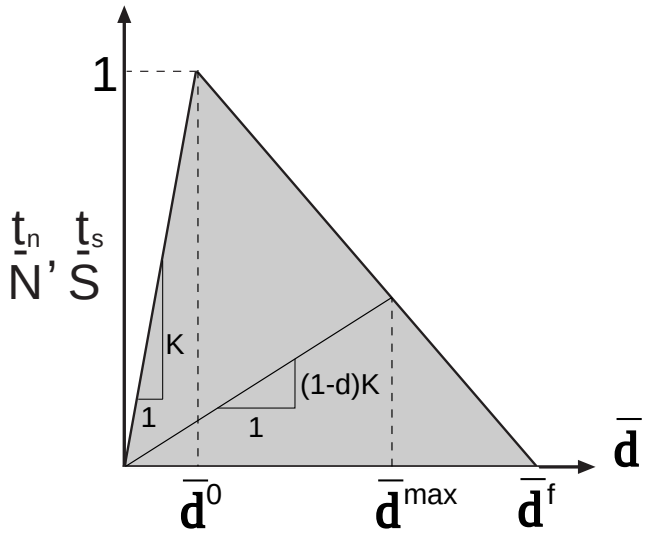

Figure 1.17: Schematic of the traction-separation law governing the behavior of the cohesive crack at the fiber/matrix interface.

model, the energy necessary to completely break the interface is the interface fracture energy G, which can be defined as

$$G = \frac{1}{2} T_{eff} \delta^f \tag{1.26}$$

being T_{eff} the effective traction at the damage initiation

$$T_{eff} = \sqrt{N^2 + S^2} \tag{1.27}$$

Continuum damage models

Continuum damage mechanics is a constitutive theory describing damage by the generation, propagation and coalescence of cracks or voids at the microscopic level. The progressive degradation of the material leads to its final failure (Fig. 1.16(b)). Continuum damage models do not account for individual cracks, but smear their effect over a region of the material by degrading the stiffness and strength of the cracked material. The continuum damage models have been implemented in finite

elements codes through the degradation of the elastic moduli, the decreasing of the yield stress or combining both. The different approaches have a similar response upon the material loading, but differences appear during the unloading (Fig. 1.18).

The first continuum damage model was proposed by Kachanov (1958) and Rabotnov (1968) by introducing a scalar internal variable to take into account the reduction of the cross-sectional area produced by microcracking during the creep failure in metals. Therefore, denoting respectively by A_o and A the effective load bearing areas of the pristine and damage material, the damage variable, D_K, was introduced by

$$D_K = \frac{A - A_o}{A} \tag{1.28}$$

where $D_K = 0$ represents undamaged material and $D_K = 1$ fully damaged material with a total loss of load-bearing capacity. Considering the damage variable, the observed stress, σ, is replaced by the effective stress, σ_{eff}.

$$\sigma_{eff} = \frac{\sigma}{1 - D} \tag{1.29}$$

Lemaitre (1984) also considered a scalar damage variable, D_L, to represent the stiffness degradation experimentally observed in ductile metals under load-unload cycles

$$E = (1 - D_L)E_o \tag{1.30}$$

The damage evolution can also be coupled with the plastic behavior of metals, Gurson (1977) described the mechanism of damage by void growth in porous metals producing an evolution of the yield surface. Initially, when the material is undamaged $D_G = 0$, the plastic behavior is governed by the von Mises yield criterion. However, in presence of damage, $D_G \neq 0$, the yield behavior becomes pressure-sensitivity and the yield surface shrinks.

The continuum damage models have been extensively used in finite element analysis because of their easy implementation in computational codes as constitutive equations at Gauss points at material level. These strategies have been successfully employed to simulate the fracture in a wide variety of materials such as metals (Tvergaard and Needleman, 1984), concrete (Mazars, 1986), polymers (Jeong, 2002; Canal

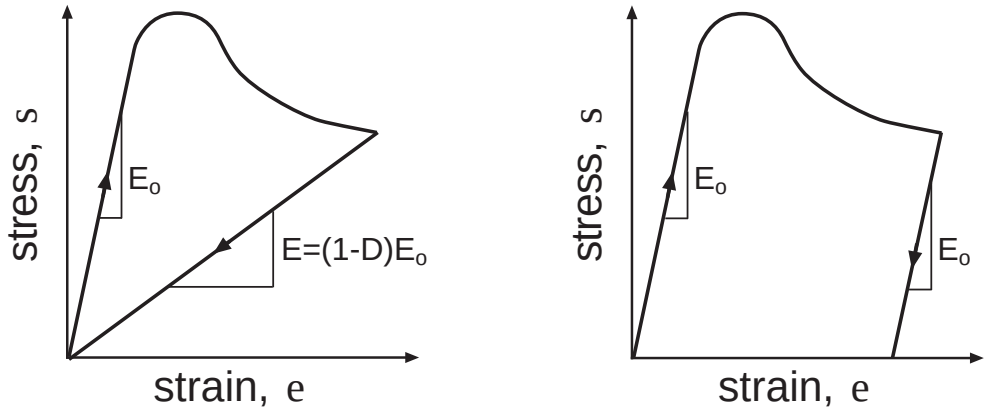

Figure 1.18: Illustration of loading-unloading curve for the smeared crack model implemented through the degradation of the elastic moduli and the decrease of the yield stress.

et al., 2009) or FRPs (Ladevèze and Lubineau, 2001; Camanho et al., 2007; Maimí et al., 2007).

Strain localization and mesh adjustment

When the crack opening is modeled by a displacement jump, as it is done by the cohesive crack models, it is possible to formulate an objective traction-separation law. In this case, the numerical result does not exhibit pathological mesh sensitivity. On the other hand, when the crack is smeared over a softening region of an arbitrary size (e.g. the element size), the resulting model can be physically incorrect and numerically ill-posed.

For illustrating this problem, let us consider a homogeneous bar of initial length L subjected to a tensile load and made of softening material. This bar can be subdivided in N identical pieces which act as equal elements coupled in series. In this case, after the peak of maximum stress, strain localizes in only one element, resulting in different stress-strain curves, depending on the length of the pieces, implying that the result obtained through finite element models would completely depend on the mesh density

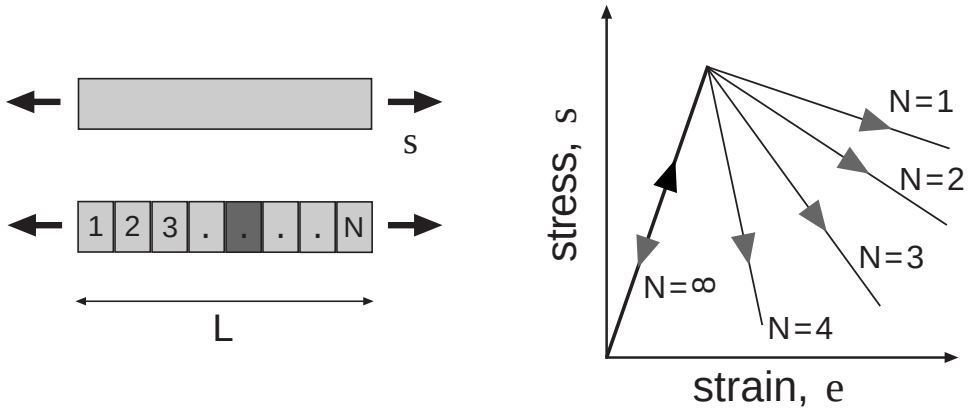

Figure 1.19: Homogeneous bar subdivided into N equal elements and the resulting stress-strain curves.

(Fig. 1.19). This problem is referred as lack of *mesh objectivity* or *spurious mesh sensitivity*.

The mesh sensitivity is not acceptable in finite elements calculations and it must be avoided. The simplest remedy, frequently used in engineering applications, is based on an adjustment of the stress-strain diagram depending on the size of the element. This technique was proposed for softening plasticity models (Pietruszczak and Mroz, 1981) and later applied to damage models (Bažant and Oh, 1983). The degradation of the material is due to the opening of microcracks which later collapse into a macroscopic crack producing the final failure. If the crack opening is modeled by a displacement discontinuity, as is done in the cohesive crack models, it is possible to formulate a traction-separation law as the constitutive description of the damage. Since the crack opening does not depend on the element size, the numerical results do not exhibit pathological mesh sensitivity because the physical description of the fracture process is objective. Then, a stress-strain law can be constructed at each material point by taking into account the width of the simulated process zone (which depends on the type and size of the corresponding finite elements).

The traction-separation law for the crack can be defined by

$$\sigma_n = f(w) \tag{1.31}$$

where σ_n is the traction stress perpendicular to the crack plane and w is the crack opening. Considering for simplicity a uniaxial problem ($\sigma_n = \sigma$), if the crack is smeared over a distance h, the resulting cracking strain is

$$\epsilon_{crack} = \frac{w}{h} = \frac{f^{-1}(\sigma)}{h} \tag{1.32}$$

The total strain in the localization region (L_s) is obtained by combining the cracking and the elastic strains

$$\epsilon = \epsilon_{elastic} + \epsilon_{crack} = \frac{\sigma}{E} + \frac{f^{-1}(\sigma)}{h} \tag{1.33}$$

The remaining part of the material ($L_u = L - L_s$) is in elastic regimen and its strain is given by $\epsilon_{elastic}$. Thus, the total elongation of the material is

$$u = L_u\epsilon_{elastic} + L_s(\epsilon_{elastic} + \epsilon_{crack}) = L\epsilon_{elastic} + L_s\epsilon_{crack} = \frac{L\sigma}{E} + \frac{L_s}{h}f^{-1}(\sigma) \tag{1.34}$$

When $L_s = h$, the term corresponding to the crack opening becomes independent of the finite elements discretization. Therefore, to avoid the mesh sensitivity it is necessary to obtain the value of L_s from the mesh characteristic length and set h equal to this value. In uniaxial problems L_s is the size of the element, but the selection of this parameter can be difficult in multidimensional problems or second-order elements (Oliver, 1989).

1.7.3 Damage-plasticity coupled model of the matrix

The cracking process in quasi-brittle materials is not a sudden onset of new free surfaces, but a continuous nucleation and coalescence of microcracks (Kinloch and Young, 1983; Metha and Monteiro, 1993) and the evolution of microcrack density produces a macroscopical softening in the material.

The plastic-damage approach was first employed by Lubliner et al. (1989); Lee and Fenves (1998) to model the mechanical behavior of quasi-brittle materials. This

model employees a modification of the Drucker-Prager yield function to account for the different strength under tension and compression stress states. In terms of the invariants of the stress tensor, J_1 and J_2', the yield function is given by

$$F_{QB}(J_1, J'_2, \sigma_I, \beta, \alpha) = \sqrt{\frac{3}{2}J'_2} + J_1\alpha + \beta\langle\sigma_I\rangle - d(\tilde{\epsilon}_c^{pl}) = 0 \tag{1.35}$$

where σ_I is the maximum principal stress and β is a function of the tensile and compressive yield stresses, $\sigma_t(\tilde{\epsilon}_t^{pl})$ and $\sigma_c(\tilde{\epsilon}_c^{pl})$ respectively, it is given as

$$\beta = \frac{\sigma_c(\tilde{\epsilon}_c^{pl})}{\sigma_t(\tilde{\epsilon}_t^{pl})}(1-\alpha) - (1+\alpha) \tag{1.36}$$

In many cases, it is useful to avoid the use of the cohesion d by rewriting the yield function in term of the compression yield stress

$$F_{QB}(J_1, J'_2, \sigma_I, \beta, \alpha) = \frac{1}{1-\alpha}\left(\sqrt{\frac{3}{2}J'_2} + J_1\alpha + \beta\langle\sigma_I\rangle\right) - \sigma_c(\tilde{\epsilon}_c^{pl}) = 0 \tag{1.37}$$

the yield surface under plane stress conditions is plotted in Fig.1.20. For compression stress states, the quasi-brittle material yields following the standard Drucker-Prager yield criterion. However, under tension loads, the criterion predicts a yielding mainly controlled by the maximum principal stress, similar to the Rankine model applied for perfectly brittle materials. The model assumes two competing deformation mechanisms: the tensile cracking and compressive shear banding. The evolution of the yield surface is controlled by two internal damage variables $\tilde{\epsilon}_t^{pl}$ and $\tilde{\epsilon}_c^{pl}$, depending on the failure mechanisms under tension and compression loading, respectively.

Under uniaxial compression the response of the material is linear and elastic until the value of the initial yield σ_{c0} which corresponds with the onset of the plastic regime. For uniaxial tension, the stress-strain response follows a linear behavior until the value of the failure stress σ_{t0} is reached. The failure stress corresponds to the onset of microcracking in the material (Fig. 1.21), beyond this point failure stress the formation of microcracks produces softening by decreasing the yield stress.

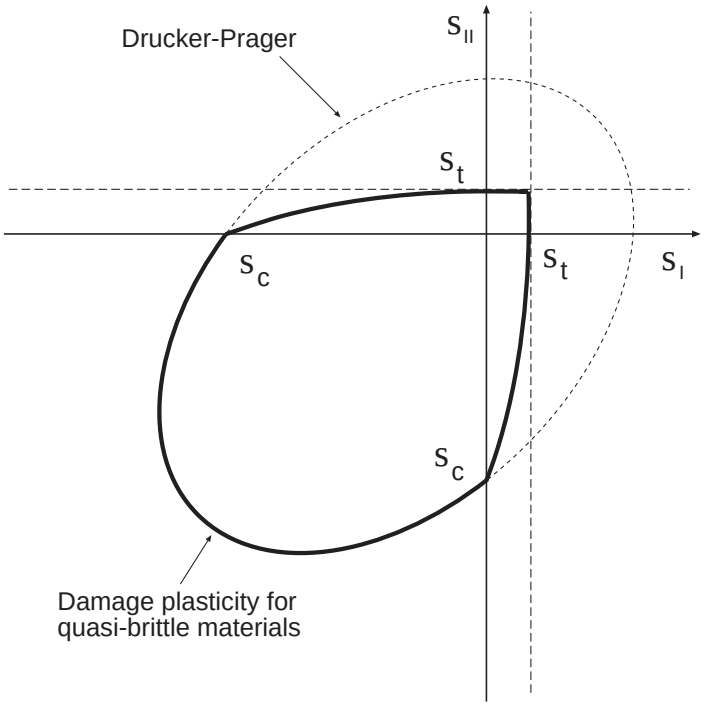

Figure 1.20: Yield surfaces in plane stress.

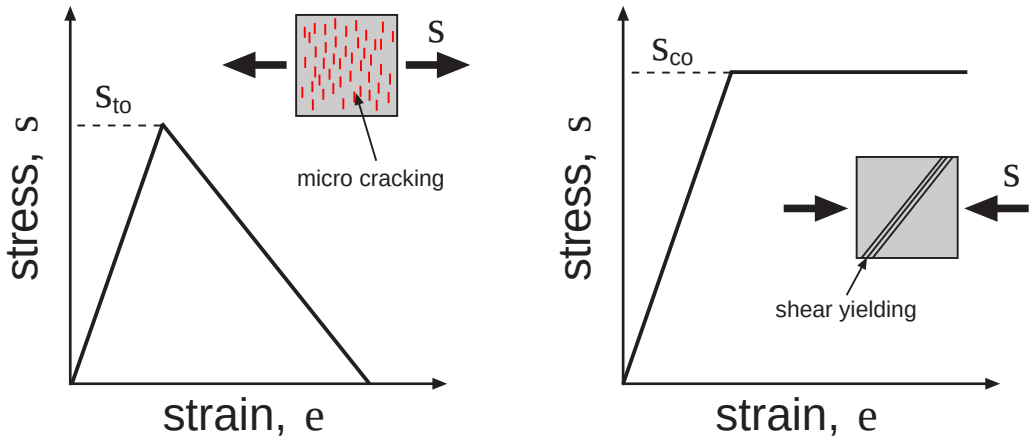

Figure 1.21: Response of quasi-brittle material to uniaxial loading in tension and compression.

1.7.4 Fiber-matrix interface

Matrix-reinforcement decohesion is one of the main damage mechanisms in FRPs because it leads to significant reductions of the strength, ductility and toughness of the material (LLorca, 2000). Interface fracture initiates by the nucleation of a crack as the stress at the interface exceeds the interfacial strength. Damage progresses as the crack propagates along the matrix-fiber interface and reduces the amount of load transferred from the matrix to the reinforcement. Finally, the fracture of the composite can occur by the coalescence of interface cracks connected by shear bands in the matrix. For these reasons, the fiber-matrix decohesion is considered a key mechanism which should be taken into account to analyze the overall composite behavior.

Interface fracture in composites has been modeled by two different strategies. Mean-field approximations (Zhao and Weng, 1996; Sun et al., 2003) represented the composite as a three-phase material formed by the continuous matrix, intact and debonded reinforcement. It was assumed that interface fracture was strength-controlled, and that decohesion occurred when the average tensile stress in the reinforcement along the loading axis surpassed a critical value identified as the interface strength. These models provided the first estimations of damage evolution by interface fracture during deformation but present some limitations. First, interface fracture is controlled by maximum stress values which may be very different from the average stress in the reinforcement. Second, they assumed that the interface decohesion was complete, while experimental observations always showed partial decohesions (Fig. 1.11).

Most of these limitations to simulate the matrix-fiber decohesion are overcome by the second strategy. In this approximation interface fracture is simulated by a cohesive crack model using interface elements inserted between fibers and matrix. This technique takes into account the effect of interface strength and toughness, and its results are in good agreement with the experimental patterns of interface decohesion (Canal et al., 2011) and the effective properties of composites subjected to elastic (Gusev, 1997; Michel et al., 1999; Segurado and LLorca, 2002) and elasto-

plastic deformation (Böhm and Han, 2001; Segurado et al., 2003; González et al., 2004).

1.8 Objectives

FRPs present outstanding mechanical properties (stiffness and strength) and low density, which compete favorably with metallic alloys, the standard structural materials for engineering applications. Since FRPs became affordable, as a result of the maturation of the processing and quality control techniques, their use in structural components was spread in many industrial sectors. The strength of a composite laminate is assessed nowadays through the application of physically-based phenomenological failure criteria. These criteria establish a failure locus in the stress space, which is formed by the intersection of various smooth surfaces, each one representing the critical condition for a given fracture mode. However, the comparison of their predictions with the experimental results indicate that the existing knowledge on failure mechanisms of FRPs needs further development. Therefore, without accurate models to predict the failure strength of laminates, it is necessary to perform a high number of tests to validate the safety of composite structures through a costly trial-and-error approach.

Recent developments in computational micromechanics have demonstrated that the mechanical behavior until fracture of a composite lamina can be obtained, knowing the mechanical properties of its constituents, from numerical simulations of the composite microstructure. This can be the first step in a new multiscale modeling strategy aimed to predict the strength of composite structures. Nevertheless, to perform this virtual testing strategy successfully it is necessary to gain a substantial knowledge of the mechanical properties of the FRPs constituents (matrix, fiber and interfaces) and the failure mechanisms developed in the microstructure. Thus, the objectives of this thesis can be identified as follows.

The main objective of this study is to develop computational micromechanical models to predict the transversal behavior of unidirectional fiber reinforced polymers. These numerical models should be consistent with the main deformation and failure

processes occurring at the microscale. For this reason the second goal of this work is the detailed experimental characterization of a glass fiber/epoxy laminate, where the most relevant mechanical properties of the matrix and the fiber/matrix interfaces were obtained by means of nanoindentation and push-out tests. Moreover, additional information about the deformation and damage mechanisms at the micron scale was obtained through the application of *in situ* SEM testing carried out on cross-section specimens of the laminate. Finally, to assess the validity of the computational models, their results were compared with experimental results and the predictions of the standard failure criteria for FRPs.

Chapter 2

Characterization of the transverse properties of unidirectional FRPs

The compressive and tensile mechanical properties of a commercial unidirectional laminate of epoxy-matrix reinforced with glass fibers were determined, in the transverse direction, by means of the ASTM standard test methods.

2.1 Material

Unidirectional laminates ($[0]_{14}$) were manufactured from pre-impregnated sheets of E-glass/MTM 57 epoxy resin (Advanced Composite Group, UK). Rectangular panels of 350 x 300 x 2.5 mm^3 were heated at 3°C/min and consolidated at 120°C under 0.64 MPa of pressure in an autoclave for 30 min. They were cooled at the same rate of 3°C/min and the pressure was released at 80°C. After manufacturing, the panels were inspected by ultrasound to ensure that they were free of delaminations or other defects. The nominal fiber volume fraction was 54 %.

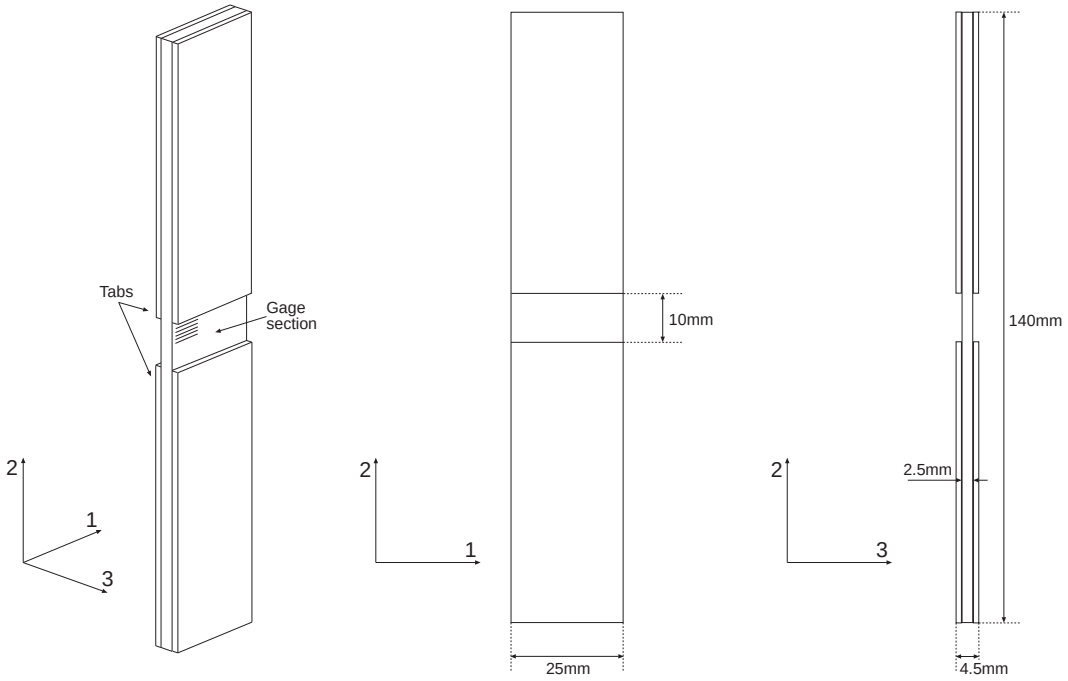

Figure 2.1: Schematic picture of the transversal compression test specimens.

2.2 Compressive properties determination

The transverse compressive properties of the unidirectional E-glass/MTM 57 epoxy laminate were determined according to the ASTM D 3410 standard test method. This test procedure introduces the compression into the specimen through shear forces acting throughout the grips. The compression specimens were machined from the panels of unidirectional laminate with the dimensions recommended by the ASTM standard (Fig. 2.1). Tabs of woven E-glass FRPs were employed to prevent the premature failure of the specimen in the grip area. The tabs were bonded to the specimen surface with an epoxy adhesive, leaving 10 mm of free gage length between them.

The shear load is applied via wedge grips using the IITRI compression test fixture shown in Fig. 2.2. The wedges grips fit into a mating set of wedges that also fit into the upper and lower wedge housing block assemblies. Finally, the housing block as-

semblies are attached to the crosshead of the testing machine. Tests were carried out in a servo-hydraulic mechanical testing machine Instron 8803, under stroke control using a constant cross-head speed of 1mm/min while the load and the displacement were measured using a 25kN Instron load cell and the displacement transducer of the mechanical rig, respectively. The transversal strain was measured using a digital image correlation technique (Vic, Correlated Solutions, Inc.). To this end, one of the specimen surfaces was painted in white and then sprayed in black to created a random pattern of black dots over the white background. The digital image correlation system acquired a high-resolution image of the surface every 2 s and tracked the displacement of the black dots to create a map of the displacement field on the specimen surface. The local lagrangian strain tensor was computed directly as the derivative of the interpolated displacement field obtained from the digital image correlation system. Further details on this measurement technique are described in Chapter 5. In addition, some of the specimens were instrumented with 350 Ω strain gages at both sides to monitor the degree of bending introduced and to check the accuracy of the optical strain method. The strains measured by the strain gages were equivalent to that obtained by the digital image correlation until the strain gages were detached form the specimen.

2.2.1 Experimental results

Ten transversal compression tests were performed on unidirectional $[0]_{14}$ E-glass / MTM 57 coupons according to the ASTM 3410 standard. The stress-strain curves ($\sigma_2 - \epsilon_2$) are plotted in Fig. 2.3. The stresses were computed from the readings of the load cell and the initial cross sectional area of the specimen, while the digital image correlation system allowed the measurement of full-field deformations. The tests were reproducible and exhibited a limited experimental scatter. The shape of the stress-strain curves was typical of unidirectional polymer composites subjected to transversal compression. The behavior was initially linear and the slope of the curve was used to compute the transverse elastic modulus of the laminate $E_2 \approx 12 \pm 2$ GPa. The initial elastic zone ends with a non-linear region in which deformations are mainly controlled by the plastic deformation of the polymeric matrix and the softening effect

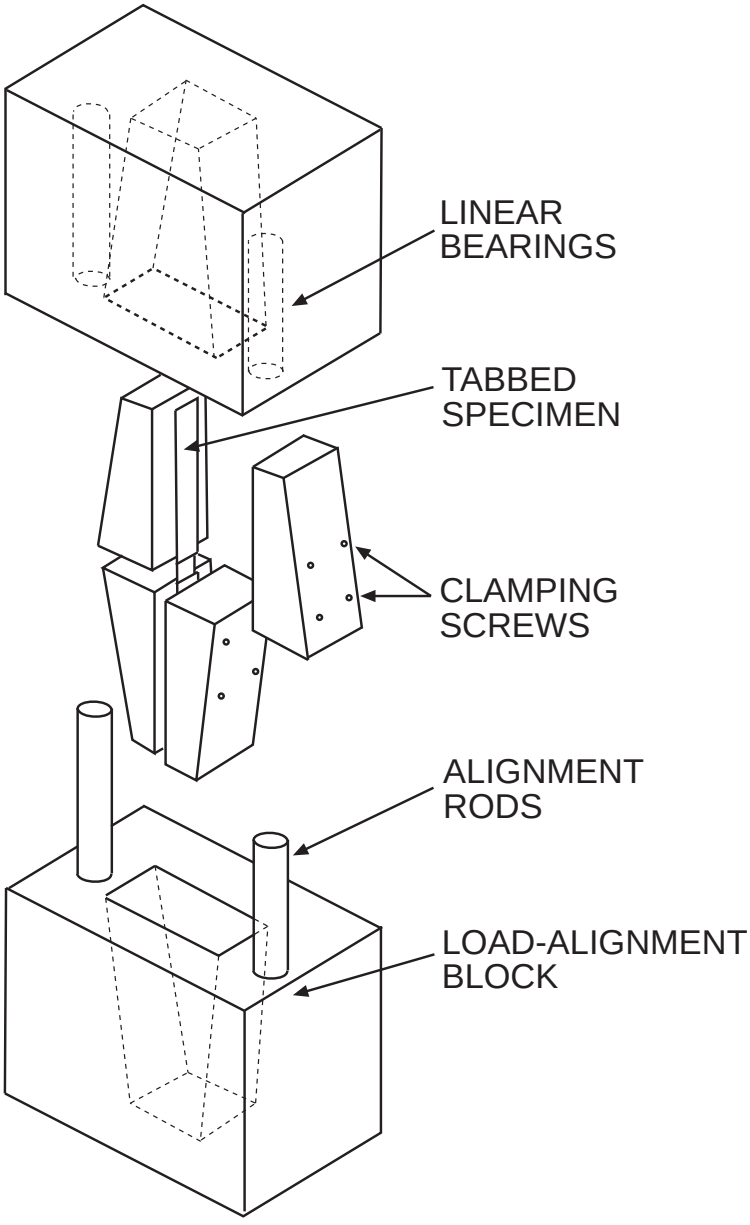

Figure 2.2: Schematic of the IITRI compression test fixture.

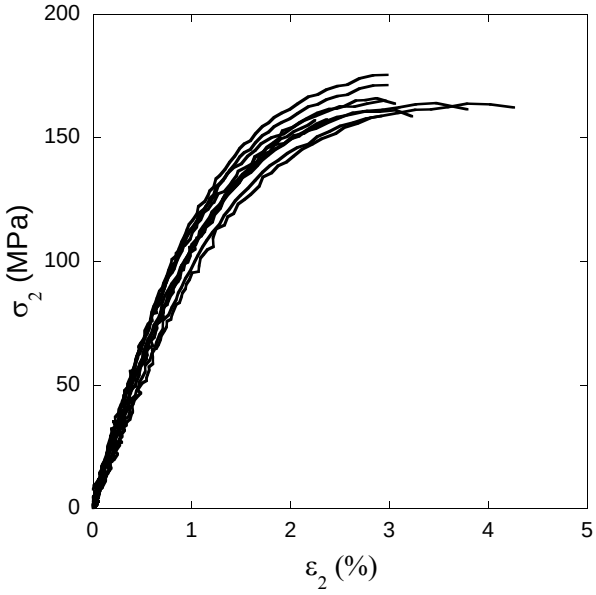

Figure 2.3: Transverse compressive stress *vs.* strain curves for E-glass/MTM 57 epoxy specimens.

of the decohesion of the fibers. In turn, this region ended with the catastrophic failure of the laminate. The strength of the material was obtained, according to the ASTM standard, as the ultimate load divided by the cross sectional area of the specimen, which provided a value of $Y_c \approx 160 \pm 10$ MPa

Fracture surfaces were visually inspected after the compression tests. In all cases, the fracture plane was parallel to the fiber direction and perpendicular to the transverse plane 23, which is an acceptable failure mode according to ASTM standard. Due to the short gage length of the specimens, the failure was mostly located near the tab region, but never inside the grip portion of the specimen, which also meets the requirements of the Standard. The fracture surface of one of the tested coupon is shown in Fig. 2.4. The angle between the fracture plane and the direction perpendicular to the loading axis was also measured by optical microscopy leading to a value of $\Theta \approx 54 \pm 2.0°$.

Experimental evidences and micromechanical simulations of the deformations and

fracture processes of FRPs have pointed out that the fracture plane orientation of the composite under transverse compression can be mainly determined by the pressure sensitivity of the matrix. During the test, before the maximum compressive load is attained, shear bands of severe plastic deformation appear in the matrix. These bands are tilted at a certain angle with respect to the plane perpendicular to the loading axis and their orientation is dependent on the pressure sensitivity of the polymer. The deviation of the experimental fracture angle with respect to the maximum shear stress directions at $\pm 45^{\circ}$ is indicative of the hydrostatic pressure dependent yielding of the polymer matrix (González and LLorca, 2007a). Continuing with the compressive loading of the laminate, the damage by interface decohesion is developed afterwards around the shear bands. The final fracture occurs by the link-up of interface decohesions through the matrix, following the path previously set by the shear bands.

The previously described failure mechanism indicates that the fracture plane orientation is approximately given by the orientation of the shear bands of the polymeric matrix. Therefore, the experimental measurement of direction of the failure plane provides an estimation of the pressure sensitivity parameter of the epoxy matrix. Considering that the plastic behavior of the matrix is represented adequately by a non-dilatant Drucker-Prager yield model, the orientation of the shear bands is given by (Rudnicki and Rice, 1975; Gao et al., 2011)

$$\Theta = \tan^{-1} \sqrt{\frac{\zeta - N_{min}}{N_{max} - \zeta}} \tag{2.1}$$

where $\zeta = (1+\nu)(\alpha) - N(1-\nu)$, $N_{max} = \frac{\sigma'_I}{\bar{\tau}}$, $N = \frac{\sigma'_{II}}{\bar{\tau}}$, $N_{min} = \frac{\sigma'_{III}}{\bar{\tau}}$, $\bar{\tau} = \sigma_{mises}/\sqrt{3}$, being ν the Poisson ratio and α the pressure sensitivity in the Drucker-Prager model.

Following this strategy, the measured orientation of the fracture plane $\Theta \approx 54$ represents a pressure sensitivity parameter of $\alpha \approx 0.13$ in the Drucker-Prager yield model (Eq. 1.16).

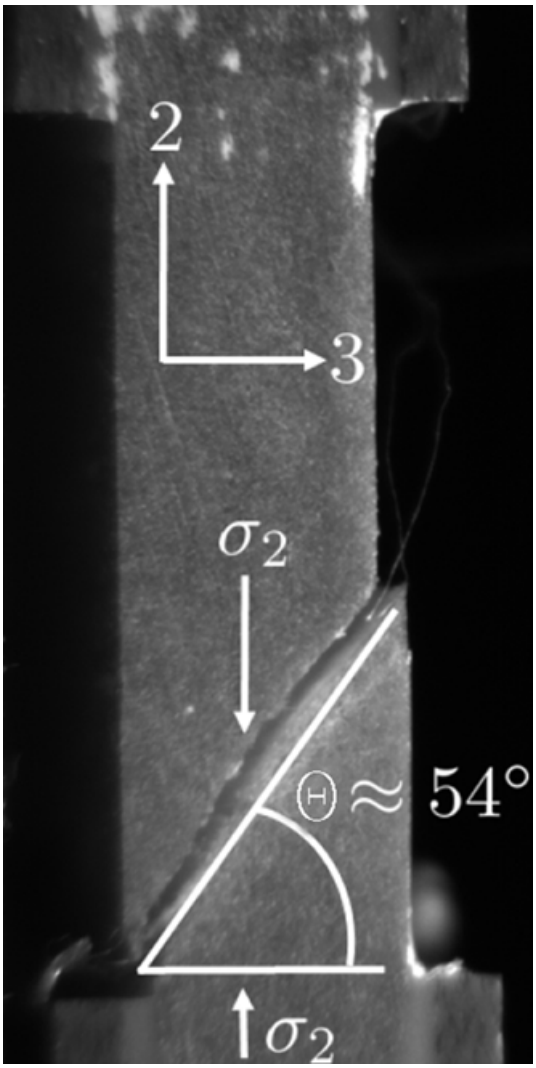

Figure 2.4: Fracture plane orientation on the lateral surface of an E-glass/MTM 57 loaded under transverse compression.

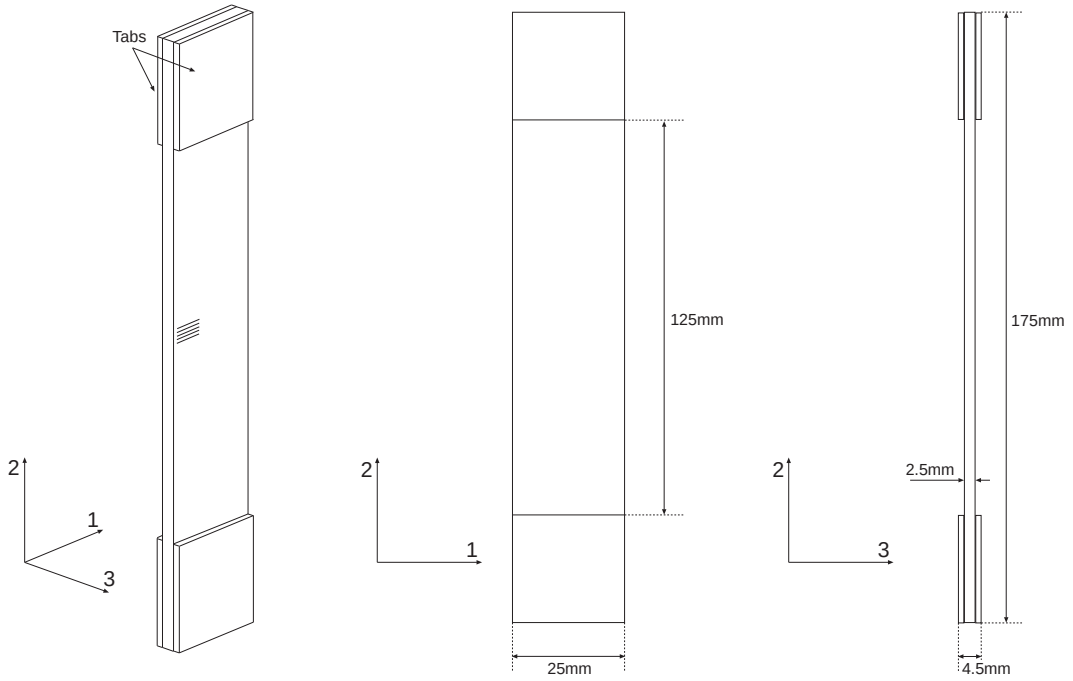

Figure 2.5: Schematic picture of the transversal compression test specimens.

2.3 Tensile properties determination

The transverse tensile properties of the unidirectional E-glass/MTM 57 epoxy laminate were determined according to the ASTM D 3039 standard test method. The specimens were machined according to the standard with the dimensions specified in Fig. 2.5. The result of the tensile test is extremely sensitive to specimen imperfections. For this reason, special precautions were taken to avoid notches, undercuts, rough or uneven surfaces caused during the specimen preparation. The samples were machined from the laminate panels by water-lubricated precision sawing, using an abrasive cutting disk. Aluminum tabs were bonded to the specimen surface to prevent gripping damage. Finally, every specimen was inspected and measured, and showed flat and parallel edges within the tolerances specified in the standard.

Transverse tension tests were carried out in a servo-hydraulic mechanical testing machine Instron 8803, under stroke control using a constant cross-head speed of

1mm/min while the load and the displacement were measured using a 10kN Instron load cell and the displacement transducer of the mechanical rig, respectively. The transversal strain was measured using an Instron strain gauge extensometer with 50mm of gauge length.

2.3.1 Experimental results

Ten transversal tension tests were performed on unidirectional $[0]_{14}$ E-glass / MTM 57 coupons according to the ASTM 3039 standard. The failure mode was determined by the visual inspection of the broken specimens. In many samples, due to the brittle behavior of the laminate in the direction perpendicular to the fibers, the failure was localized near to the tabs or inside the grip region. These failure modes were considered unacceptable, according to the ASTM standard, and the measurements were rejected. The stress-strain curves ($\sigma_2 - \epsilon_2$) of six specimens broken inside the gauge area are plotted in Fig. 2.6. The stresses were computed from the readings of the load cell and the cross sectional area of the specimen. The deformations were acquired with the extensometer reading. The tests were reproducible and exhibited a limited experimental scatter. The shape of the stress-strain curves were the expected for unidirectional polymer composites subjected to transversal tension. The behavior was linear until failure, showing the expected brittle behavior of the laminated. The slope of the curve was used to compute the transverse elastic modulus of the composite $E_2 \approx 11 \pm 2$ GPa, the linear region ended with the catastrophic failure of the laminate. The measured strength of the material was $Y_t \approx 50 \pm 5$ MPa.

2.4 Concluding remarks

The transversal tensile and compressive properties of a unidirectional laminate of E-glass/MTM 57 epoxy resin were determined by means of the ASTM standard test methods.

Transverse compression tests showed an elasto-plastic behavior of the laminate prior to its catastrophic failure. The measurements carried out during the compressive tests provided an elastic modulus of $E_2 \approx 12 \pm 2$ GPa and a compressive strength

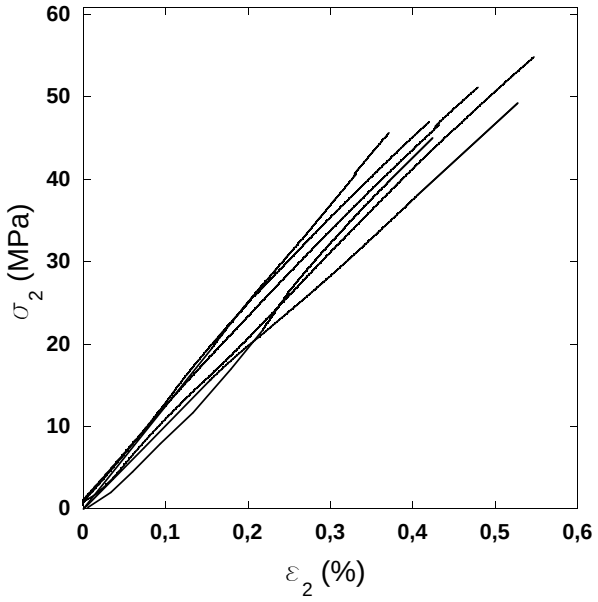

Figure 2.6: Transverse tension stress *vs.* strain curves for E-glass/MTM 57 epoxy specimens.

of $Y_c \approx 160 \pm 10$ MPa. The fracture was always localized parallel to the fiber direction and oriented at an angle slightly higher than 45° with respect to the direction perpendicular to the loading axis. It was assumed that the orientation of the fracture plane was related with the pressure sensitivity of the matrix. Thus, an estimation of the pressure sensitivity parameter was provided by the measurement of the fracture inclination.

Tensile tests showed a linear and elastic behavior of the composite until its catastrophic failure for limited deformations. The fracture was parallel to the fiber direction and perpendicularly oriented to the loading direction. Tensile test provided an elastic modulus of $E_2 \approx 11 \pm 2$ GPa and a strength of $Y_t \approx 50 \pm 5$ MPa.

Chapter 3

Micromechanical characterization of FRPs constituents

The properties of the fibers, matrix and fiber-matrix interfaces determine the mechanical performance of FRPs. In this chapter, an innovative micromechanical characterization framework is developed to measure the properties of the laminate constituents within the actual composite ply. These techniques are then employed to obtain the matrix and interface properties of the E-glass/MTM 57 laminate.

3.1 Matrix characterization

As a first approximation, the matrix properties can be determined by conventional mechanical tests for rigid plastics on specially manufactured neat resin coupons. Two ASTM standards define the conditions for tensile and compression tests at low uniform rate of loading (D7078, 2003a,b). The tensile test specimens have a parallel gauge section of rectangular cross section, broadening at each end to provide attachment points for the grips (dog-bone-shaped specimens). The preferred specimens for the compression tests shall be in the form of straight cylinders or prisms whose length is twice its principal width or diameter, in order to prevent barreling. During the tests, contacting or remote extensometers are used to measure the separation between

Table 3.1: Mechanical properties of the epoxy matrix and the glass fibers provided by the prepreg supplier.

	E	ν_m	σ_{yc}	σ_{yt}
	(GPa)		(MPa)	(MPa)
MTM 57 epoxy matrix	3.35	0.35	120	70
Glass fibers	74	0.2		

two points on the gauge length, while a load cell records the applied force. This experimental information directly provides Young's modulus, and the compressive or tensile yield stresses. Following these procedures, the prepreg supplier (Advanced Composite Group, UK) measured the basic matrix properties and the results are summarized in Table 3.1.

However, the properties provided by neat resin coupons may not be representative of the mechanical behavior of the matrix in the laminate. For instance, matrix mechanical properties are controlled by the cross-linking process that takes place during the cure cycle and hence by the exact processing conditions which could be significantly modified by the presence of a large volume fraction of fiber reinforcement. Therefore, the optimum solution proposed in this work, relies on using *in situ* testing techniques to characterize the ply components at the microstructural level.

3.1.1 Determination of the Young's modulus and compressive yield stress

It has been recently shown that the mechanical properties of the matrix can be determined by means of instrumented nanoindentation into resin pockets between the fibers on a polished cross-section of the composite (Rodríguez et al., 2011). Special care must be taken to place the nanoindentations sufficiently far away from the fibers in order to avoid their constraining effect which induce a marked stiffening effect. However, it is not difficult to find rich resin locations far away from any fiber because of the inhomogeneous fiber arrangement at the microscopic level (Fig. 3.1).

During the nanoindentation, a very small diamond hard tip is pressed into the

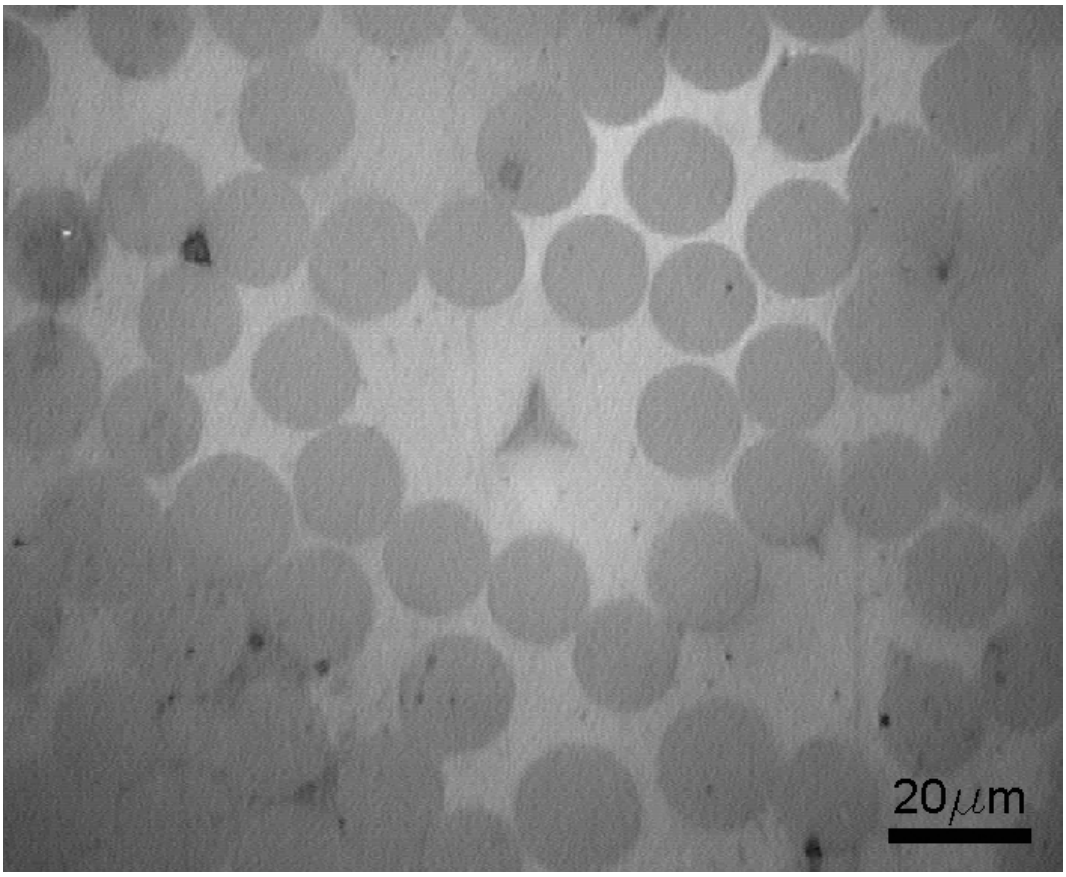

Figure 3.1: Optical microscopy image of the cross section of the E-glass/MTM 57 unidirectional laminate showing a nanoindentation in a resin pocket.

sample. The load in the tip is increased as it penetrates, the applied load and the displacement into the surface are continuously recorded with high precision instruments, obtaining the load-displacement curves showed in Fig. 3.2.

The hardness of materials can be determined from the indentation test as the ratio between the applied force (P) and the projected contact area (A).

$$H = \frac{P}{A} \tag{3.1}$$

The contact area can be estimated from microscopical observations of the residual imprint, but this practice can be difficult to be carry out at the small scale of the nanoindentation tests. Oliver and Pharr (1992) developed an analytical method to determine the elastic properties from the load-displacement curves measured during the test. This technique has been extensively used to obtain the elastic modulus through instrumented indentation experiments, the proposed method relates the initial slope of the unloading curve, S in Fig. 3.2, with the contact area and the elastic modulus (E) by

$$E_r = \frac{\sqrt{\pi}}{2}\frac{S}{\sqrt{A}} \tag{3.2}$$

where A is computed from the geometrical characteristics of the tip and the record of the displacement into the surface. E_r stands for the reduced modulus, which takes into account the effect of a non-rigid indenter

$$\frac{1}{E_r} = \frac{(1-\nu^2)}{E} + \frac{(1-\nu_i^2)}{E_i} \tag{3.3}$$

being E and ν the Young's modulus and the Poisson's ratio for the specimen and, E_i and ν_i the same parameters for the indenter.

However, this method provides inaccurate predictions when it is applied to study non-linear, viscoelastic or plastic materials. The pile-up and sink-in of the material on the edges of the tip during the indentation process (Fig. 3.3) produces a variation on the contact area, resulting in unaccuracies when the Oliver and Pharr method is applied. Moreover, the imprint area is also afected by relaxation phenomena due to the viscoelastic behavior of the polymers. In these cases, the analytical study of the indentation process becomes unreachable.

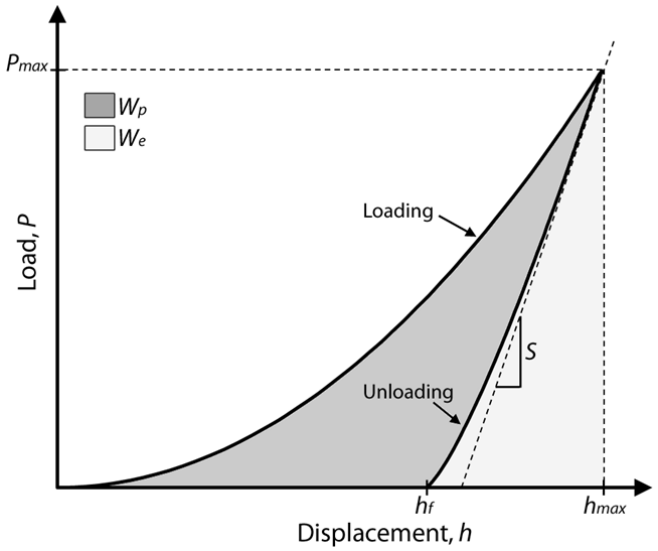

Figure 3.2: Schematic of the load-displacement curve obtained from the nanoindentation.

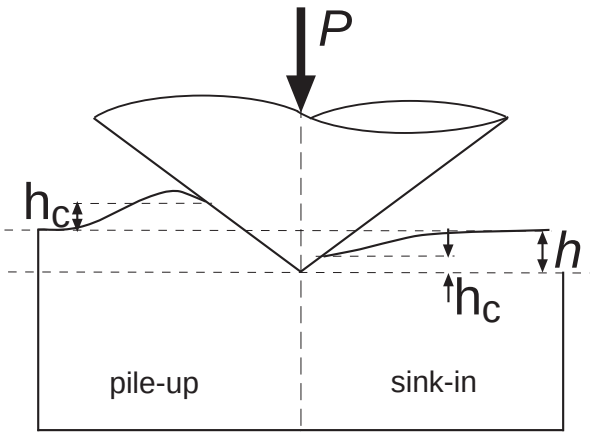

Figure 3.3: Diagram showing pile-up/sink-in effects affecting the contact area of indentation.

Cheng and Cheng (2004) simulated the indentation process on a wide variety of elasto-plastic materials, they obtained the following relation between the elastic fraction work and the reduced modulus

$$\frac{W_e}{W_t} \approx 1 - 5\frac{H}{E_r} \tag{3.4}$$

being W_t and W_e the total and the elastic work of the indentation process, respectively.

In addition, Cheng and Cheng also provided an accurate method for the yield stress determination in elasto-plastic materials. This method has been successfully applied to metallic alloys, but it can not be accurately applied to materials whose yielding presents pressure sensitivity. Rodríguez et al. (2011) extended this methodology to pressure dependent materials by simulating the indentation on materials following a Drucker-Prager yield criterion. As a result, they proposed two empirical curves. The first one relates the fraction of elastic and total work with the ratio between the hardness and the yield stress, while the second curve relates the latter magnitude with the ratio between the yield stress and the elastic modulus. These curves were obtained for a wide range of pressure sensitivities parameters, making possible their use for many different materials (Fig. 3.4 a and b).

Assuming that the yield behavior of the epoxy matrix is pressure sensitive, the compressive strength and the elastic modulus were experimentally determined through the nanoindentation process according to the Rodríguez et al. (2011) methodology.

Five nanoindentation tests were performed, using a Berkovich indenter tip, into the resin pockets of the material microstructure. The load was applied at a constant rate of 0.2μm/s, the results were reproducible and the scatter was very limited. A representative load-displacement curve obtained in the process is plotted in Fig. 3.5. The curve shows the load branch, produced when the tip is pressed into the specimen surface, up to an approximate depth of 2μm. Then, the load is held during 10 seconds to reduce the creep deformation upon the unloading, which could induce inaccuracy predictions of the material properties. Following the hold period, the indenter is lifted off from the surface, producing the unloading branch which is supposed to be completely elastic.

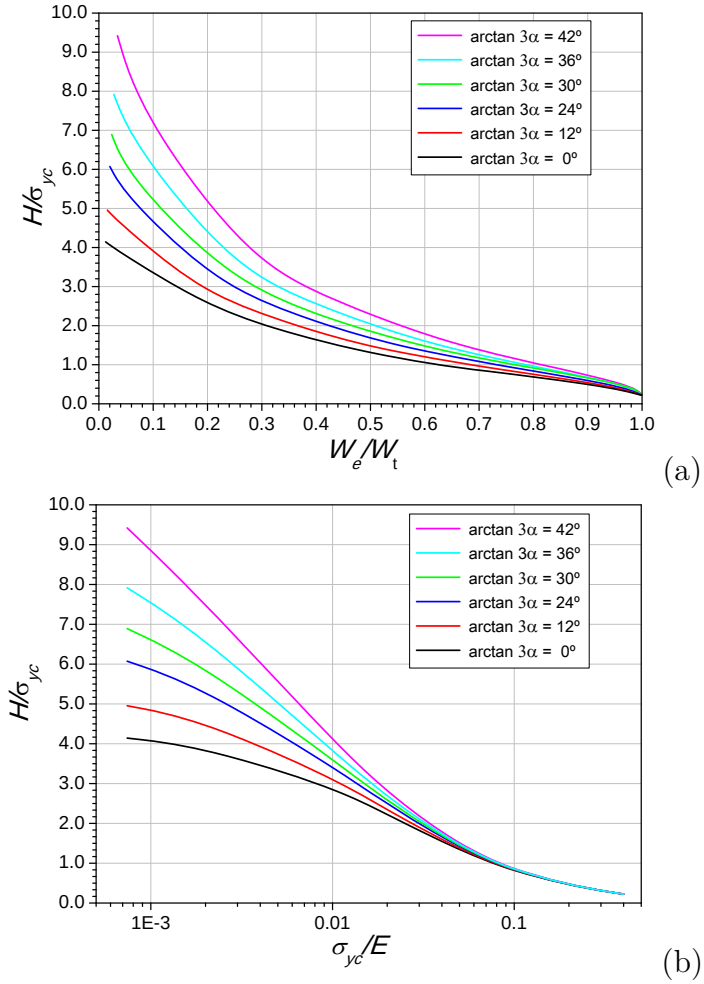

Figure 3.4: (a) H/σ_{yc} as a function of the elastic fraction work and (b) as a function of the ratio between the compressive yield stress and the reduced modulus. α stands for the pressure sensitivity parameter of the Drucker-Prager yield criterion (Eq. 1.16). Adapted from Rodríguez et al. (2011)

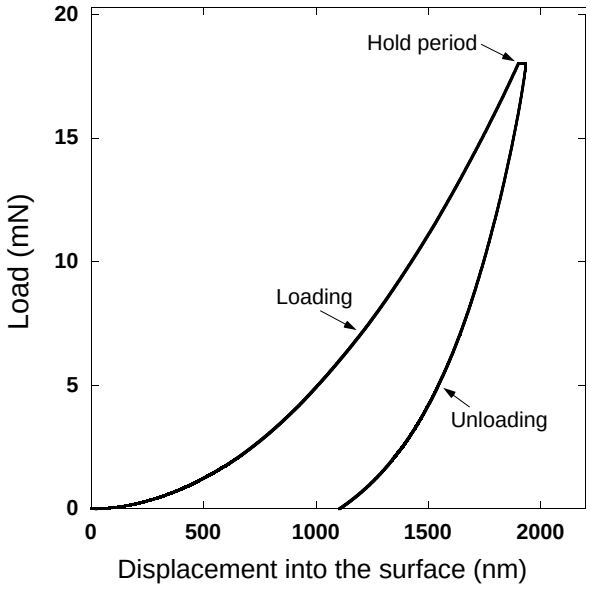

Figure 3.5: Load-displacement curve obtained from the nanoindentation into the a matrix pocket of the FRP E glass/ MTM 57 epoxy.

The measurement of the areas under the loading and unloading branches (Fig. 3.5) provided a ratio between the elastic and the total work of $W_e/W_t \approx 0.42$. In addition, the hardness $H \approx 200$MPa was obtained through eq. 3.1 by measuring the applied load and computing the contact area from the geometrical characteristics of the tip and its displacement into the specimen surface. From these parameters and the pressure sensitivity of the material ($\alpha \approx 0.13$, obtained in the previous chapter), it is straightforward to obtain the compressive yield stress of the epoxy matrix through the curves of Fig. 3.4(a). Following this strategy, the determined compressive yield stress was $\sigma_{\text{yc}} \approx 105$MPa. Finally, a Young's modulus of $E \approx 3.5$GPa was obtained through the application of the curves of Fig. 3.4(b).

The experimental technique employed to characterize the mechanical properties of the matrix has been carried out without manufacturing special specimens from resin coupons and taking into account the exact processing conditions of the FRPs and the influence of the temperature, water absorption, etc. This methodology has been widely assessed for different pressure dependent materials, including thermoplastic and thermosetting polymers (Rodríguez et al., 2011). In addition, the experimentally determined values of the elastic modulus and the compressive yield stress of the epoxy matrix were in good agreement with the properties reported by the material supplier (Table 3.1). This fact confirmed that the presence of fibers did not substantially modified the mechanical behavior of the epoxy resin.

3.2 Fiber-matrix interface characterization

3.2.1 Interface strength determination

Several experimental methods exist to characterize the interfacial adhesion between fiber and reinforcement in composite materials, such as the fragmentation test, the pull-out test and the push-in and push-out tests. No ideal test exists, but each of them presents advantages and disadvantages which should be considered to select the most adequate for a specific purpose.

The fragmentation test was early proposed to study the interfaces in metal matrix composites (Kelly and Tyson, 1965), and later it was extensively employed to study

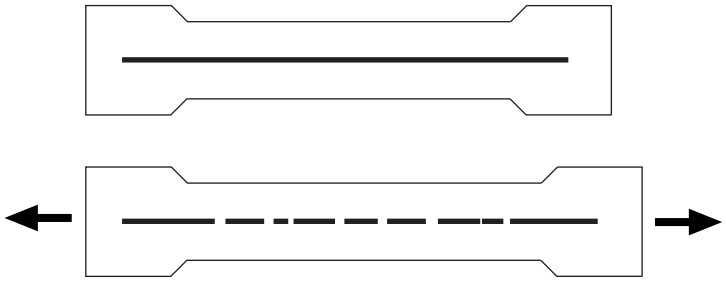

Figure 3.6: Schematic illustration of the fragmentation test.

FRP (Zhou et al., 2001; Young et al., 2001). In this test, a single fiber is embedded within a resin tensile specimen (Fig. 3.6). If the fiber failure strain is lower than the corresponding to the matrix, the fiber breaks at several points. Thus, the elastic recovery of the embedded broken fiber is controlled by the elastic behavior of the matrix and the strength of the interface.

The fragmentation test is adequate for composites with ductile matrices and brittle fibers. On the contrary, for tough fibers embedded in a brittle matrix are considered, the pull-out test usually provides better results (Zhandarov and Mäder, 2005). This test is based on pulling out a partially embedded fiber from a resin specimen (Fig. 3.7). In this test, the load is transfered from the fiber to the interface. Then, the decohesion happens when the shear strength in the interface is reached.

The fragmentation test, pull-out test and their other modifications consisting on embedding a single fiber in the matrix material can be very valuable, but testing conditions are sometimes technically difficult to fulfill. In addition, they might suffer from the fact that the results cannot be readily scaled-up to a real composite laminate because a single isolated fiber is generally not representative of the mechanical and physico-chemical conditions encountered in real composites (Kharrat et al., 1997). To overcome these difficulties, the push-in and push-out tests can be carried out in a specimen of the real composite.

In the push-in test, a single fiber is pushed by means of a nanoindentor on a cross-section of a bulk specimen of the laminate until interface decohesion occurs (Fig. 3.8). The main advantage of this technique is that it does not require any labo-

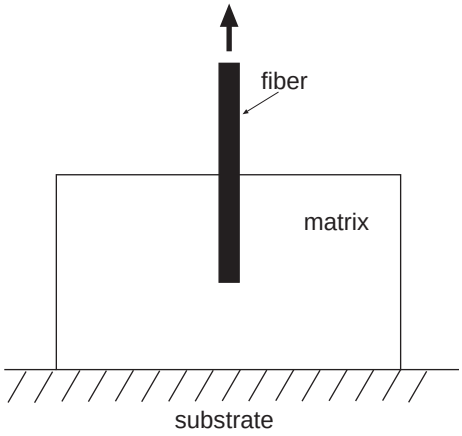

Figure 3.7: Schematic illustration of the pull-out test.

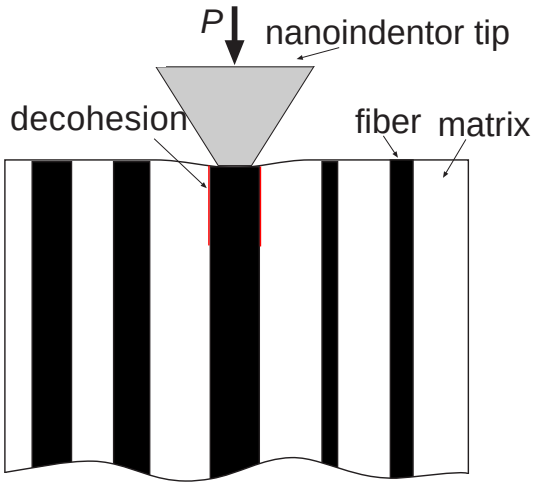

Figure 3.8: Schematic illustration of the push-in test.

rious sample preparation but interpretation is somehow difficult because the length of the debonded interface below the surface is not known. Thus, the results should be analyzed in terms of a shear lag model or FE simulations of the test (Molina-Aldareguía et al., 2011).

The push-out test requires harder specimen preparation, but provides a more

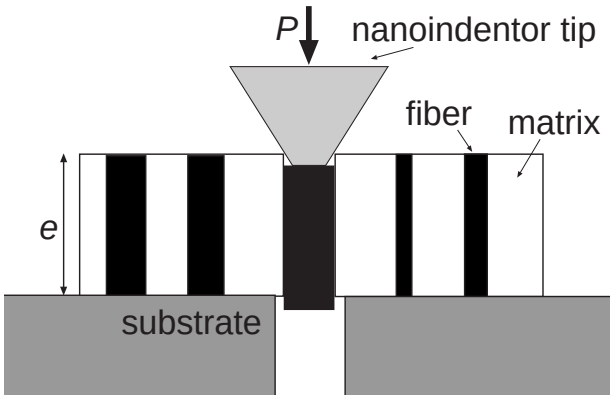

Figure 3.9: Schematic illustration of the push-out test.

direct measurement of the interface strength (Godara et al., 2010). This test is similar to a push-in test but is carried out on a very thin specimen. The force applied on the fiber leads to the complete fiber/matrix debonding and the fiber is pushed out through out the plate (Fig. 3.9). The shear stress at the instant of fiber push-out provides the direct measurement of the interface strength ($S_{\text{interface}}$) given by

$$S_{\text{interface}} = \frac{P_{\max}}{2\pi r e} \tag{3.5}$$

where $P_{\max}$ is the maximum applied load and e is the specimen thickness.

In this work, the push-out test was selected to evaluate the strength of the fiber/matrix interface. Very thin specimens were prepared by polishing the cross section of E-glass/MTM 57 unidirectional laminate up to a thickness of $\approx 20 - 30\mu$m. These specimens were thin enough to allow decohesion over the whole interface and the complete push out of the fiber. The samples were mounted on a MTS Nanoindenter XP instrumented equipped with a flat-punch tip with a diameter of 10μm. The indentations were performed at a displacement rate of 50 nm/s. Fibers covering a wide range of diameters (between 10 and 30μm) and different environments (positions of the neighboring fibers) were selected for the test. After the tests, the specimens were inspected in the scanning electron microscope. The front and back side of the tested slices were observed to check that the pushed fibers were completely

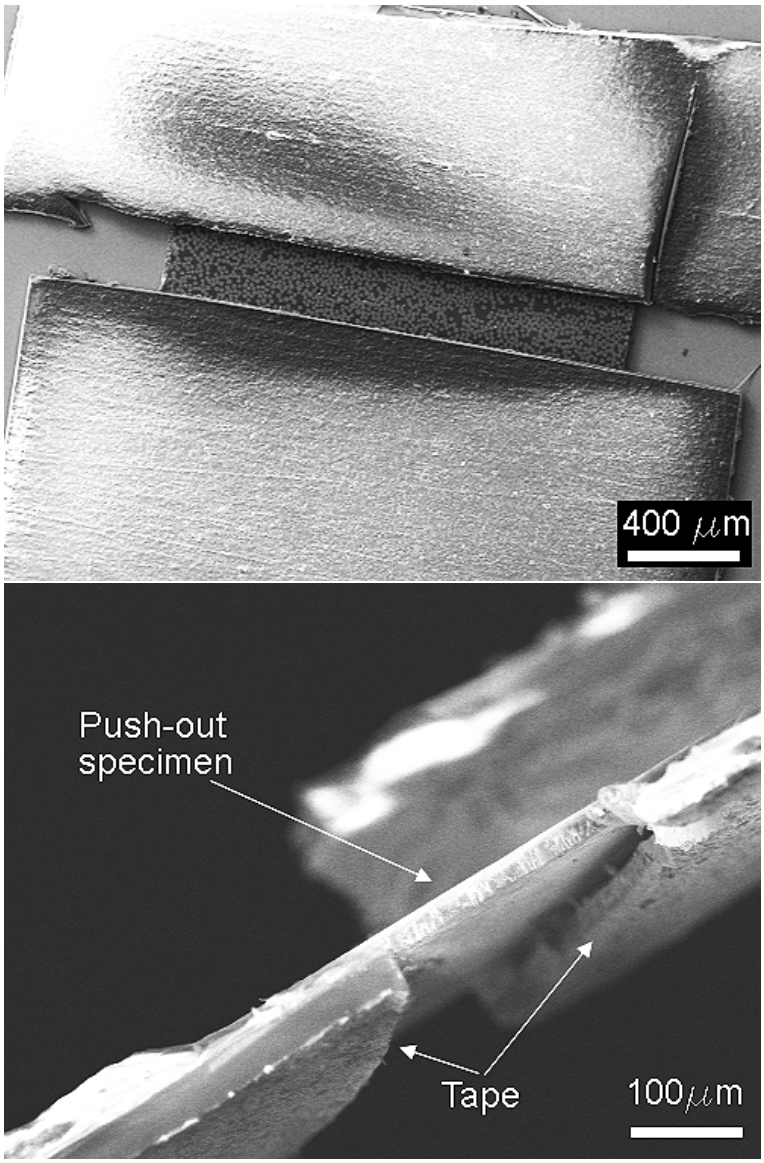

Figure 3.10: SEM images of the front and section of the push-out test specimens.

debonded from the matrix. Furthermore, the micrographs were employed to measure the diameter of the tested fibers and the thickness of the specimen (Fig. 3.10).

The main stages of the push-out test and the typical resulting load-displacement curve are shown in Fig. 3.11. The curve presents an initial region dominated by the elastic bending of the thin plate, followed by a region controlled by the elastic

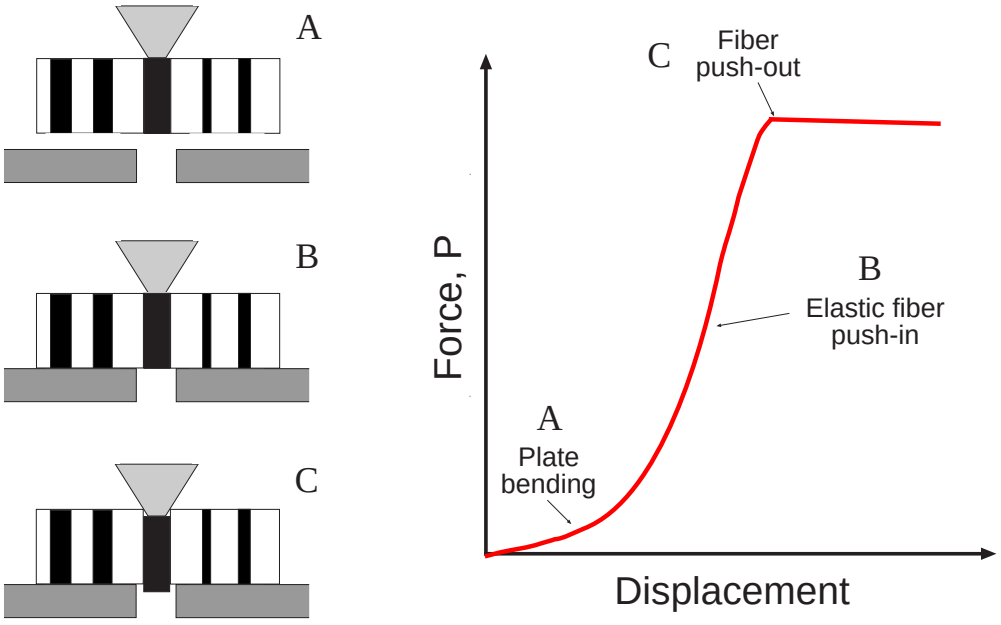

Figure 3.11: Schematic of the push-out process and load-displacement curve resulting form the test.

deformation of the fiber and the surrounding matrix until maximum load. From this point on, the test becomes instable, since the nanoindenter is load-controlled, showing a plateau of constant load in the load-displacement curve.

Once the applied load is measured by the nanoindentor, and the specimen thickness and the diameter of the fibers obtained through the SEM observations, it is possible to calculate the interfacial shear stress through Equation 3.5. The resulting shear-displacement curves were plotted in Fig. 3.12. The maximum stress for each curve gives the shear strength of the fiber-matrix interface. The average measured value was $S_{\text{interface}} \approx 75 \pm 15\text{MPa}$. The relatively high value of the uncertainty was possibly caused by the constrained effect of the nearest neighboring fibers. This values are in accordance with other measurements carried out in this material by the push-in technique (Molina-Aldareguía et al., 2011).

In addition, it is interesting to notice that the shear strength of the interface could be considered as a lower bound for the tensile yield stress of the matrix. The SEM

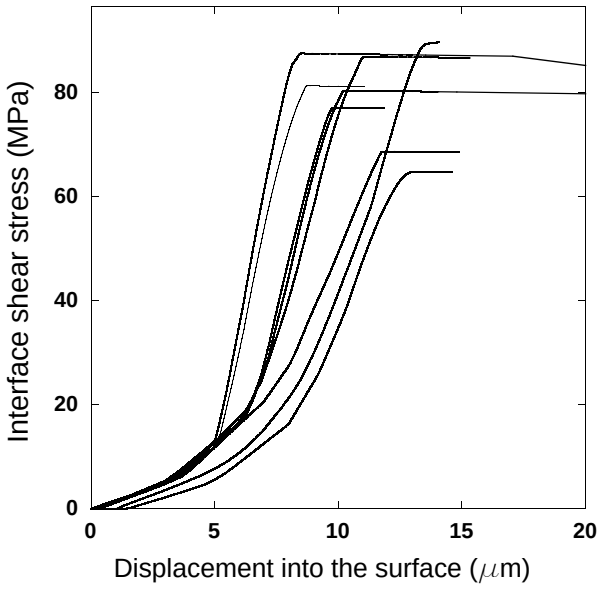

Figure 3.12: Experimental shear stress-displacement curves obtained form the tests.

observation of the fibers extracted during the push-out test (Fig. 3.12) showed that the fibers were debonded through an "interfacial" failure, without any fragmentation of the matrix around the extracted fibers (Fig. 3.13). Therefore, considering that the shear stresses during the push-out did not produced the failure of the matrix, it is possible to establish that $\sigma_{\text{yt}} \geq S_{\text{interface}}$.

It should be noted, however, that the push-out test does not provide the actual value of the normal interface strength, which may be different from the shear strength. Ogihara and Koyanagi (2010) studied the interface failure under combined shear and normal stress states in a glass fiber/epoxy composite. Their experiments were conducted by using specimens reinforced with a single fiber, whose angle from the loading direction was varied in order to create the different stress states in the interface. The study concluded that the shear strength of the interface was higher than its normal strength and proposed a quadratic stress criteria to represented the debonding of the interface. Finally, assuming that the shear strength was 1.5 times

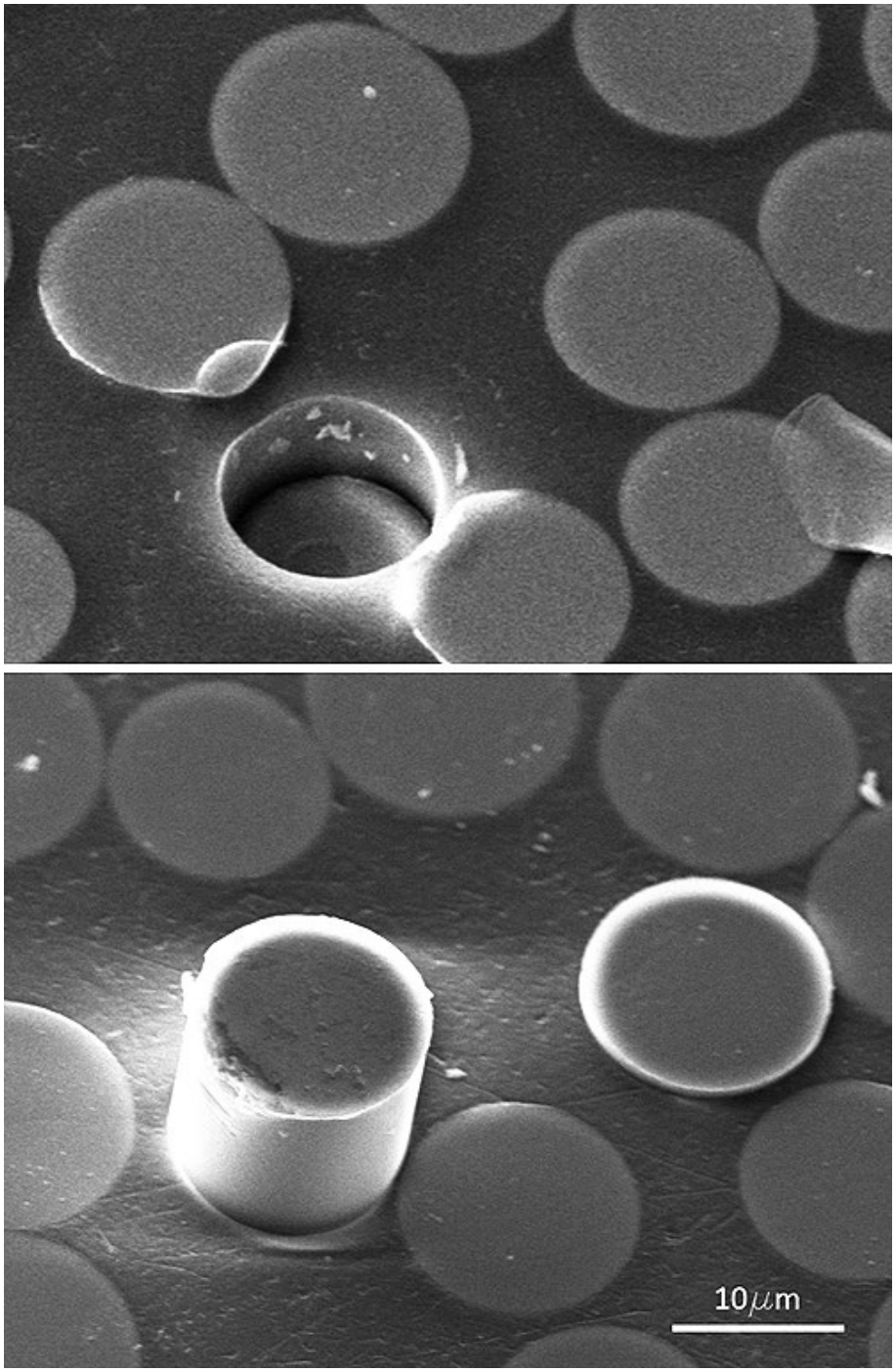

Figure 3.13: Front and back sides of the specimen after the push-out test.

higher than the normal strength, the proposed criteria fitted the experimental failure envelope of the interface under the combined shear and normal stresses.

In view of these results, the normal interface strength of the E glass/MTM 57 was computed in our case from the shear strength obtained form the push-out test as $N_{\text{interface}} = S_{\text{interface}}/1.5 \approx 50$ MPa.

3.2.2 Interface toughness

The strength of the fiber-matrix interface is a key property to control the mechanical behavior of composites because it determines the initiation of the interface fracture. In addition, the behavior of the interface during the fracture process is also highly relevant. For example, if the interfaces between fibers and matrix were perfectly brittle, the fibers would be completely debonded when the stresses at any point of the interface reached the value of the strength. This might lead to the sudden and catastrophic failure of the composite, and it would be impossible to make safe structures with FRPs.

For this reason, the characterization of the fracture energy of the fiber-matrix interface is an essential step to develop realistic micromechanical models of the composite. The fracture energy of the fiber-matrix interfaces has been studied by means of tests in single-fiber specimens (Zhou et al., 1999), but it cannot be easily determined through nanomechanical testing techniques in the actual composite ply. For this reason, the push-out test performed with a load-controlled nanoindenter was not able to provide an experimental value of the fracture toughness. In this case, due to the absence of valid direct micromechanical measurement, the fracture energy was indirectly evaluated through micromechanical simulations of the overall composite behavior during its fracture (Chapter 4).

3.3 Concluding remarks

The mechanical properties of the matrix and the matrix-fiber interfaces have been characterized *in situ* by means of nanoindentation and push-out test.

In the case of the matrix, the elastic modulus and the compressive yield stress were determined by carrying out nanoindentation tests into the resin pockets of the composite microstructure. The properties obtained with this nanomechanical characterization were in good agreement with those provided by the material supplier. The mechanical behavior of the matrix can be modeled then by a continuous damage model which explicitly takes into account the effect of the hydrostatic pressure on the yielding and the quasi-brittle failure under tensile loads. The pressure sensitivity of the epoxy was obtained through the observation of the fracture surfaces of the unidirectional laminate under transverse compression.

The shear strength in the fiber-matrix interfaces was experimentally obtained by means of the push-out test, and it was estimated for the case of normal opening.

As a final conclusion, the experimentally characterized values of the mechanical properties of the matrix and fiber-matrix interfaces are compiled in the following Table.

Table 3.2: Mechanical properties of the epoxy matrix and the fiber-matrix interface obtained through nano-characterization techniques.

E_m	σ_{yc}	σ_{yt}	$N_{\text{interface}}$	$S_{\text{interface}}$
(GPa)	(MPa)	(MPa)	(MPa)	(MPa)
3.5	105	$\geq$75	50	75

Chapter 4

Fracture behavior of FRPs

Unidirectional FRPs loaded in tension perpendicular to the fibers fail by the initiation and propagation of a narrow crack perpendicular to the loading axis. The microscopical inspection of the fracture process showed that the failure was caused by the decohesion of the fiber-matrix interfaces and the failure of the matrix ligaments localized between debonded fibers (Fig. 4.1).

Considering the aforementioned failure mechanisms, it is possible to state that the fracture behavior of the composite depends on the strength and the fracture energy of the matrix and fiber-matrix interfaces. Some of the critical micromechanical parameters which determine the failure properties of the composite can be independently measured or taken for well-established values in the literature (see Chapter 3). However, the fracture energy of the microconstituents cannot be directly determined within the actual composite ply.

In this Chapter, the fracture behavior of E-glass/MTM 57 unidirectional laminate in the direction perpendicular to the fibers is studied by means of tensile and three-point bending tests. In addition, in order to evaluate the effect of the micromechanical parameters on the fracture behavior of the final composite, both experimental test were simulated through embedded cell approaches and their results were assessed with the experimental measurements.

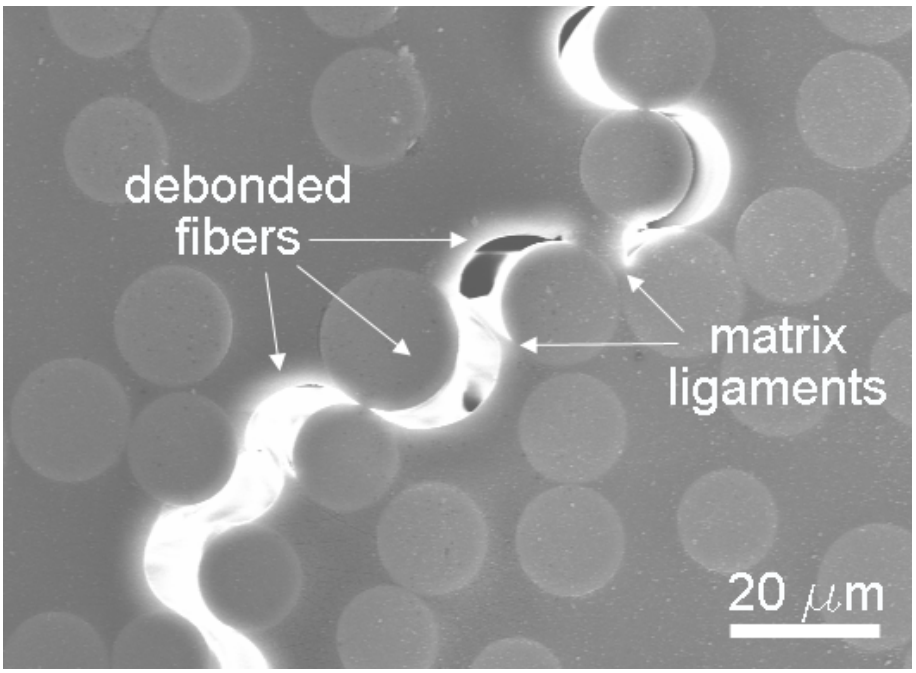

Figure 4.1: Scanning electron micrograph showing the fracture process zone during a three-point bending test of a E-glass / MTM 57 unidirectional laminate.

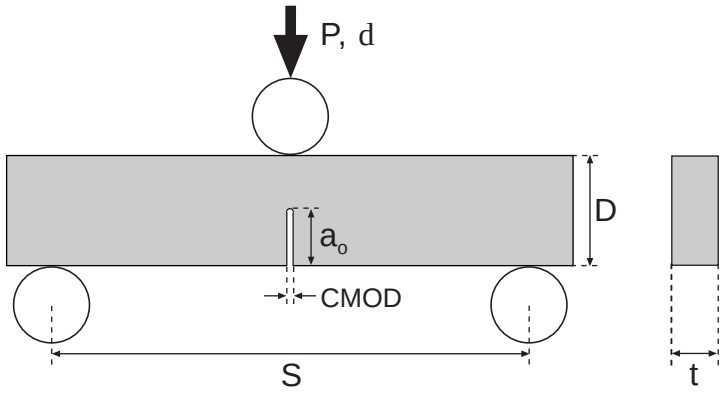

Figure 4.2: Schematic picture of the three-point bending tests specimens.

4.1 Experimental techniques

Two kinds of tests were carried out to characterize the fracture behavior of the laminate, transversal tensile tests and stable three-point bending test with prismatic notched specimens.

The tensile strength in the direction perpendicular to the fibers was obtained according to the ASTM D 3039 standard test method. The description of this test, the experimental procedure and the obtained results have been already presented in Chapter 2. These tests provided an elastic modulus of $E_2 \approx 110 \pm 20$GPa and a strength of $\sigma_t \approx 50 \pm 5$MPa.

The fracture behavior of the composite was determined using notched three-point bending tests. Beams with a depth (D) of 2.8mm, a span (S) of 12mm and a thickness (t) of 2mm were machined from unidirectional panels of E-glass/MTM 57 with the fibers perpendicular to the beam axis and parallel to the thickness direction. A notch was machined in the central section of the beams with a thin diamond wire, to a notch root diameter of $\approx 130\mu$m. The initial notch depth (a_o) was 0.5D (Fig. 4.2).

Fracture tests were carried out in an Instron 5543A electromechanical testing machine, under stroke control at a constant cross-head speed of 100μm/min. The applied load (P) and the displacement of the loading point (δ) were continuously

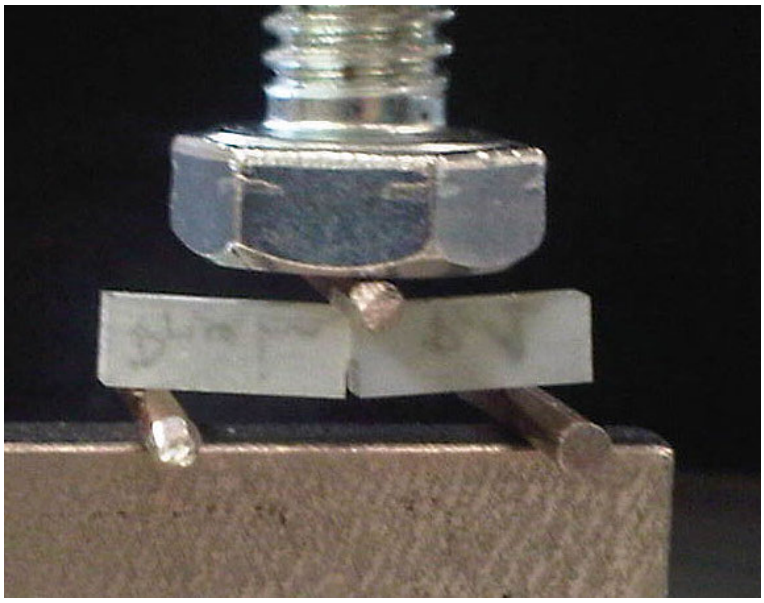

Figure 4.3: Detail of the experimental setup for the three-point bending test.

recorded during the tests with a load cell of 1kN and the cross-head position, respectively. In addition to this, the displacement of the loading point and the crack mouth opening displacement (CMOD) were more accurately measured through the digital image correlation of the specimen images acquired during the tests. To this end, one of the specimen surfaces was scratched with SiC paper of 250 grit to create a pattern of points of random gray level which could be tracked by the analysis software. Digital image correlation (DIC) is a non-contact method to measure displacements and strains through the registration and tracking of images of the specimen. In the three-point bending test DIC was used as an extensometer to measure the distance between two points, but it can also provide the full field strain measurement on the specimen surface. Additional information about this technique is provided in Chapter 5.

To obtain additional information about the damage micromechanisms in FRPs, three fracture tests were carried out inside the scanning electron microscope. To this end, the specimens were coated with gold by sputtering and the bending test fixture was set up in a micro-electro-mechanical testing machine (Kammrath & Weiss Ten-

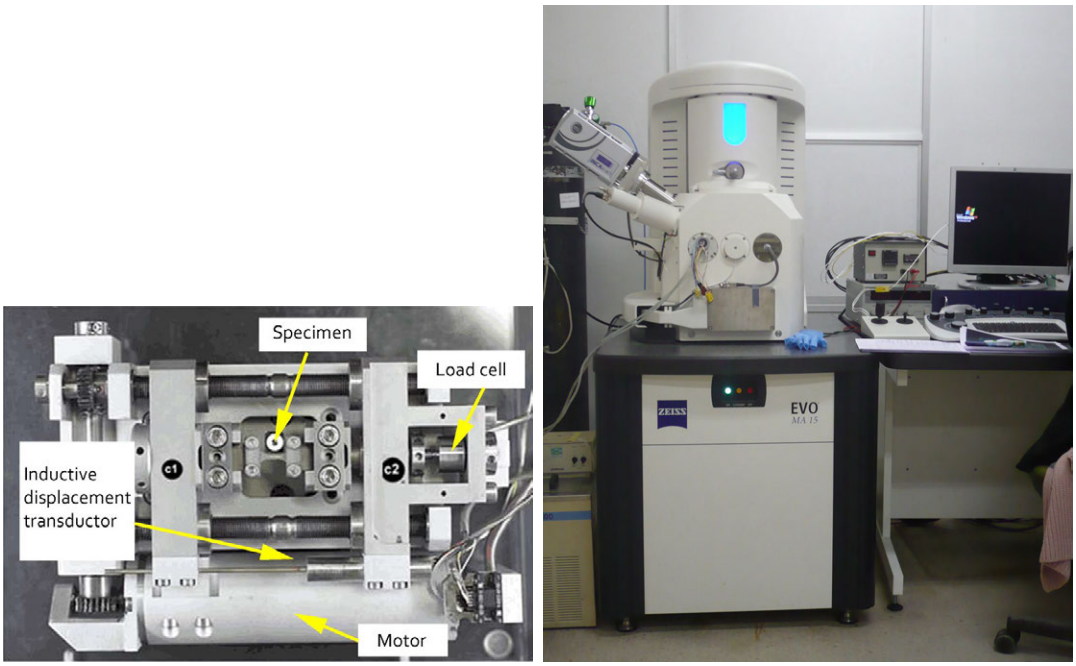

Figure 4.4: (a) Miniaturized testing machine. (b) Scanning electron microscope where the testing machine is inserted.

sile/Compression Stage) inside a scanning electron microscope (Zeiss EVO MA-15). Micrographs of the central zone of the three-point bending specimens, the region where the fracture process was localized, were taken at different magnifications (50X, 85X, 250X and 500X). The actuator was stopped at regular intervals of 5μm and micrographs of the previously selected area were taken at the same magnification. Load was not recorded because actual load signal (up to 16N) could not be distinguished from the background noise given the fact that the load cell was designed for a maximum load of 10kN.

4.2 Experimental results

Five fracture tests were carried out on the transverse section of unidirectional $[0]_{14}$ E-glass/MTM 57 laminate. The load-CMOD curves obtained from these tests are plotted in Fig. 4.5. The curves were very repetitive within the experimental scatter,

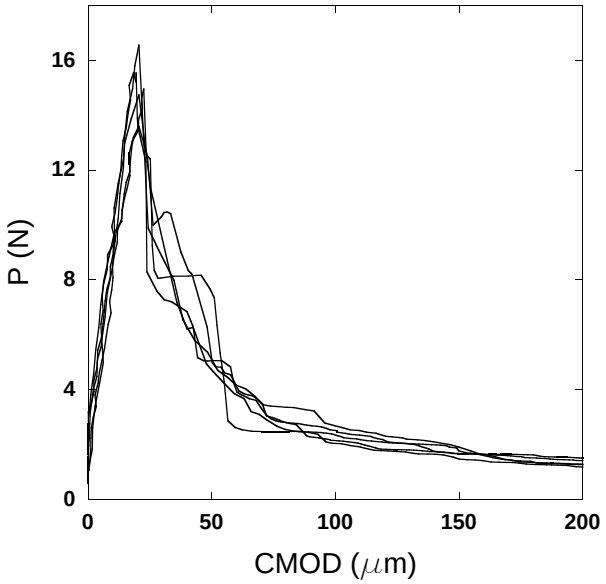

Figure 4.5: Load-CMOD curves of the fracture tests of E-glass / MTM57 unidirectional laminates in the cross section.

which shows that the fracture mechanisms of this laminate in the transverse section was reproducible. The load-CMOD curves exhibited a linear and elastic behavior up to the peak of maximum load which was attained for a value of 15 ± 2N. After this peak, load fell to the 60% or 70% of its maximum value. The sudden drop in the load indicated the nucleation and development of the failure at the notch root. Continuing with the test, the load stably decreased with the propagation of the crack through the specimen section. The test ended with the splitting of the beam in two halves.

The fracture tests provided two important parameters to characterize the fracture behavior of this composite. The first one was the composite fracture energy, G_f, computed as the area under the P-δ curve divided by the area of the initial ligament, as

$$G_f = \frac{\int_0^\infty \mathrm{P}\mathrm{d}\delta}{(D - a_o)t} \tag{4.1}$$

The second parameter was the characteristic length, which was defined by Hilleborg et al. (1976) as

$$l_{ch} = \frac{EG_f}{{Y_t}^2} \tag{4.2}$$

where E is the elastic modulus and Y_t is the tensile strength of the material. This parameter is directly related to the cohesive zone extension during the fracture process, and is commonly used to characterize brittleness of materials. The smaller the l_{ch} value, the more brittle the material. The average value of the fracture energy provided by the five tested specimens was $G_f = 400 \pm 50 \mathrm{J/m^2}$ and, considering the elastic modulus and the tensile strength obtained through the transverse tensile tests, it resulted in a characteristic length of 1.8 $\pm$0.9 mm.

4.2.1 Fracture mechanisms

The *in situ* SEM fracture tests of the transverse section of unidirectional E-glass / MTM57 laminate allowed to study the main micromechanisms of deformation and failure developed during fracture.

The initial loading of the specimen did not produce the development of failure neither inelastic deformations. The first noticeable damage mechanism appeared for a displacement of the load application point around $\approx 40 \mu$m. Initially, the crack involved only the fiber-matrix interfaces (Fig. 4.6c), and the matrix ligaments between debonded fibers absorbed the deformations without noticeable signs of damage. Continuing with the test, the crack tip advanced breaking the fiber-matrix interfaces toward the load application point. Simultaneously, the matrix ligaments bridged the crack opening making difficult its advance until the final failure of the ligaments (Fig. 4.6d). This process continued until the final splitting of the specimen in two halves.

The experimental observation of the fracture process described above showed that fiber-matrix interfacial decohesion followed by the fracture of the matrix ligaments were the two only active failure mechanisms during the fracture of the cross section of the composite. The sequence of this process indicated that the strength in tension of the fiber-matrix interfaces is lower than the tensile fracture stress of the matrix, in

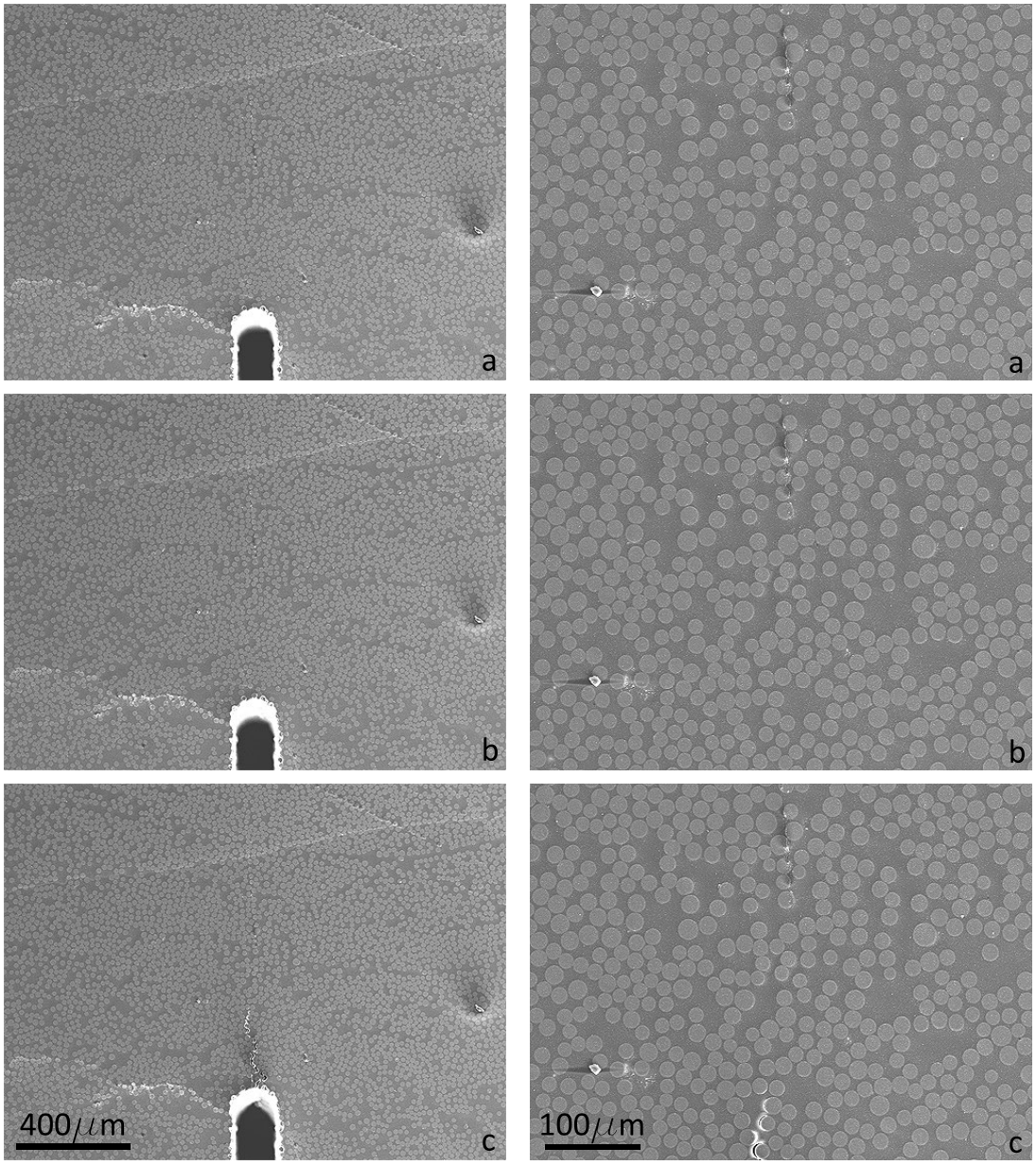
a
a
b
b
400μm
c
100μm
c

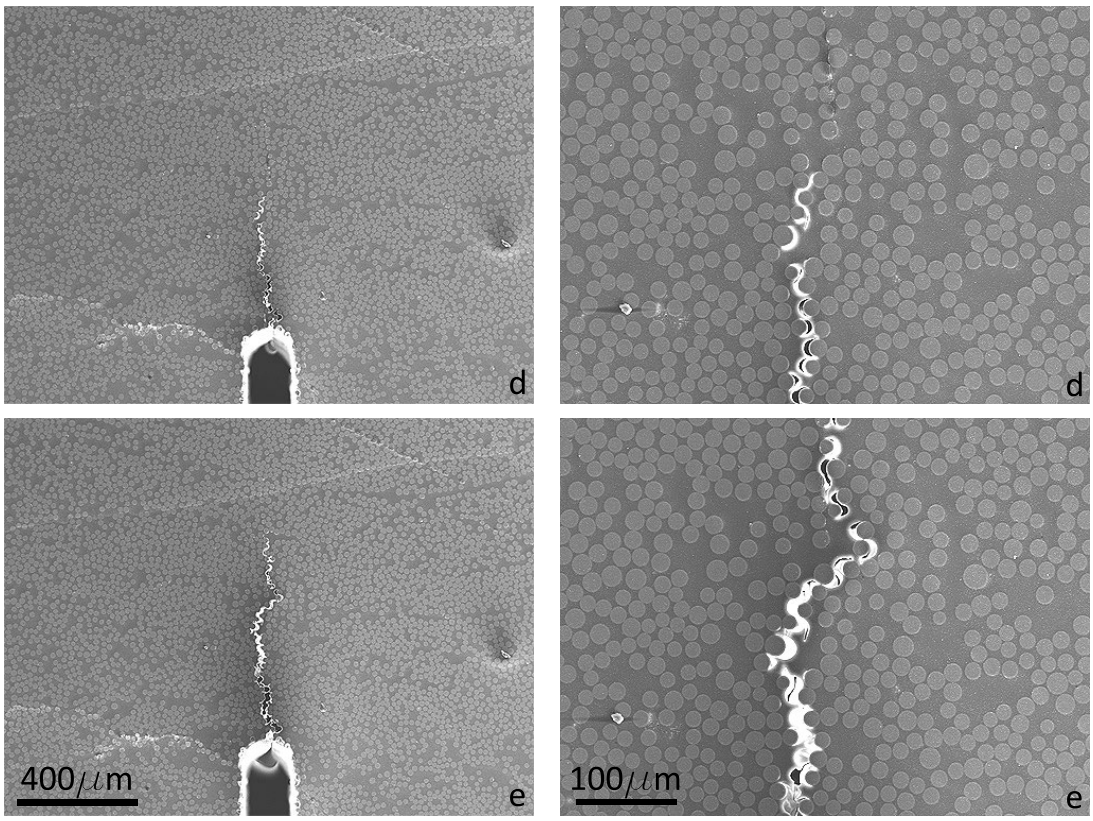

Figure 4.6: Scanning electron micrographs showing the sequence of the crack propagation during a three-point bending test. The displacement of the load application point corresponds to (a) 20μm, (b) 30μm, (c) 40μm, (d) 50μm and (e) 60μm.

good agreement with the experimental measurements obtained by nanoindentation techniques (see Chapter 3). Moreover, the SEM inspection showed two toughening mechanisms. First, the circular shape of the cross section of the fibers produced the deflection of the crack tip, increasing the area of the fracture surface and consequently the final fracture energy. Second, the matrix ligaments between debonded fibers bridged the crack opening, making the failure to progress slower. Considering the intricate failure and toughening micromechanisms developed during the composite fracture, it was not possible to directly extract any information about the fracture energy of the microconstituents from the measurements of the three-point bending test. For this reason, the fracture of the composite was studied by means of the micromechanical simulations of the transverse tension and three-point bending tests.

4.3 Computational model

The transverse tension and three-point bending tests were simulated by means of multiscale models based on the embedded cell approach. These simulations allowed to study the failure micromechanisms and the influence of the fracture energy of the microconstituents on the macroscopic fracture behavior.

4.3.1 Simulation of the transverse tension test

The geometric model to simulate the tension test comprised the cross section of the central region of the transverse tension specimens up to a distance of 3.75mm. Following the strategy of the embedded cell, the central region was divided into two different zones (Fig. 4.7). The center of the model reproduced the actual microstructure the composite material, while the remaining sample above and below the microstructured part was assumed to be an homogeneous solid. The simulation was focused on capture the maximum load achieved in the transverse tension tests. In the microstructured region, the cross section of the laminate was represented by a random and homogeneous dispersion of circular fibers embedded in an epoxy matrix. The fiber volume fraction within the microstructured region of the embedded cell was 54%, the same as in the real material.

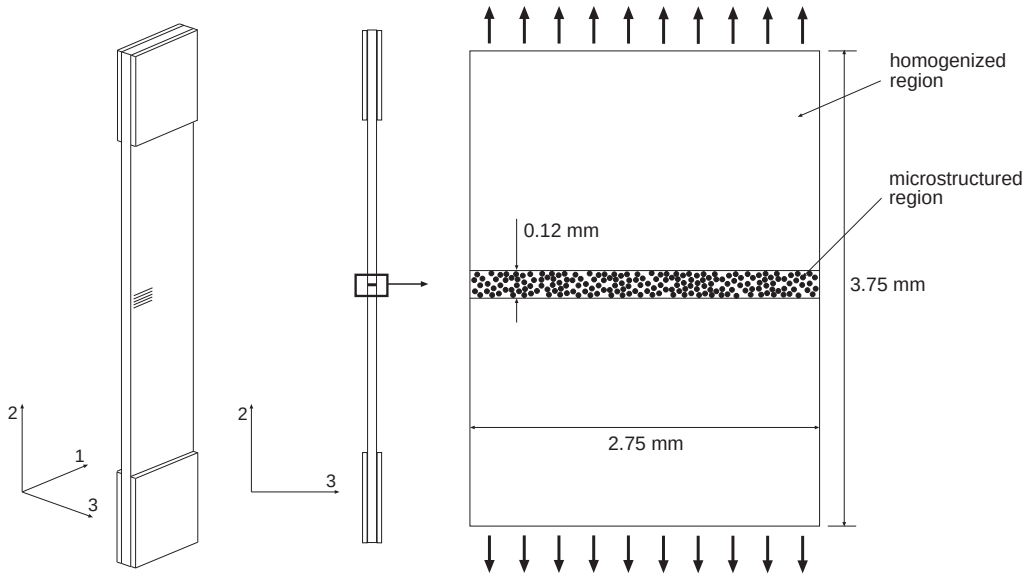

Figure 4.7: Schematic of the transverse tension test specimen and the embedded cell used in the numerical simulations.

The mechanical behavior and the main damage mechanisms experimentally observed in the microconstituents were included in the simulations through the adequate constitutive models. Glass fibers were modeled as linear, thermo-elastic and isotropic solids, their elastic constants were provided by the material supplier and they are compiled in Table 4.1. The epoxy matrix was represented by an isotropic, elasto-plastic solid, its Young's modulus was experimentally determined by nanoindentation techniques and the Poisson ratio was provided by the material supplier. The elastic constants of the epoxy matrix employed in the simulations are also shown in Table 4.1. Moreover, the plastic and damage of the matrix was represented by the model for quasi-brittle materials presented in Chapter 1 (Equation 1.37). A pressure sensitivity parameter $\alpha = 0.13$, extracted from the observation of the fracture plane orientation in the transverse compression tests (Chapter 2), was considered. The compressive strength was measured by means of nanoindentation and it provided a value of $\sigma_{\text{yc}} = 105\text{MPa}$ (Chapter 3). Finally, the tensile strength employed in the

Table 4.1: Mechanical properties of the epoxy matrix, glass fibers and the homogenized material employed in the numerical model.

E_m (GPa)	ν_m	E_f (GPa)	ν_f	E_h (GPa)	ν_h
3.5	0.35	74	0.2	11	0.3

model was $\sigma_{\text{yt}} = 75\text{MPa}$, a lower bound obtained from the push-out tests (Chapter 3).

Fibers and matrix were discretized with 6-node isoparametric modified triangles in plane strain condition (CPE6M in Abaqus (2010)) with integration at three Gauss points. The fiber-matrix decohesion was included in the simulations using interface elements, which were inserted between both constituents (COH2D4 in Abaqus, Camanho and Dávila (2002)). The final model had approximately 700000 nodes and 375000 elements.

The strength of the interfaces was obtained from push-out tests which provided N=50MPa and S=75MPa, for the normal and shear interface strength respectively (see Chapter 3). It was assumed that the fracture energy of the matrix and the interfaces has not a key influence on the final load achieved in the transverse tensile test. As a first approximation, the fracture energy values for the matrix and the interface were obtained from the literature (Kinloch and Young, 1983; Zhou et al., 2001) and, for the sake of simplicity, they were assumed to be the equal for both components ($G_f^{\text{interface}} = G_f^{\text{matrix}} = 150\text{J/m}^2$).

Finally, the homogeneous region of the model was represented by a linear, elastic and isotropic solid. Its elastic modulus was obtained from the average result of the transverse tension tests (Chapter 2), and the Poisson's coefficient was supposed to be a mixture of those of the composite microconstituents according to its volumetric fraction. These properties are also compiled in Table 4.1.

Mesh sensitivity analysis

In the numerical simulations, the epoxy matrix was represented by a continuum damage model. It is well known that this kind of models may lead to mesh-dependent

results, which should be avoided in the numerical study of the composite failure. Simulations of uniaxial tension tests of a dog-bone specimen meshed with three different discretizations were carried out to check the adequate implementation of the model and the correction of the mesh sensitivity.

The same geometry was meshed with linear quadrilateral elements for plane strain conditions (CPE4 in Abaqus (2010)). Three different element sizes were employed to obtain the meshes plotted in Fig. 4.8. The same material properties were impose to the models. The material behaved as a linear elastic solid up to the tensile yield stress. From this point on, damage arose in the material producing a macroscopical softening, which is determined by the fracture energy. The contour plot of the strain in the loading direction for the three different discretizations showed that the strain is localized in a band with the thickness of the element size (Fig. 4.9).

As a result, the smaller the element size, the higher the values of strain were localized in the contours. However, the force-displacement curves obtained from the simulations showed that the energy dissipated during the fracture was the same in the three discretizations (Fig. 4.10), which confirmed the mesh objectivity of the implementation of the damage model.

Results

The transverse tensile behavior of the E-glass/MTM57 laminate was simulated using the computational model described above. The tension load was introduced by applying a relative displacement between the upper and lower surfaces, as depicted in Fig. 4.7.

The computational model reproduced the main deformation and failure micromechanism experimentally observed, as well as the macroscopical behavior. The mechanisms of deformation and fracture in transverse tension can be observed in Fig. 4.11a, which show a detail of the damage at the interfaces. Failure was initiated by the nucleation of interface cracks, which grew along the interfaces. The stress concentration in the matrix ligaments between decohesionated fibers promoted its damage, and the macroscopic crack advanced through the specimen by the linking up of the debonded

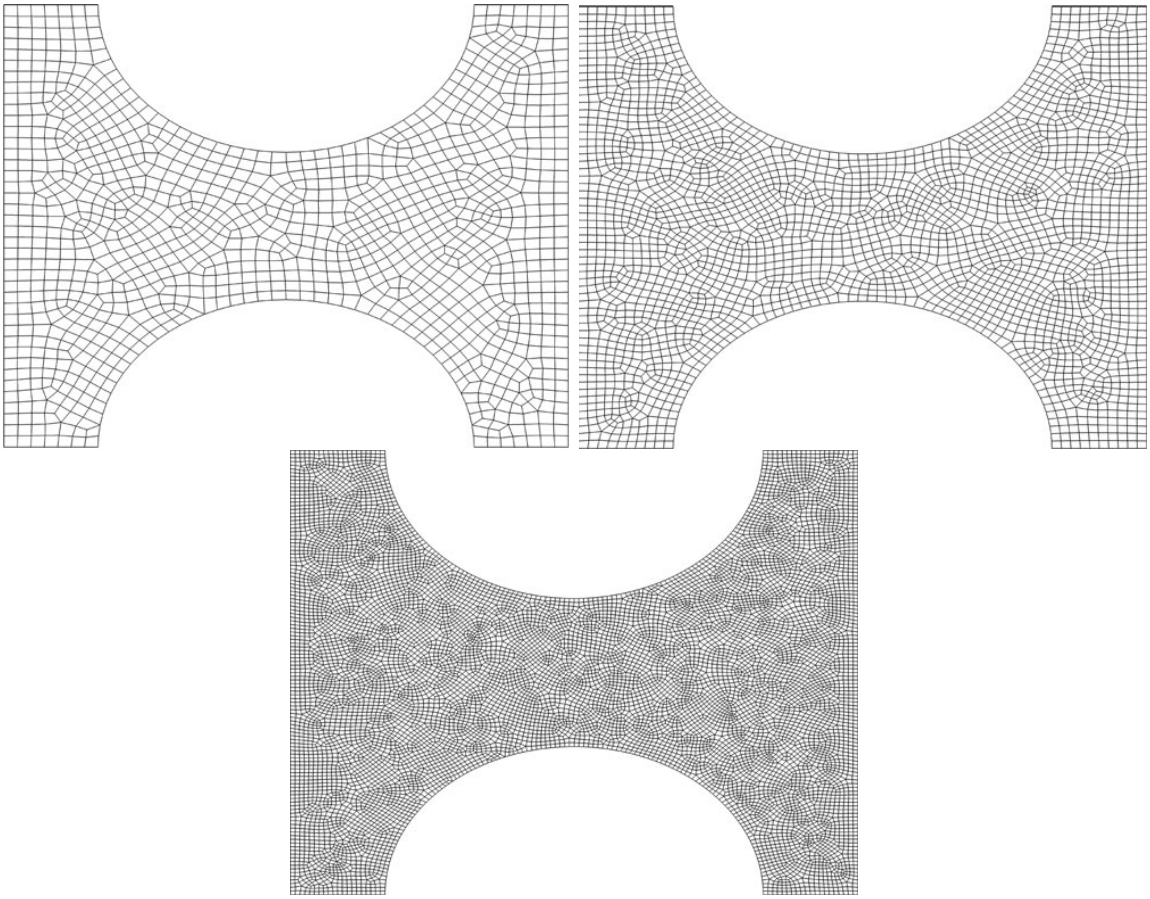

Figure 4.8: Three discretizations employed to studied the mesh sensitivity of the damage model.

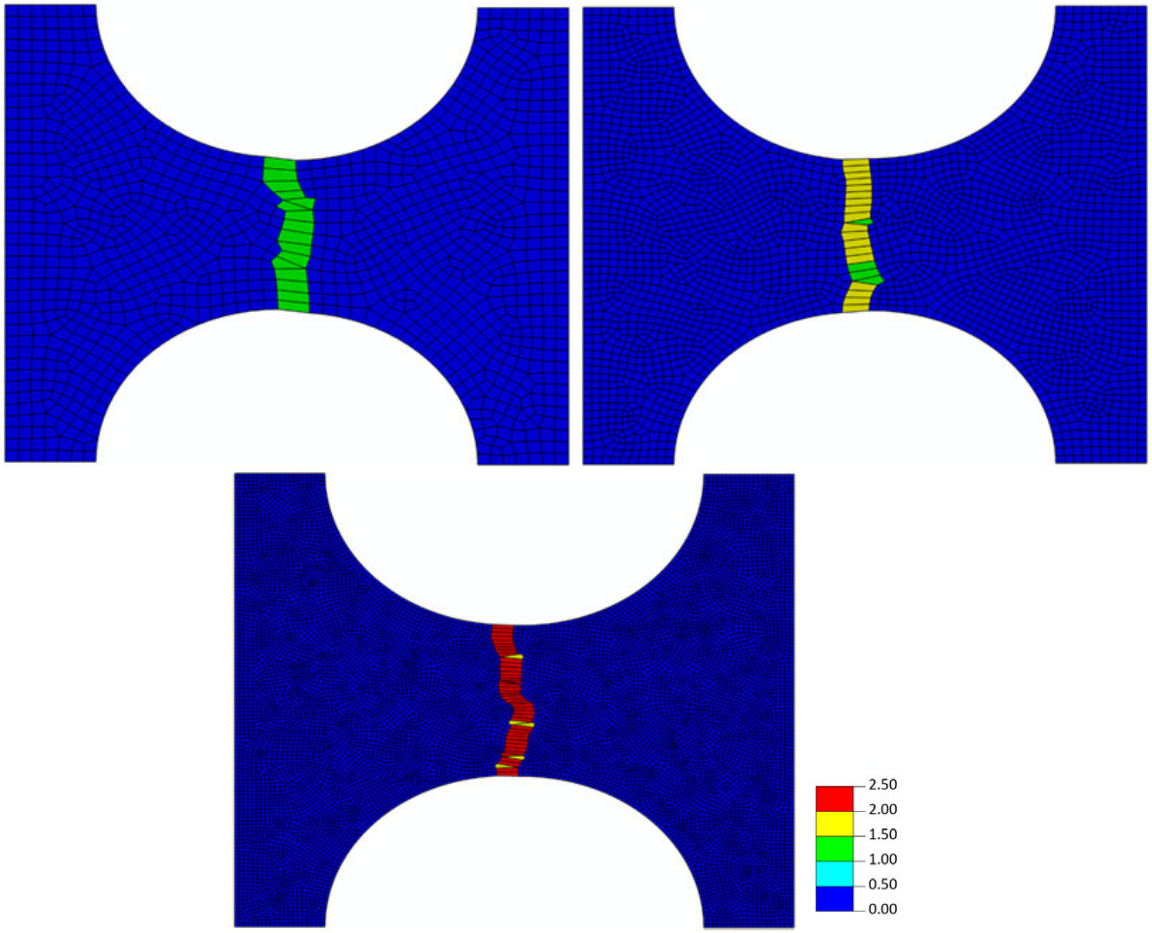

Figure 4.9: Contour plot of the strains in the x-direction for three different discretizations.

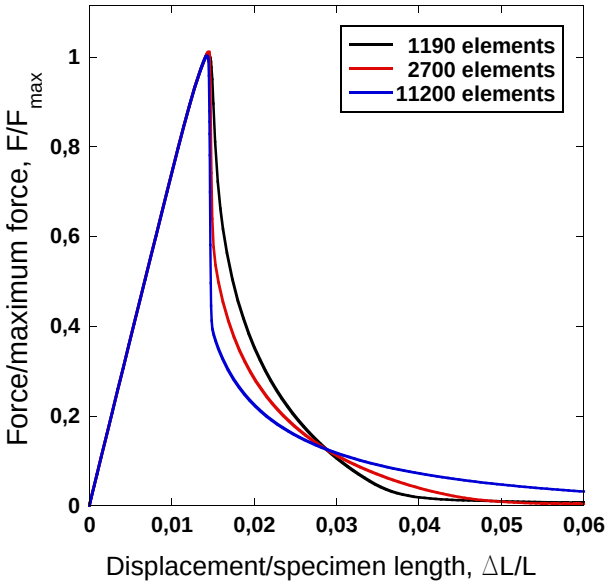

Figure 4.10: Force-displacement curves obtained from the three different mesh discretizations.

interfaces, resulting in a sudden decrease of the load-carrying capability of the material (Fig. 4.11b).

The stress-strain curves obtained from the numerical simulations are plotted together with the experimental measurements in Fig. 4.12. The numerical simulations of the mechanical behavior of the laminate under transverse tension predicted a brittle fracture behavior, in accordance with the experimental observations. The stress-strain curve showed an initial linear elastic loading of the laminate until its sudden failure. An elastic modulus of 11.7GPa was obtained from the slope of the loading branch. The maximum load attained in the simulations provided a value of 64.3MPa for the strength of the laminate.

The elastic modulus predicted by the numerical simulation was in good agreement with the experimental measurements of the transverse compression and tension tests. However, the strength of the laminate predicted by the numerical model overestimated by 30% the experimentally obtained value (50MPa). The mismatch between the experiments and numerical predictions could be a consequence of the presence of defects which triggered the early failure of the material or inaccuracies in the determination of the strengths of the matrix and fiber-matrix interfaces.

4.3.2 Simulation of the three-point bending test

The experimental results presented in previous sections have demonstrated that the fracture behavior of the E-glass/MTM 57 unidirectional laminate is rather complex due to the interaction of different deformation and damage micromechanics. Numerical simulations that take into account the details of the microstructure are therefore critical to understand the role played by the different mechanisms.

The embedded cell approach, previously used to simulate the transverse tension test, is employed here to study the transverse fracture behavior of the E-glass/MTM 57 unidirectional laminate by means of the simulation of the three-point bending test. These simulations are important to study in detail the processes of deformations and fracture and to understand which factors control the failure of the laminate. In particular, these simulations will allow to ascertain the influence of the microstructural parameters on the quantitative values of the fracture toughness of the composite.

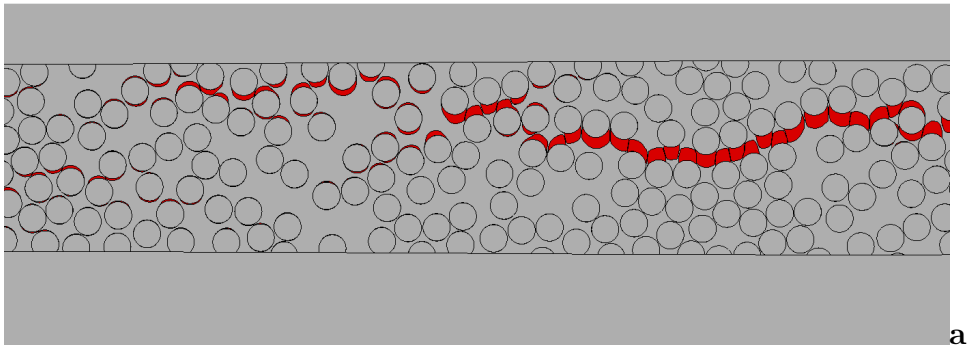

a

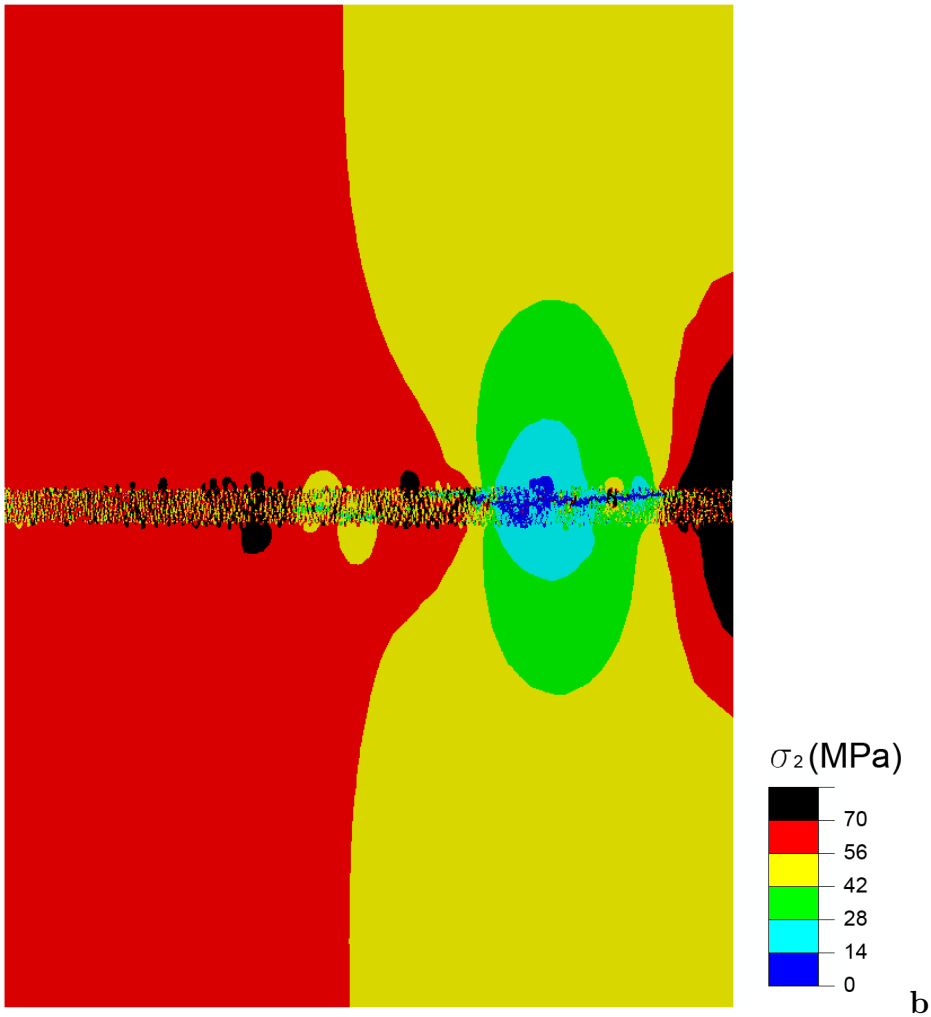

b

Figure 4.11: (a) Detail of the damage at the fiber-matrix interfaces. (b) Contour plot of the stresses in the load direction.

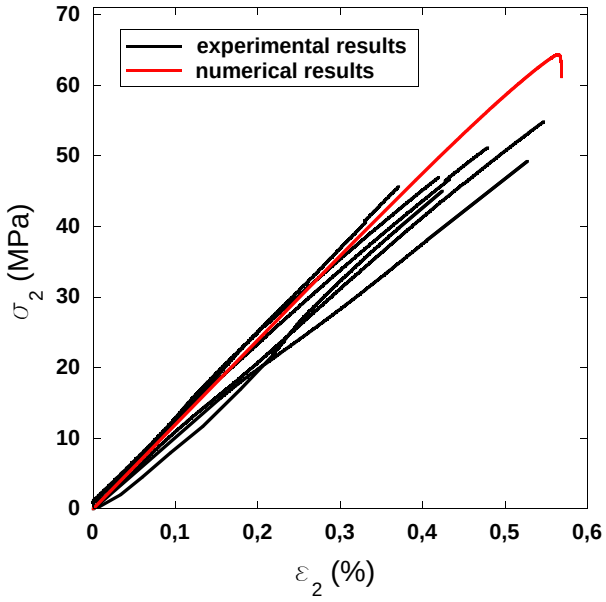

Figure 4.12: Experimental and numerical stress *vs.* strain curves obtained from the transverse tension tests of E-glass/MTM 57 laminate.

The simulations were focused on capturing the area under the load-displacement curve attained in the fracture test during the crack propagation along the specimen. The geometric model to simulate the fracture behavior of the composite beam was divided into two zones, according to the strategy of the embedded cell approach. An area of the specimen in front of the notch was represented by a random and homogeneous dispersion of circular fibers embedded in an epoxy matrix. The fiber volume fraction within the microstructured region of the embedded cell was 54%, the same as in the real material. The remaining beam was assumed to be a homogeneous solid (Fig. 4.13).

The area in which the microstructure is explicitly accounted corresponds to the region were the fracture process will be localized, as it has been observed in the experiments. In this region, the main damage mechanisms experimentally observed, namely fracture of the matrix and the fiber-matrix interface, were included in the numerical models.

The fibers and the matrix were discretized with 6-node isoparametric modified triangles in plane strain condition (CPE6M in Abaqus (2010)) with integration at three Gauss points. The fiber-matrix decohesion was included in the simulations using interface elements, which were inserted between both constituents (COH2D4 in Abaqus, Camanho and Dávila (2002)). The final model had approximately 350000 nodes and 180000 elements.

Fibers were modeled as linear, elastic and isotropic solids, their elastic constants were taken from the manufacturer's data sheet and they are given in Table 4.1. The epoxy matrix was represented by an isotropic, elasto-plastic solid, following the damage-plasticity model for quasi-brittle material. The elastic material properties were the same already employed to simulate the transverse tension test in the previous section and they are also shown in Table 4.1. The plastic and damage behavior of the matrix were controlled by the parameters experimentally obtained, a pressure sensitivity of $\alpha = 0.13$ and material strengths of $\sigma_{\text{yt}} = 75\text{MPa}$ and $\sigma_{\text{yc}} = 105\text{MPa}$. The normal and shear strength employed to simulated the fiber decohesion were not modified form the previous section (N=50 and S=75 MPa).

Three different values of the fracture energy of the matrix and the interfaces (10,

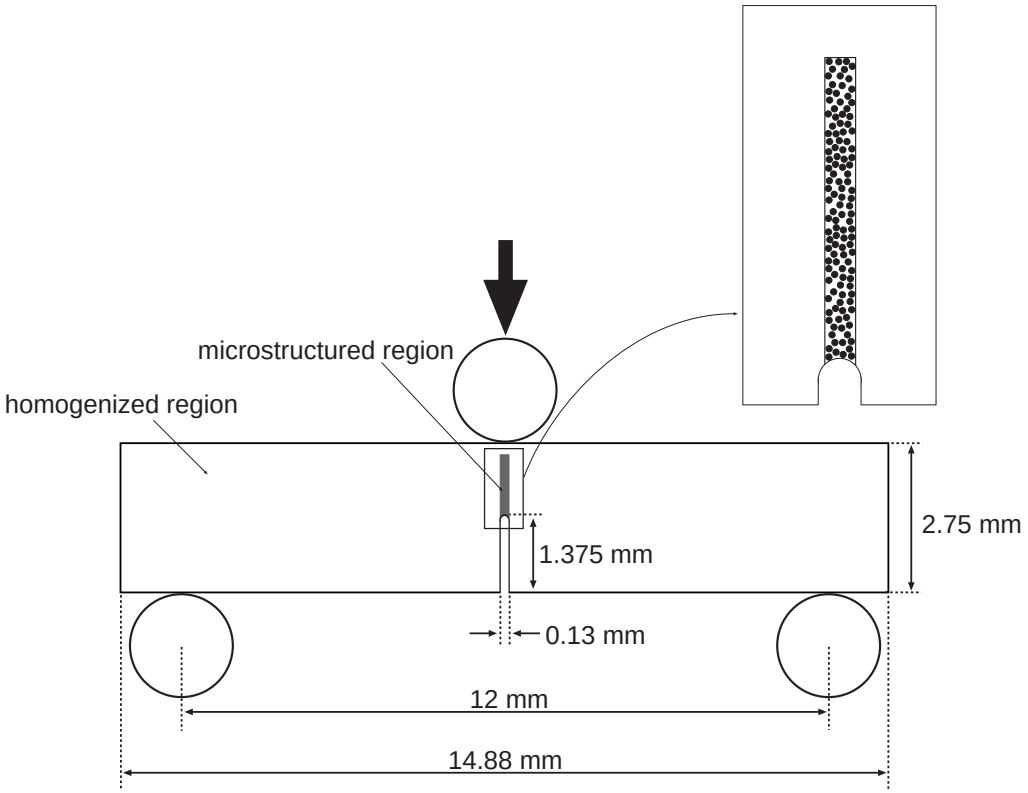

Figure 4.13: Schematic of the three-point bending embedded cell model used in the numerical simulations.

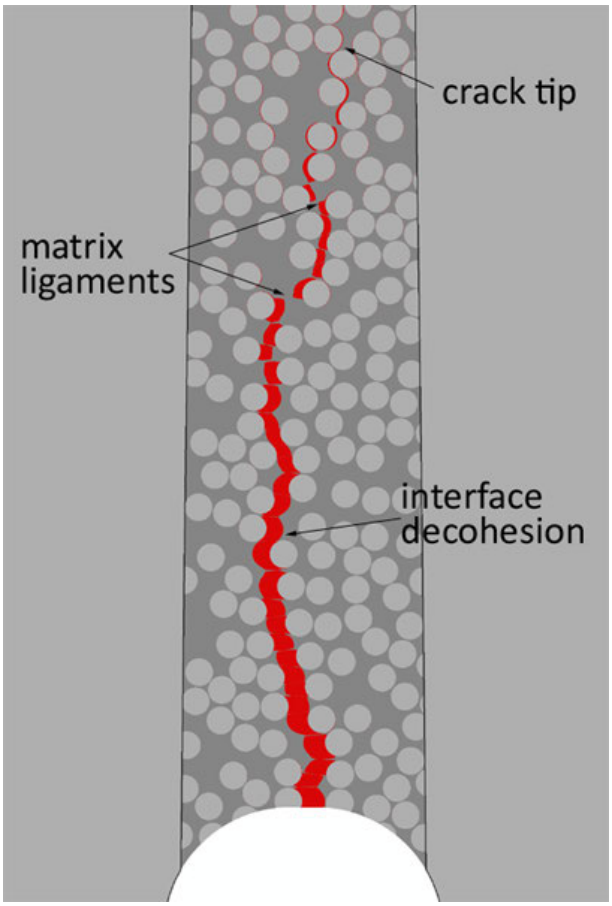

Figure 4.14: Detail of the micromechanism of damage obtained in the simulations of the three-point bending tests in notched specimens.

100 and 200 J/m^2) were employed to assess the influence of the microconstituents toughness in the overall fracture behavior of the composite.

The fracture mechanisms simulated in the numerical model showed that they were not modified by the fracture energy of the constituents. In agreement with the experimental observations of the fracture evolution in the three-point bending test, a lone crack appeared at the notch root. This crack evolved by the initial opening of the fiber-matrix interfaces and the subsequent fracture of the matrix ligaments between debonded fibers (Fig. 4.14). Thus, the numerical simulations confirmed that the fracture mechanisms are only dependent on the strength of its components, but

not on their fracture energy. However, the toughness of the microconstituents had a relevant influence on the overall fracture energy of the composite. Fig. 4.15 shows the load-CMOD curves obtained from the simulation of the three-point bending test for the studied values of the fracture energy of the matrix and the fiber-matrix interfaces. These results show that the combination of the fracture energy of the interface and the matrix controlled the peak of load and the total fracture energy dissipated by the composite. The fracture energy of the interface played the most important role, as far as the crack is initially nucleated at the fiber-matrix boundary. Once the interfaces have been broken, the crack advance was stopped by the matrix ligaments between the debonded fibers outdistanced by the crack tip. At this point, the load can increase or keep almost constant, depending on the matrix fracture energy. Finally, a real crack grew a given distance through the composite when the matrix ligaments failed, resulting in a sudden drop in the load. The repetition of this process during the crack propagation through the composite section produced a stepped shape of the unloading branch of the load-CMOD curve, which could be also observed in the experimental curves. It is important to note that since the microstructured region did not fill the whole section of the beam, the fracture process could not totally break the specimen in two halves. For this reason, simulations were stopped before the complete crack propagation across the embedded cell.

Finally, the results of the parametric study to assess the influence of the fracture energies of the microconstituents were also employed to select values for these parameters which could approximately reproduce the load-CMOD curves and the overall composite behavior experimentally obtained. Thus, an additional simulation of the three-point bending test was performed using fracture energies $G_f^{\text{interface}} = 150\text{J/m}^2$ and $G_f^{\text{matrix}} = 100\text{J/m}^2$ for the interfaces and the matrix, respectively. The load-CMOD curve obtained in this simulation is plotted in Fig. 4.16 together with the envelope of the experimental data. The overall agreement between the numerical and experimental results was very good and the predictions of the initial stiffness and the maximum load were close to the experimental values. It should be noted that the simulations underestimated the peak of the maximum load by $\approx 5\%$, although this difference can be considered negligible in the overall fracture energy and attributed to

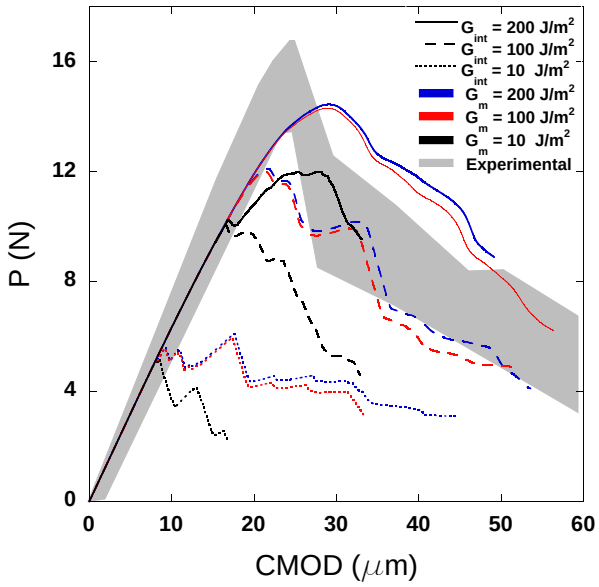

Figure 4.15: Load-CMOD curves obtained in the simulations of the three-point bending fracture tests for different values of the fracture energy of the interfaces and matrix.

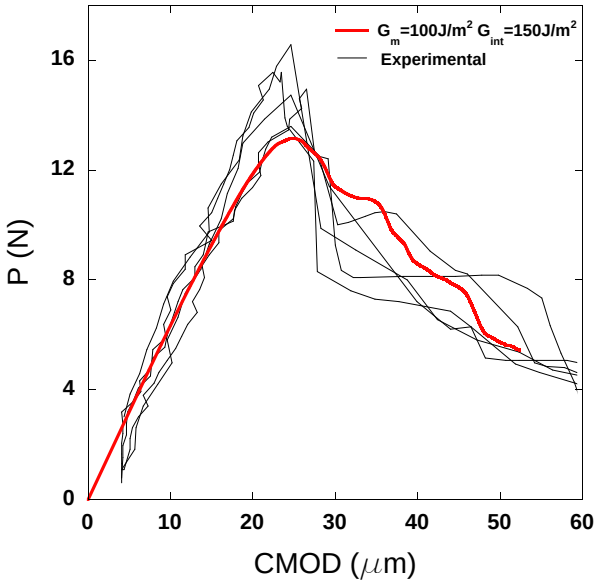

Figure 4.16: Load-CMOD curve obtained from the simulation of the three-point bending fracture tests with $G_f^{\text{interface}} = 150\text{J/m}^2$ and $G_f^{\text{matrix}} = 100\text{J/m}^2$.

many factors as small inaccuracies in the selection of the strength and the toughness of the microconstituents or to the simplifications in the geometry of the numerical model. Moreover, the most important information extracted from the three-point bending test is the fracture energy of the material, which is related with the area under the load-CMOD curve, and here the result of the simulation showed a perfect match with the experiments. Beyond the maximum load the behavior predicted by the simulation was equivalent to those reported experimentally. Once the crack was nucleated at the notch root, it stably propagated across the specimen in successive stages, which provided a stepped profile in the load-CMOD curve, in accordance to the experimental evidences. The numerically obtained load-CMOD curve falls inside the envelope of the experimental results.

The sequence of the fracture obtained through the numerical simulations of the three-point bending test is shown together with the *in situ* SEM micrographs of the crack evolution in Fig. 4.17. The simulation showed that the first indication of

damage appeared from a very early stage at the interfaces of the fibers close to the top of the notch (Fig. 4.17a), without any detectable effect in the load-CMOD curve. This nucleation of damage by the interface decohesion of the first fiber could not be observed in the SEM inspections because the acquired micrographs have not enough resolution. Thus, experimental evidence of crack nucleattion and propagation could only be observed when the applied displacement reached $\approx 40\mu$m. For this stage of load, the simulations showed a crack with approximately the same length (Fig. 4.17c). From this point on, the simulations showed that the crack is propagated across the specimen at approximately the same rate as was experimentally observed (Fig. 4.17d and e).

4.4 Concluding Remarks

The fracture behavior in the transverse direction of E-glass/MTM 57 unidirectional laminate was both experimentally and numerically studied.

Tensile tests provided the strength of the laminate in the direction perpendicular to the fibers. The toughness of the material was obtained through three-point bending test of notched specimens.

The fracture micromechanisms developed in this material were experimentally studied by carrying out additional three-point bending tests inside the scanning electron microscope, in which fracture occurred by a single crack propagated from the notch tip. The microscopic observation of the crack evolution showed that fiber-matrix decohesion followed by the fracture of the matrix ligaments between debonded fibers were the two active failure mechanisms.

Tensile and three-point bending tests were simulated through multiscale models based on the embedded cell approach. The specimens representation included two regions: one was endowed with full details of the composite microstructure (including the matrix, fibers and interfaces) and another surrounding this region, where the composite was represented by a linear, elastic and homogeneous solid. The experimentally observed damage micromechanisms were included in the simulations through the adequate constitutive models. The mechanical response of the composite was

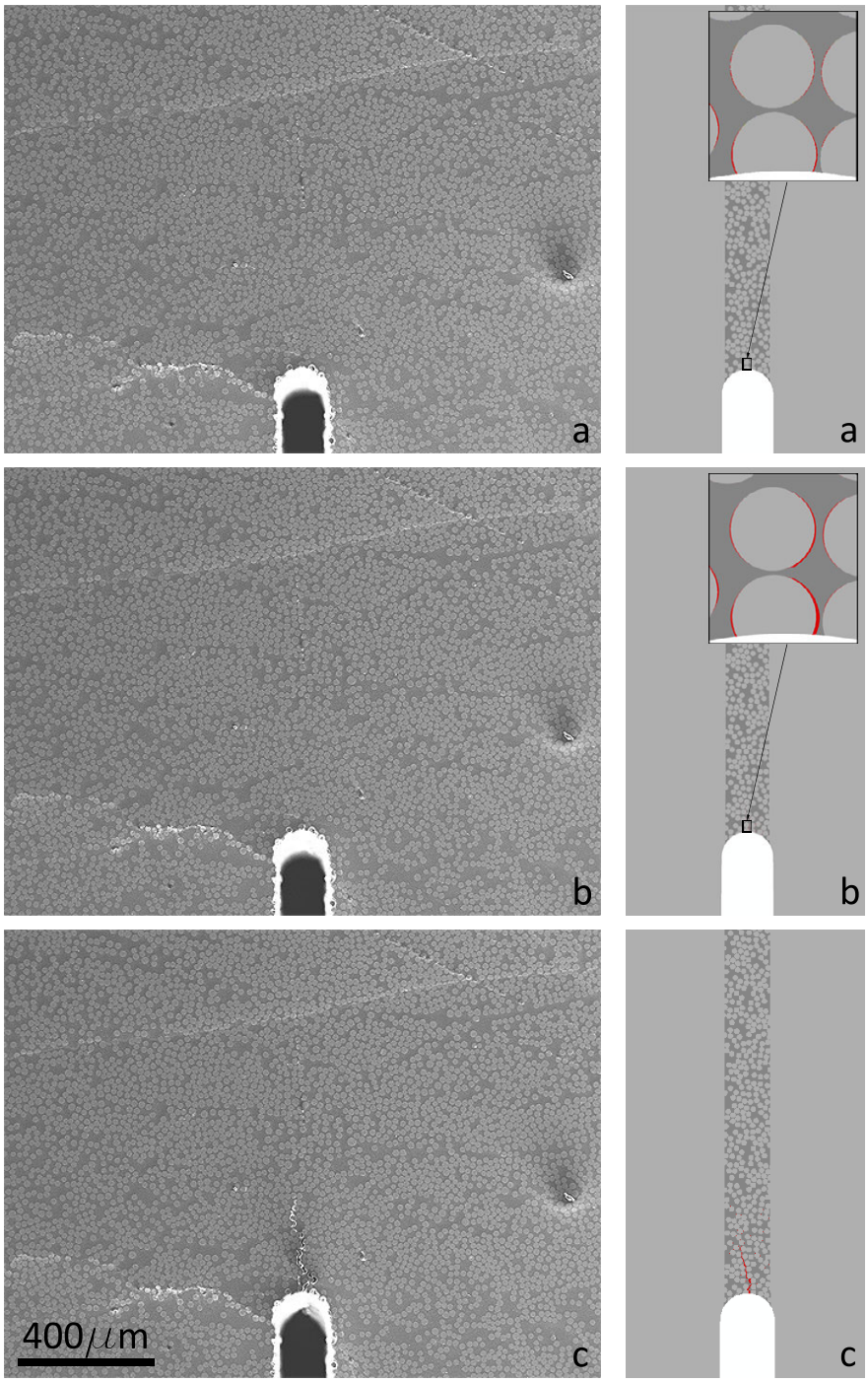
a
a
b
b
400μm
c
c

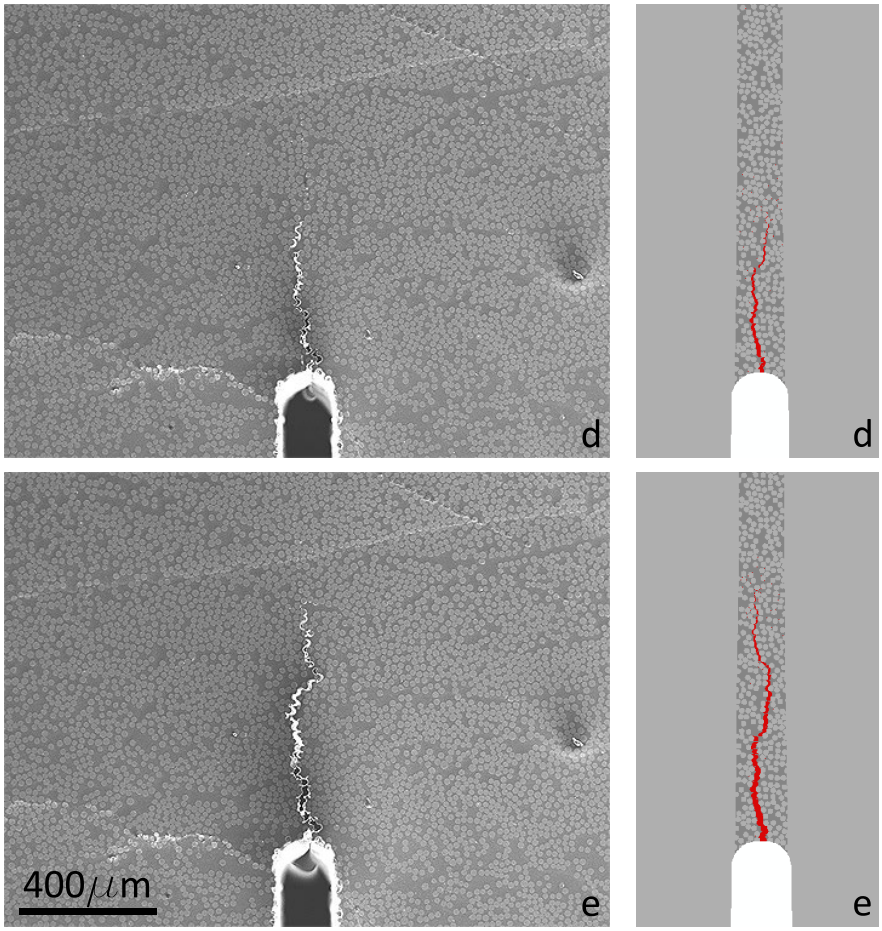

Figure 4.17: Scanning electron micrographs and simulations showing the sequence of the crack propagation during the three-point bending test. The displacement of the load application point corresponds to (a) 20μm (with detail of the fiber-matrix decohesion), (b) 30μm (with detail of the fiber-matrix decohesion), (c) 40μm, (d) 50μm and (e) 60μm.

computed through the finite element method, and it was found that the multiscale computational model reproduced the main deformation and damage mechanisms.

Finally, the simulations of the three-point bending test were also employed to estimate the value of the fracture energies of the matrix and the fiber-matrix interfaces, whose experimental determination is extremely difficult to achieve.

Chapter 5

In situ SEM compression test

Mechanical properties of FRPs are dictated by phenomena which take place at the micron scale, which is the size of the reinforcement. This is the case, for instance, of deformation (matrix-reinforcement load transfer) and fracture mechanisms (fiber-matrix decohesion). Our knowledge of the role played by the microstructure in the mechanical performance of materials has benefited greatly from the information provided by different kinds of microscopy (optical, scanning and transmission electron, atomic force) and particularly from the ability to carry out *in situ* mechanical tests inside the microscope. This latter technique allows for recording of the sequence of the deformation and fracture events, leading to a clear and qualitative understanding of the interaction among the relevant microstructural features on the performance.

More precise quantitative information about the deformation and fracture processes at the micron scale can be obtained through the application of optical full-field measurement methods, e.g. digital image correlation (DIC) in combination with *in situ* testing inside a scanning electron microsocope (SEM).

In this chapter, the most important deformation and damage mechanisms developed in the transverse section of FRPs are studied by means of in situ SEM testing of specimens of E glass/MTM 57 laminate. To this end, compression tests were carried out inside the SEM. This technique allowed the observation of the microstructure evolution, and it influence in the deformation and fracture of the composite. In addition,

the secondary electron images obtained during the compression test were processed with DIC to extract the displacements and strain fields at the microstructural level.

5.1 Experimental techniques

Prismatic specimens of 3.2 (length) x 2.8 (width) x 2.0 (thickness) mm^3 (Fig. 5.1) were machined from the unidirectional panels using a diamond wire cutting machine. This method ensures an almost perfect parallelism between the faces of the prismatic specimens, a critical condition to obtain an homogeneous stress distribution in the compression test. The specimens were subjected to uniaxial compression perpendicular to the fibers in the laminate within a scanning electron microscope (Zeiss EVO MA-15). The compression axis was parallel to the longest dimension of the specimen and load was applied using two parallel steel compression plates mounted on a micro-electro-mechanical testing machine (Kammrath-Weiss Tensile/Compression Stage). The specimen-plate friction was minimized by coating the upper and lower specimen surfaces with vacuum wax. Compression tests were carried out at a cross-head speed of 1μm/min. The load and cross-head displacement were continuously recorded during the test using the load cell and displacement transducer of the mechanical testing machine. Secondary electron micrographs with 768 x 1024-pixel resolution were taken of the central area of the specimen at different magnifications in the range 70x to 6000x in the undeformed configuration as a reference. The central area of the specimen is the region around the center of the sample, where the solid rigid displacements are supposed to be minimum. Once the test began, it was interrupted periodically and held at a fixed displacement until full stress relaxation of the specimen was attained. The relaxation produced small reduction of the applied load, always below 5%, and took place in a few minutes. Secondary electron micrographs were then taken of the central area of the specimen with the same resolution and magnification. They were used as input for full-field measurements using the Vic2D digital image correlation software (Vic, Correlated Solutions, Inc.).

The surface preparation of the specimens was crucial to obtain good results using DIC. The microstructure of the material was first revealed by polishing a section

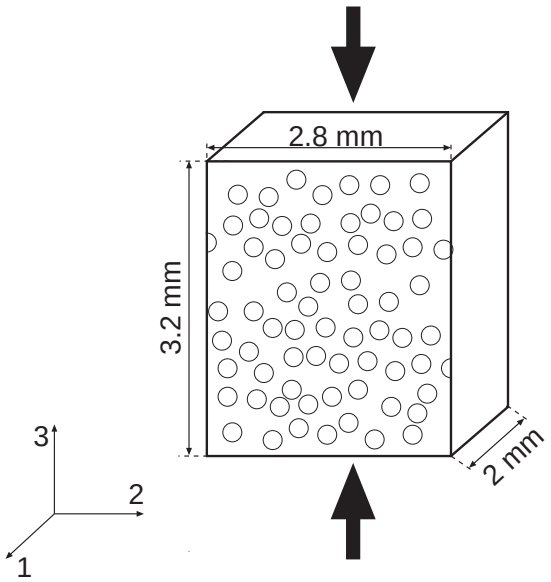

Figure 5.1: Schematic of the compressive specimen. Fibers have been enlarged to show their orientation within the specimen.

perpendicular to the fibers using SiC paper to a 1000 grit finish followed by a diamond slurry up to 1 μm grain size. A speckle pattern was created on this surface by depositing submicron alumina particles from a suspension containing 1% wt. of Al_2O_3 in propanol. The submicron powders tended to agglomerate leading to particle clusters whose size was similar to the fiber diameter but this effect was eliminated by adding iodine to the suspension as a dispersant. A typical pattern is found in the scanning electron micrograph of Fig. 5.2, showing an homogeneous dispersion of submicron alumina particles on the specimen surface. The maximum greyscale level in the image was generated by the alumina particles, and the average intensity was 130 (within the range 0-255). Meanwhile, the background microstructure showed an average intensity of 63 with a minimum greyscale level of 36. Thus, the contrast provided by this speckle pattern was good enough to correlate the displacement fields.

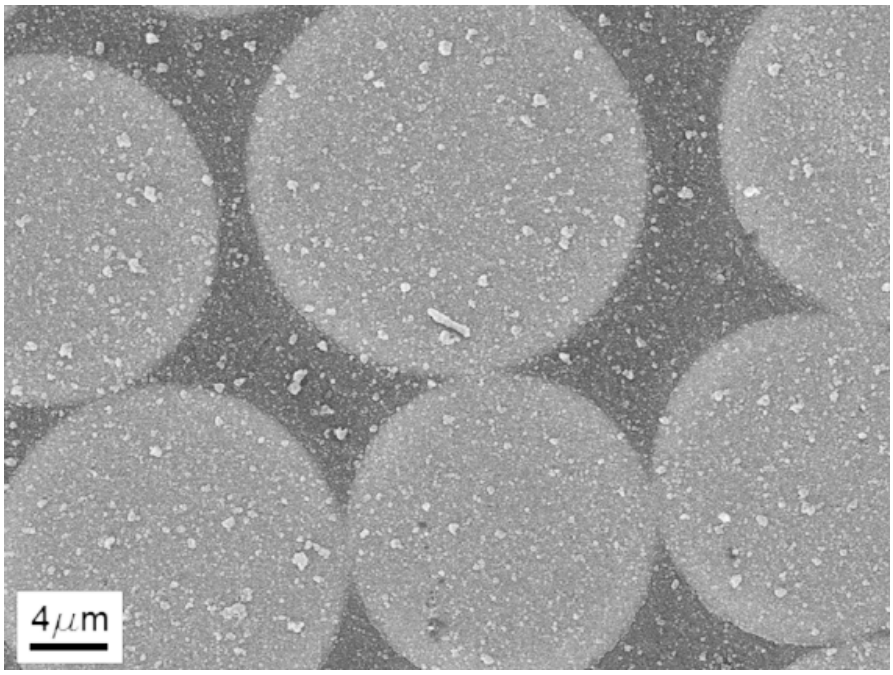

Figure 5.2: Scanning electron micrograph of the specimen surface showing the homogeneous dispersion of submicron alumina particles.

5.2 DIC in heterogeneous materials

DIC is nowadays a mature technique, widely used in the field of experimental mechanics to obtain the full displacement field (sometimes including the out-of-plane displacements) from optical images taken at different stages of deformation (Bornert et al., 2009). Its popularity among the optical methods comes from the availability of commercial packages, the low cost of high-resolution digital cameras and the general simplicity of sample preparation and optical setup. Accordingly, DIC has been applied in recent years to revealing the deformation and fracture mechanisms of Ti alloys (Lagattu et al., 2006), dual-phase steels (Kang et al., 2007; Ghadbeigi et al., 2010), and Al foams (Amsterdam et al., 2006) by analyzing secondary electron images obtained during *in situ* testing. Displacement correlation in DIC is based on the presence of a random speckle pattern on the specimen surface whose movement is tracked and compared with the initial, reference pattern. In the case of visible light, this pattern is provided by the surface texture of the material or can easily be created

by paint spraying. In the case of secondary electron images, the pattern was created by the deposition of particles 100 nm in size all over the specimen surface (Lagattu et al., 2006) or by scratching lines (Kang et al., 2007) or it was naturally produced by the differences in contrast of the microstructural features (Amsterdam et al., 2006; Ghadbeigi et al., 2010). Obviously, the accuracy and resolution of the measurements are very dependent on the nature of the reference pattern. For practical reasons, a random deposition of nanometric particles seems to be a suitable option because it would be independent of the material and fine enough to measure local displacements at the scale of the microstructural features. The foundation of the DIC technique is very simple: the displacement field is computed by tracking the distribution of gray intensity on the specimen surface in images acquired at different stages upon loading (Peters and Ranson, 1982).

The position of an arbitrary pixel i of the image in the undeformed specimen can be expressed in terms of its coordinates $\mathbf{X}_i$ in the reference configuration. This pixel will be displaced to a new position given by the coordinates $\mathbf{x}_i$ in the deformed configuration. Obviously, both coordinates are related by

$$\mathbf{x}_i = \mathbf{X}_i + \mathbf{U}_i \tag{5.1}$$

where $\mathbf{U}_i$ is the displacement vector. Let $G(\mathbf{X}_i)$ and $g(\mathbf{x}_i)$ be the intensity of the gray level in each pixel of the images corresponding to the undeformed and deformed configurations, respectively. If it is assumed that the intensity pattern deforms but it does not change its local value during deformation (i.e., $g(\mathbf{x}_i)$=$G(\mathbf{X}_i + \mathbf{U}_i)$, it is possible to track the displacement of every point of the specimen surface by identifying the displacement field which minimizes a residual function C (T. C. Chu and Peters, 1985) over the whole region of interest, where C is expressed as

$$C(\mathbf{X}_i, \mathbf{x}_i) = 1 - \frac{\sum G(\mathbf{X}_i) g(\mathbf{x}_i)}{\sqrt{\sum G(\mathbf{X}_i)^2 \sum g(\mathbf{x}_i)^2}} \tag{5.2}$$

This minimization problem is, however, too complex to be solved in a general case and it has to be simplified by introducing two main approximations. Firstly, the displacement of an arbitrary point is obtained from the evaluation of the gray intensity in its neighborhood. This set of pixels around the central one is called the

subset. Secondly, the deformations are constant within this subset. Under these assumptions, the coordinates $\mathbf{X}_i$ and $\mathbf{x}_i$ of a point of the subset in the reference and deformed configurations can be related with the coordinates of the central point of the subset ($\mathbf{X}_c$ and $\mathbf{x}_c$) by

$$\mathbf{x}_i = \mathbf{X}_c + \mathbf{U}_c + \nabla(\mathbf{U})(\mathbf{X}_i - \mathbf{X}_c) \tag{5.3}$$

where $\nabla(\mathbf{U})$ stands for the constant displacement gradient within the subset. Therefore, the subset is limited to capture homogeneous deformations. Both $\mathbf{U}_c$ and $\nabla(\mathbf{U})$ are obtained from the iterative minimization of the correlation function C (equation 5.2) within the subset. Once the displacement of the central pixel has been obtained, the subset is shifted along x- and y-directions to calculate the next point. The shift of the subset is determined by the step size, which defines how many pixels the subset was moved. Finally, the strains are computed according to the Lagrangian approach by taking the numerical derivative of the displacement field with a spacing defined by the strain window (Smits and Hemelrijck, 2005). A detailed overview of displacement and deformation measurements through digital image correlation, and its application to practical cases can be found in (Sutton et al., 2009).

The application of DIC to microscopic images obtained in electron or atomic force microscopes does not present any particular difficulty insofar as the image contains a suitable speckle pattern (Doumalin and Bornert, 2000; Yongqi et al., 1996; Vendroux and Knauss, 1998; Lagattu et al., 2006; Amsterdam et al., 2006; Ghadbeigi et al., 2010). However, DIC is a fuzzy measuring technique since it averages the displacement over the subset window (Wang and Cuitiño, 2002) and the strains are computed as the derivative of the displacements on another window. This is not a problem for capturing non-uniform full-field deformations in homogeneous materials, but limits the accuracy of the technique in the case of heterogeneous materials with strong contrast in the elastic properties of the phases if the resolution of the full-field measurements is of the order of the heterogeneity size. This limitation is due to the presence of strong deformation gradients at the interface between phases, whose evaluation may be compromised by the necessity of averaging displacements and deformations over a certain window. Thus, although DIC is a well-established tech-

Table 5.1: Elastic properties of MTM57 epoxy matrix and E-glass fibers

	E (GPa)	ν
E-glass fibers	74	0.20
MTM57 epoxy matrix	3.35	0.35

nique for obtaining the strain fields at the macroscopic scale in composites (Anzelotti et al., 2008; Totry et al., 2009, 2010) and fabrics (Lomov et al., 2008a,b; Ridruejo et al., 2011), this approach has never been used at the scale of the fibers due to the differences in stiffness between matrix and fibers.

The rigorous extension of DIC to non-homogeneous materials is not straightforward. Recent attempts were focused on the application of an interpolation technique based on the X-FEM method to account for the discontinuities in the strain field caused by microcracks (Réthoré et al., 2008). The methodology is not fully established, however, and neither is it able to deal with discontinuities due to phases with different elastic properties. So, we have preferred to assess the potential of standard DIC techniques and algorithms to capture the displacement and strain fields at the micron level in a standard fiber-reinforced composite material. In order to optimize the DIC parameters and to assess the limitations, a benchmark problem has been studied in which the exact elastic response can be computed. The problem deals with the uniaxial deformation of a representative volume element (RVE) of a model composite microstructure containing circular elastic inclusions embedded in a continuous matrix. Fiber and matrix elastic properties were those provided by the E glass/MTM 57 laminate supplier (Table 5.1) and the spatial distribution of the fibers in the RVE is shown in Fig. 5.3a. Uniaxial tension of the RVE was simulated applying a horizontal displacement on the right hand side while the left hand side of the RVE was fixed. The bottom and top boundaries of the RVE were stress-free. The exact solution to the problem was obtained using the finite element (FE) method with a very fine mesh, and the displacement and strain fields derived from the simulation were used as a reference to check the accuracy of DIC.

Images obtained from the FE simulations in the initial and deformed configura-

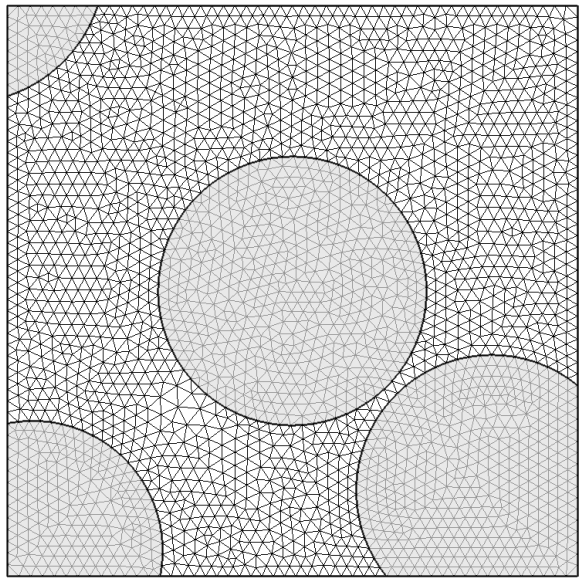

(a)

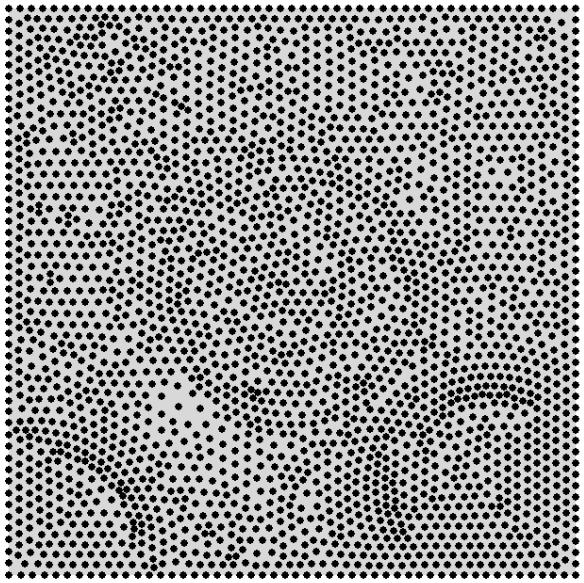

(b)

Figure 5.3: (a) RVE (with the corresponding finite element mesh superposed) used in the benchmark problem. (b) Pattern used for DIC measurements, based on nodal points.

tions were used as input for DIC. A step size of 5 pixels was maintained constant during the correlations, and the search for the optimum DIC parameters was focused in the subset and strain window size. The pattern used consisted of black dots, corresponding to each nodal point, over a grey background (Fig. 5.3b). The contrast of the computer-generated images was better than the one provided by the scanning electron micrographs. However, the size and the distribution of the black dots were comparable to the alumina particles on the specimen surface. Thus, we could use subset and strain window sizes similar to those used later for the SEM images. The contour plot of the displacements in the loading (horizontal) direction obtained from the FE analysis and from DIC with different subset sizes are plotted in Fig. 5.4. They show very good agreement, and the selection of the subset size did not significantly influence the results although transient high frequency oscillations began to be noticeable for very small subset sizes (Fig. 5.4b). Thus, these results show that the presence of heterogeneities does not impair the ability of DIC to accurately capture the displacement fields.

The contour plots for the horizontal strain field provided by the FE simulations and DIC are plotted in Fig. 5.5. The results of DIC in the figure were obtained using a subset size of $0.182D$ and strain windows of $0.0179D$ and $0.182D$, where D is the fiber diameter (0.5 the length of the RVE). At first glance, the strain fields obtained by DIC are in good agreement with the exact solution given by the FE analysis in matrix and fiber regions far away from the interface. However, the fuzzy nature of DIC makes it impossible to capture the sharp strain gradients at the fiber-matrix interface and it is necessary to optimize the parameters of DIC (namely the subset size and strain window) to enhance the accuracy of the approximation. To this end, the horizontal strains computed by FE and DIC were plotted in Fig. 5.6 along a diagonal path from the upper left to the lower right corner of the RVE. DIC results in Fig. 5.6a show the influence of the subset size at a constant value of the strain window (equal to $0.0536D$), while the curves in Fig. 5.6b present the influence of the strain window for a constant subset size of $0.182D$. The FE solution shows zones in the strain path in which the strain is very low and constant, which correspond to the stiff fibers. Matrix regions between fibers present much higher strains with very sharp gradients close to

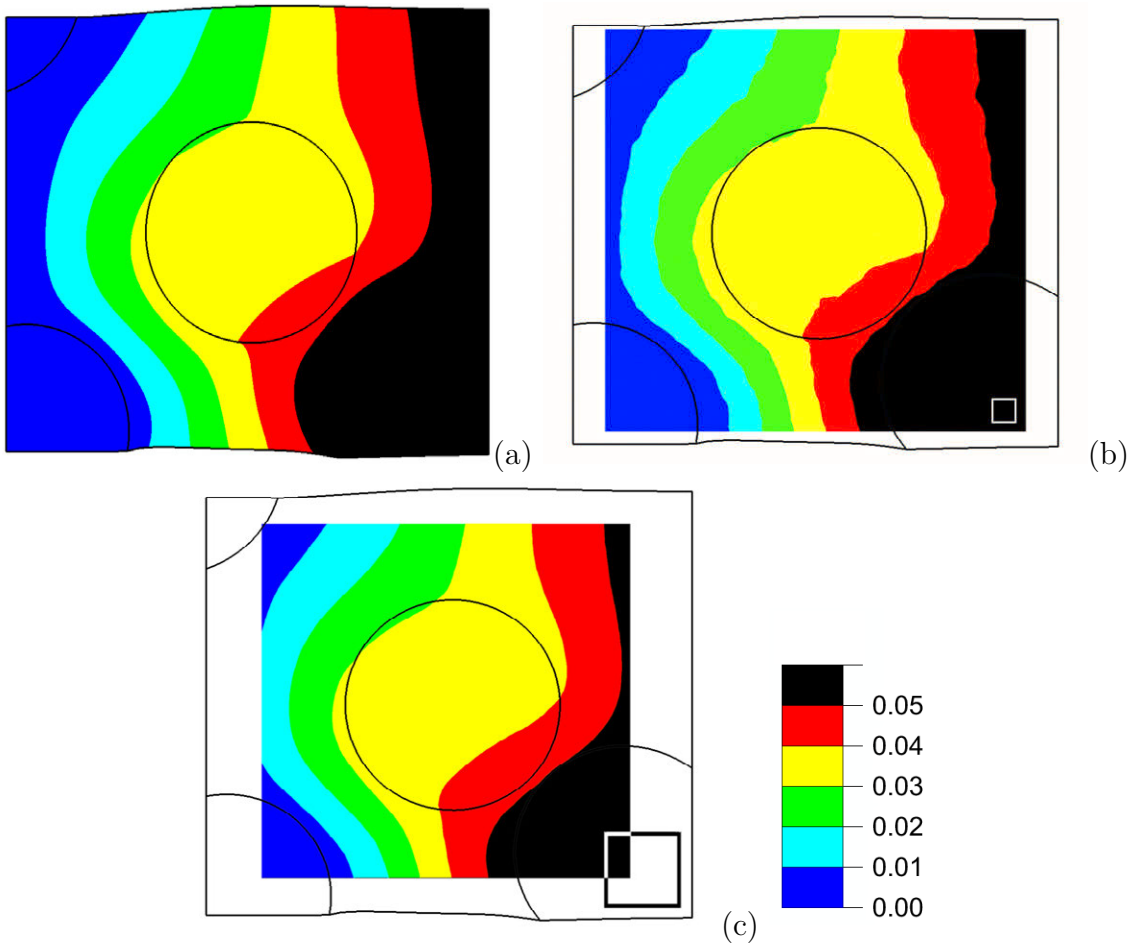

Figure 5.4: Contour plots of the horizontal displacement field in the benchmark problem (a) Reference solution provided by FE simulations. (b) DIC field with a subset size of $0.104D$ (29 pixels), the subset window is displayed in the image. (c) DIC field with a subset size of $0.361D$ (103 pixels). The displacements are normalized by the length of the unit cell.

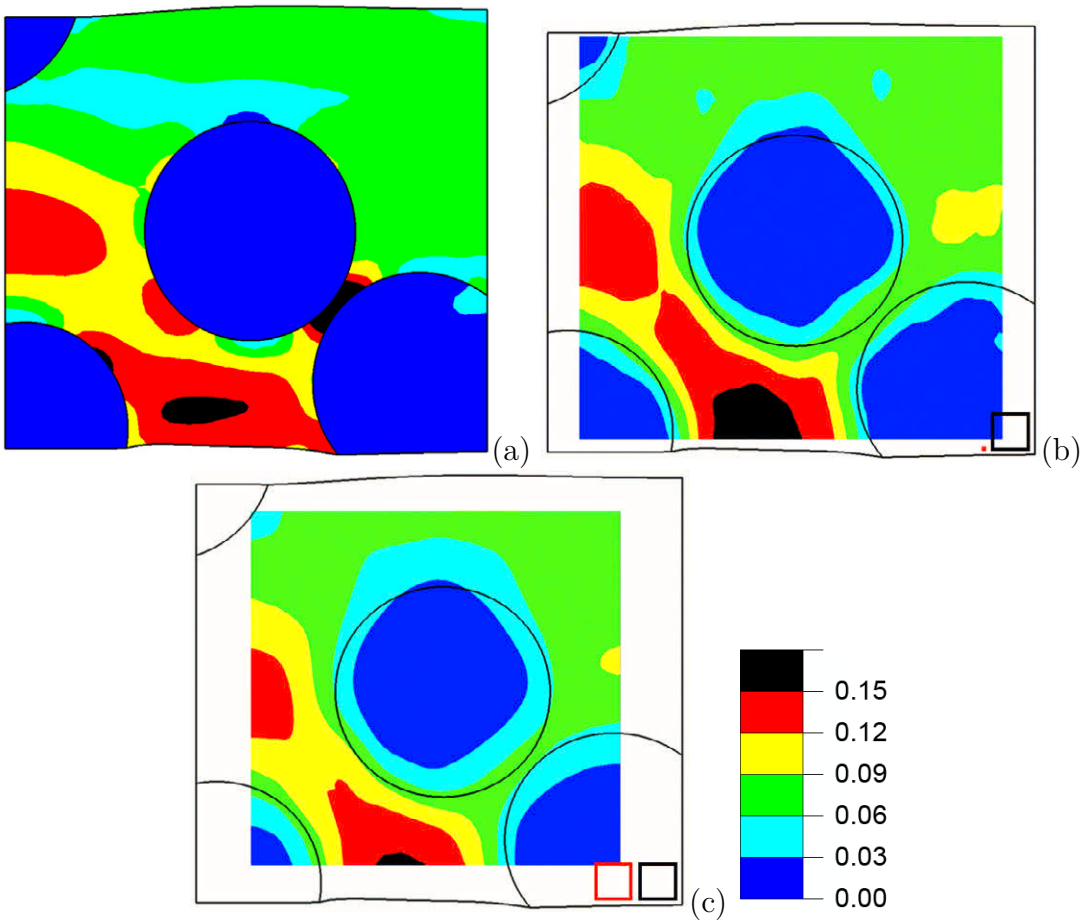

Figure 5.5: Contour plots of the horizontal strain field in the benchmark problem (a) Reference solution provided by FE simulations. (b) DIC field obtained with a subset size of $0.182D$ (51 pixels) and a strain window of $0.0179D$ (5 pixels), the subset (black) and the strain (red) windows are shown in the images. (c) DIC field obtained with a subset size of $0.182D$ and a strain window of $0.182D$.

the fiber interface. DIC was able to accurately compute the strain in the center of the fibers as well as in the matrix regions far away from the fiber interface. However, significant differences appeared near to the interface between both materials because of the discontinuity in the strain field. DIC obtains strains by taking the derivate of the displacements over a small strain window without considering the phase in which the pixels are located and the discontinuity at the interface is smoothed out.

The curves in Fig. 5.6a show that subset size did not substantially modify the strain profiles along the path and this was expected because this parameter only influences the magnitude of the displacement field, which was very accurate in the whole range of subset sizes ($0.104D$ to $0.361D$) used in this investigation. However, the strain window did modify the strain values along the path. The smaller the window, the higher the strain gradients, and thus DIC was able to capture the variations in strain near the interfaces in greater detail. Nevertheless, if the strain window was too small, high frequency oscillations appeared in the solution, leading to unrealistic oscillations of the strains within each phase. For this reason, the optimum window size should be a compromise between a small one that provides a more accurate "local" field value, and a large one that gives a smoother solution. In the case of the RVE model for composite materials, the optimum window size was around $0.05D$ which corresponds to the minimum strain window which provides logical and realistic strain fields with the minimum noise. With this window size, DIC was able to accurately reproduce the average strains in each phase and only failed to capture the strain in matrix ligaments between very close fibers.

5.3 Experimental Results

Transverse compression tests were performed using the micro-electro-mechanical testing machine inside the scanning electron microscope as indicated in the previous sections. In the first instance, the specimens were elastically strained up to $\bar{\epsilon}_2 = -1.8\%$. Second, in order to study the damage by interface decohesion, the compressive strain was continuously increased until the debonding of the fibers was spread over the specimen surface. Micrographs with 768 x 1024 pixels resolution of

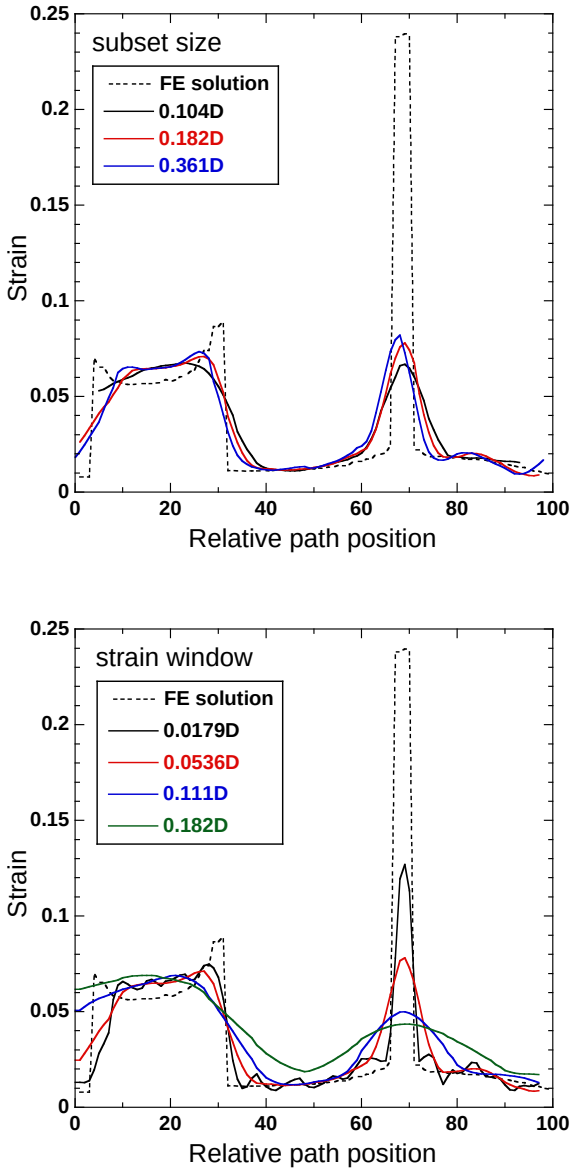

Figure 5.6: Horizontal strains along a diagonal path from the upper-left to the bottom-right corner of the RVE. (a) Influence of the subset size on DIC results. The strain window was $0.0536D$. (b) Influence of the strain window on DIC results. The subset size was $0.182D$.

a region of interest (ROI) at the center of the specimen were obtained at different magnifications and used as input for DIC analyses.

5.3.1 Elastic loading

Low magnification (250x)

The alumina nanoparticles could not be resolved on the specimen surface at this magnification and the contour of the glass fibers acted as speckle pattern for DIC. The evaluation of the displacements and strains was carried out with a subset size of 50 pixels and a strain window of 15 pixels. This subset size corresponds to approximately 50 μm ($2.5D$), while the window strain stands for $0.75D$. These large sizes for the subset and window strain limited the resolution of DIC, but it did not make sense to reduce their size because of the lack of an appropriate speckle pattern to detect the strain gradients between fibers.

The displacement field along the vertical (loading) direction obtained from a micrograph of the ROI at 250x is shown in Fig. 5.7a. Despite local fluctuations, the iso-displacement lines were almost perpendicular to the loading axis, corresponding to an homogeneous stress state characteristic of uniaxial compression. These results corroborate the adequacy of the experimental set-up to carry out uniaxial compression tests.

The contour plot of the compressive strain along the loading axis is plotted in Fig. 5.7b on top of the fiber distribution in the composite lamina. The large subset size as compared to the fiber diameter and the fact that the fiber contours acted as the speckle pattern at this magnification completely smoothed out the strain jumps associated with the fiber/matrix interface. However, the plot shows noticeable fluctuations in the strain throughout the ROI, this fluctuation corresponds to local non-homogeneities in fiber volume fraction. The local reinforcement volume fraction of three representative regions of the microstructure was computed within square windows of 100 x 100 μm^2 (Fig. 5.7b). The calculated values of the volume fraction at V1, V2 and V3 were 0.47, 0.52 and 0.63, respectively. Strain was localized in matrix-rich regions while it was minimum in zones containing clusters of highly packed fibers,

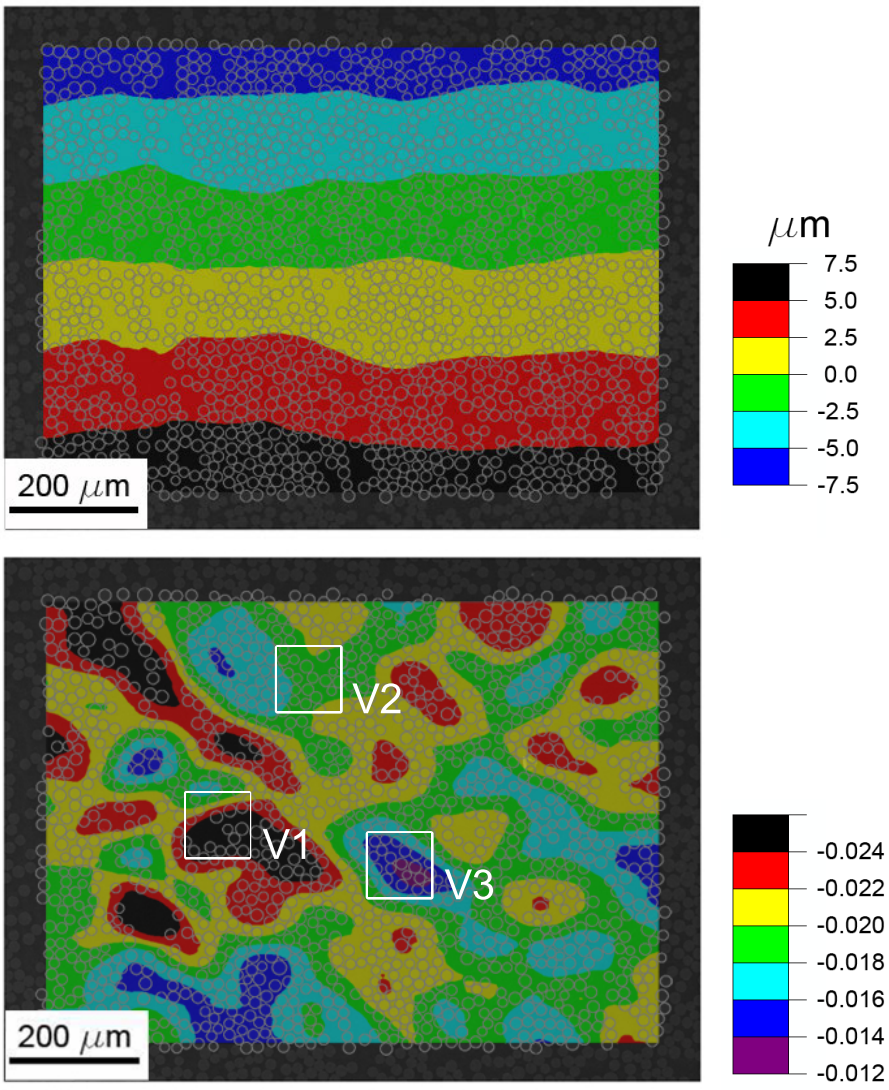

Figure 5.7: (a) Vertical displacement field obtained using DIC in a micrograph at 250x. (b) Compressive strain in the vertical (loading) direction obtained from (a). The fiber contours were artificially highlighted during post-processing of the images.

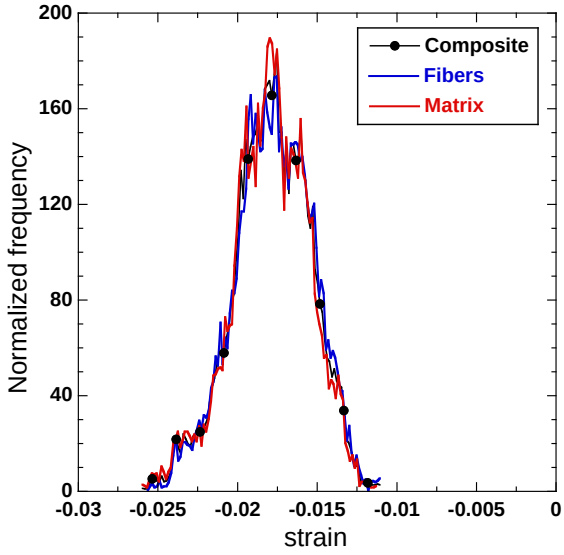

Figure 5.8: Probability density plots of the strain in the loading direction for fiber regions, matrix regions and the composite obtained from micrographs at 250x analyzed using DIC.

and only the non-homogeneities associated with fiber clusters were detected. This effect is illustrated by splitting the strain distribution into fiber and matrix areas and computing the probability density plots individually (Fig. 5.8). The different curves were not distinguishable from the overall one, indicating that the short range elastic interactions between individual fibers were not captured and were averaged over the subset size. The presence of matrix-rich and fiber-rich regions in the ROI influences in the width of the bell curve for the probability density plot which is also controlled by the contrast between elastic moduli of fibers and matrix (of the order of 22 for a typical glass/epoxy composite). The larger the contrast, the higher the difference in the elastic properties between the clustered regions and the resin-rich regions and the greater the width of the bell curve of the probability density plot. It should finally be noted that the average strain value of the composite (as obtained from the probability density plot) was $\bar{\epsilon}$ = -1.786 %.

High magnification (2000x and 6000x)

The DIC analysis of the micrographs obtained at higher magnification was carried out with a subset size of 50 pixels and a strain window of 15 pixels. The subset size of 50 pixels corresponds to approximately 6.5μm ($0.325D$) and 2.2 μm ($0.11D$) for the magnification factors of 2000 and 6000, respectively, while the strain window of 15 pixels stands for $0.0975D$ and $0.033D$. According to the analysis in section 3, these sizes were chosen to optimize the results provided by DIC at the highest magnification (6000x) while they were expected to provide reasonable results for the average strain in the composite at 2000x.

The vertical displacement fields obtained with DIC on micrographs obtained at 2000x and 6000x are plotted in Figs. 5.9a and 5.9b, respectively. Now, the heterogeneities in the displacement fields induced by the presence of matrix and fibers are resolved to the scale of the fibers at both magnifications. The corresponding vertical strain fields obtained by taking the derivative of the displacement fields are plotted in Figs. 5.10a and 5.10b for 2000x and 6000x, respectively. At first glance, it is obvious that the strain fields obtained with DIC qualitatively reproduced the expected pattern: strains in the fibers were much smaller than those found in the matrix and maximum strain concentrations were found in the matrix between fibers aligned in the (vertical) loading direction, the applied strain being mainly accommodated by the matrix ligaments between the fibers. Small longitudinal tensile strains, of absolute value very close to the resolution of DIC, appeared in fiber pairs very close to each other in the direction perpendicular to the loading axis. They were generated probably as a result of the development of large contact stresses between individual fibers upon deformation.

DIC was thus able to discriminate between fiber and matrix strains at these magnifications and this is quantitatively demonstrated in Fig. 5.11, which shows the probability density plots for the matrix and fibers regions as well as for the overall composite from the micrographs at 6000x magnification. The shape and intensity of the probability density functions for each phase were different from the corresponding plots obtained at 250x (Fig. 5.8). Fibers were characterized by a narrow peak which stands for an homogeneous strain field within the phase, while the matrix showed a

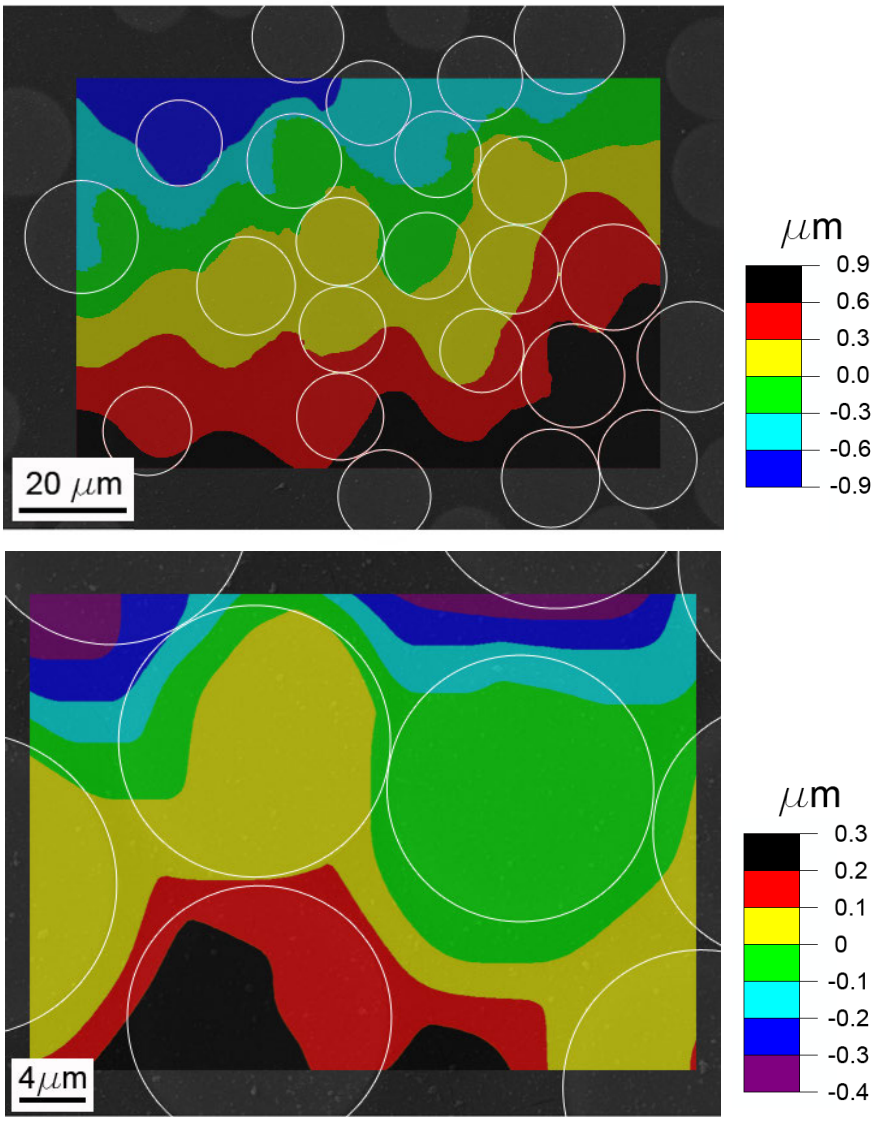

Figure 5.9: (a) Vertical displacement field obtained using DIC in a micrograph at 2000x for a compressive strain applied of $\bar{\epsilon}_2 = 1.8\%$. (b) Vertical displacement field obtained using DIC in a micrograph at 6000x for a compressive strain applied of $\bar{\epsilon}_2 = 1.8\%$. Loading axis is vertical.

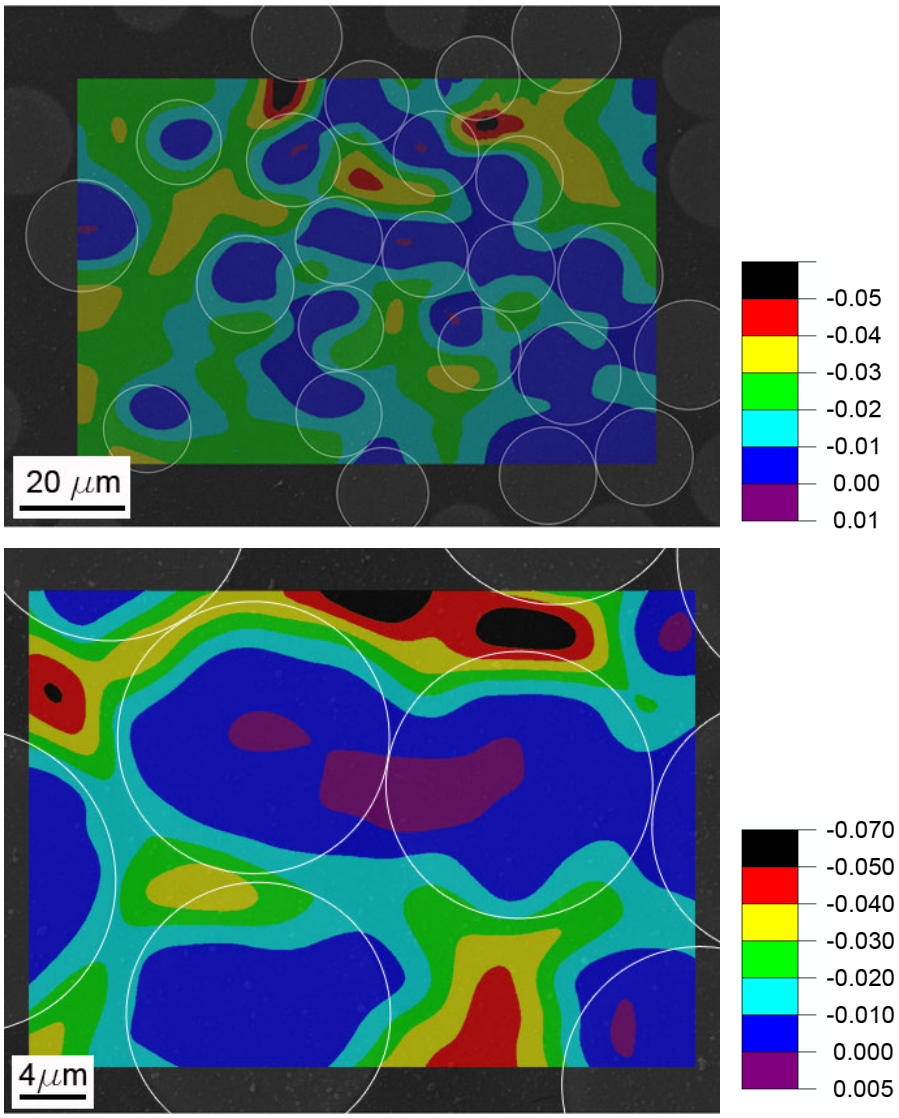

Figure 5.10: (a) Vertical strain field obtained using DIC in a micrograph at 2000x for a compressive strain applied of $\bar{\epsilon}_2 = 1.8\%$. (b)Vertical strain field obtained using DIC in a micrograph at 6000x for a compressive strain applied of $\bar{\epsilon}_2 = 1.8\%$. Loading axis is vertical.

Table 5.2: Average strains in the loading direction obtained by DIC.

	$\bar{\epsilon}$	$\bar{\epsilon}_f$	$\bar{\epsilon}_m$
DIC (2000x)	-0.0169	-0.0094	-0.0237
DIC (6000x)	-0.0148	-0.0089	-0.0237

wide distribution indicative of a very non-homogeneous strain distribution within the phase.

The average composite strain ($\bar{\epsilon}$) as well as the average strains in each phase ($\bar{\epsilon}_f$ and $\bar{\epsilon}_m$) were obtained from the probability density plots and are shown in Table 5.2. The average composite strain at 2000x was very close to that obtained at 250x while the result obtained at 6000x was slightly lower. This difference was not attributed, however, to the inaccuracy of DIC but to the actual fluctuations in the local reinforcement volume fraction when the number of fibers in the ROI is small. In fact, the reinforcement volume fraction in the ROI at 6000x was 61% while the average reinforcement volume fraction in the composite was only 54%. The average strain values in the matrix and the fibers obtained at 2000x and 6000x were similar but the accuracy of these values is questionable due to the limitations of DIC in the presence of strain discontinuities created by the mismatch in the mechanical properties.

5.3.2 Inelastic loading

The SEM inspection of the specimen during its compressive straining up to $\bar{\epsilon}_2 = -1.8\%$ did not show any evidence of damage by fiber/matrix decohesion neither matrix damage. However, the nucleation and evolution of failure mechanisms were evident for further strains. The fiber/matrix decohesion produced the cracking of the Au/Pd metallic coating which followed the deformation imposed by the composite material during the transversal compressive loading. The material discontinity caused by the crack opening at the fiber/matrix interface produces the local electrostatic charging of the specimen. This process produces a noticeable brightness around the crack mouth, which make possible the observation of the damage by decohesion from very early stages of failure.

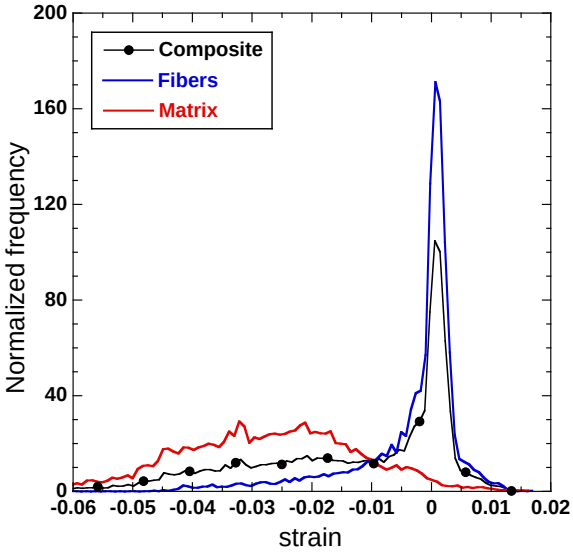

Figure 5.11: Probability density plots of the strain in the loading direction for fiber regions, matrix regions and the composite obtained from micrographs at 6000x analyzed using DIC.

The scanning electron micrographs acquired at 500X magnification levels are presented in Figs. 5.12a to 5.12f for given applied increments of transversal compressive strain up to $\bar{\epsilon}_2 = -3.5\%$. The glass fibers were not distributed homogeneously within the polymer matrix and some areas exhibited large volume fraction of reinforcement leading to noticeable fiber clustering. These clustered areas give rise to thin polymer ligaments between neighbouring fibers, where the stresses will be concentrated, leading to predominant locations for fiber/matrix decohesion. At the first strain step, Fig. 5.12b, some interface debondings were evident but clearly isolated. Further straining increasingly produced interface decohesion events up to the final failure by coalescence of debonded areas (Figs. 5.12e and 5.12f), which caused a clear softening in the global stress-strain curve of the laminate (Fig. 2.3).

The evolution of the fiber/matrix decohesion damage mechanism was more evident when analyzing the SEM images obtained at high magnification level (Fig. 5.13). The fiber clustering enhances the nucleation and subsequent growth of the interface decohesion between close fibers perpendicularly oriented to the direction

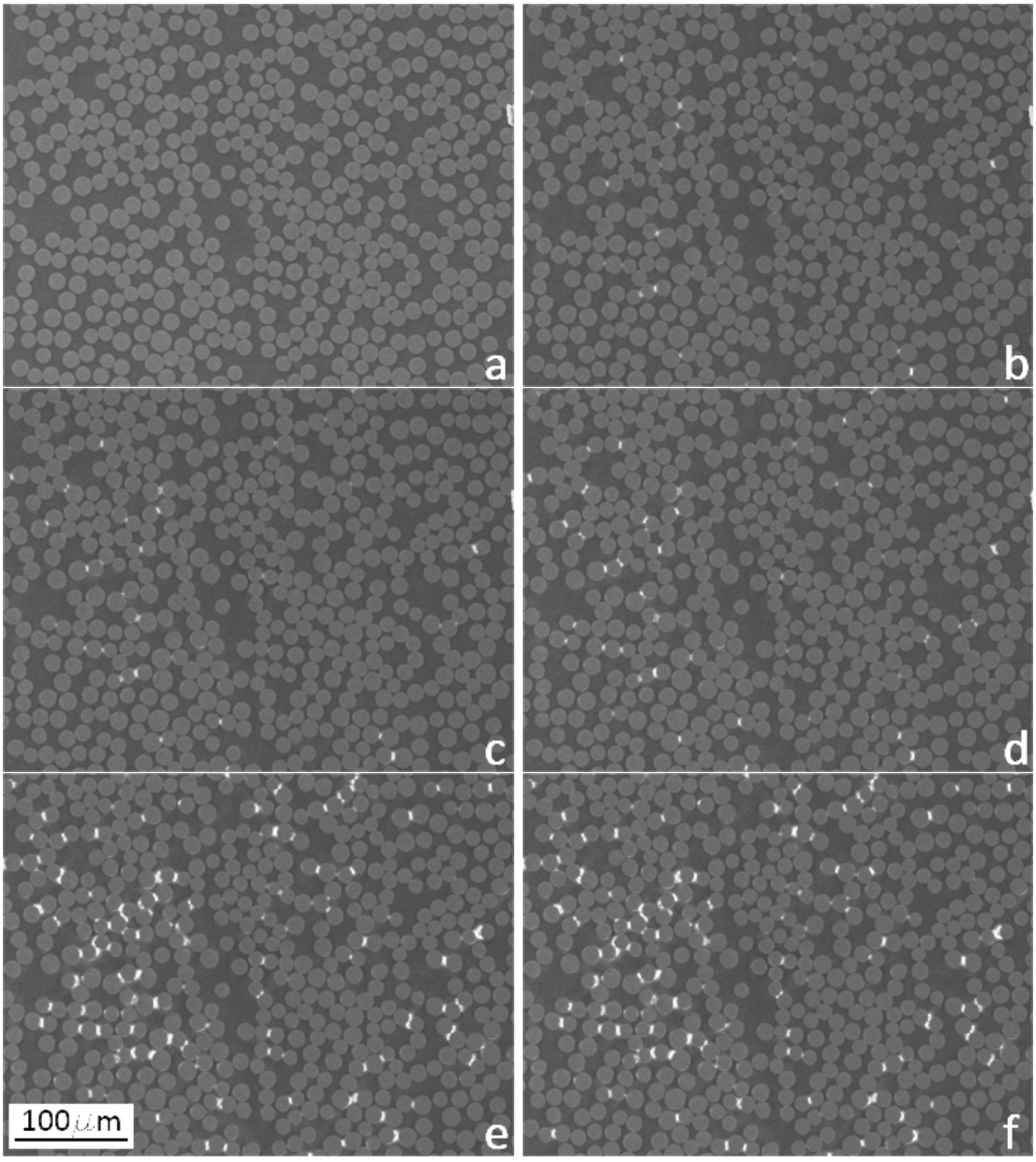

Figure 5.12: Scanning electron micrograps acquired at 500x magnification level. The average compressive strain applied corresponds to: (a) $\bar{\epsilon}_2 = 0$, (b) $\bar{\epsilon}_2 = 2.2\%$, (c)$\bar{\epsilon}_2 = 2.5\%$, (d)$\bar{\epsilon}_2 = 2.7\%$, (e)$\bar{\epsilon}_2 = 3.2\%$ and (f)$\bar{\epsilon}_2 = 3.5\%$.

of the compression. Thus, the interface crack nucleates at the interface points perpendicular to the applied load, where the tension stresses are maximum because of Poisson effect and the mismatch of elastic properties between the matrix and the reinforcement. Fig. 5.13 shows the evolution of the debonding process at the central pair of the fibers. It also makes evident that the fiber clustering leads to large stress concentrations which overcomes the interface strength, triggering the decohesion at those positions of the microstructure. After the nucleation of the interface crack, it stably growths as the compressive straining of the specimen increases. As a result, the decohesion generates voids with a crescent-moon shape (Fig. 5.13f). The final debonded angle was assumed to be controlled by the mechanical properties of the interface, particularly the interface toughness, the corresponding mode-mixity ratio and the relative position between the pair of adjacent fibers.

5.4 Numerical model

The results presented in the previous section show that the *in situ* SEM testing is able to provide a clear understanding of the deformation mechanisms developed in the composite material at the micron scale. Moreover, DIC can be applied to the scanning electron micrographs to qualitatively capture the non-homogeneous strain fields in the microstructure. However, it is also evident that the averaging nature of the DIC technique leads to errors in the strain measurement near to the fiber/matrix interface. In order to quantify the errors of the DIC measurement and study the evolution of the damage by the decohesion of the fiber/matrix interfaces, the actual deformations of the ROI at 2000x and 6000x were simulated by means of computational micromechanics. This technique has been successfully applied in the past to modeling the deformation and fracture micromechanisms of composites at the micron scale. It is based on the finite element (FE) analyses of a representative element of the material in which the microstructural details (fibers and matrix) are explicitly represented (Segurado and LLorca, 2005; González and LLorca, 2007a; Totry et al., 2008c).

In this particular case, the real microstructures analized with DIC (Figs. 5.9 and

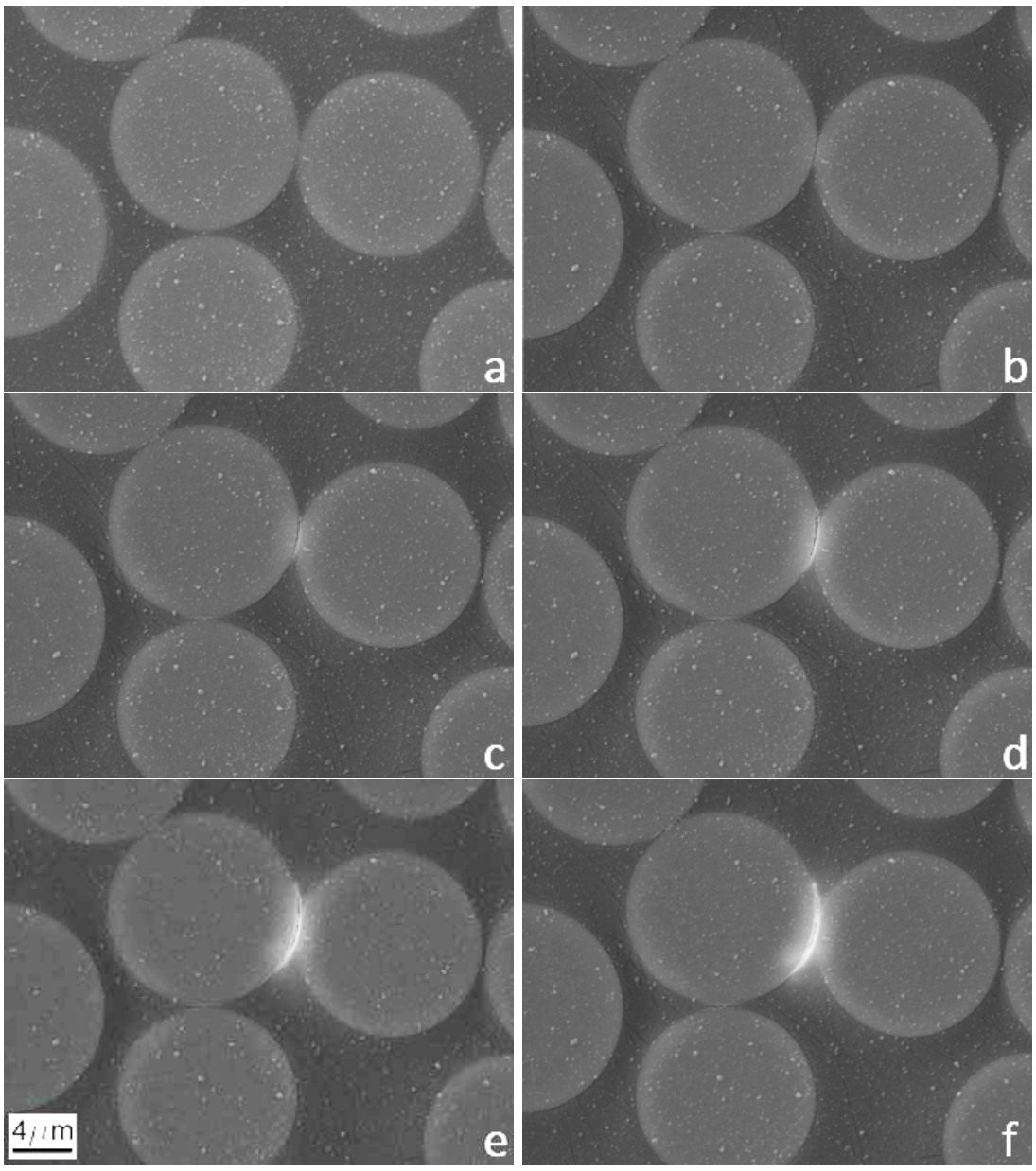

Figure 5.13: Scanning electron micrograps acquired at 6000x magnification level. The average compressive strain applied corresponds to: (a) $\bar{\epsilon}_2 = 0$, (b) $\bar{\epsilon}_2 = 2.2\%$, (c)$\bar{\epsilon}_2 = 2.5\%$, (d)$\bar{\epsilon}_2 = 2.7\%$, (e)$\bar{\epsilon}_2 = 3.2\%$ and (f)$\bar{\epsilon}_2 = 3.5\%$.

Table 5.3: Elastic properties of MTM 57 epoxy matrix and E-glass fibers

	E (GPa)	ν
E-glass fibers	74	0.20
MTM57 epoxy matrix	3.50	0.35

5.10) were exactly replicated in a two-dimensional finite element model. The matrix and fibers were automatically meshed using 6-node isoparametric modified triangles (CPE6M in Abaqus Standard) with integration at three Gauss points and hourglass control. Special care was taken to generate a very fine and homogeneous mesh at the ligaments between adjacent fibers to resolve the large deformation gradients which appear in these regions upon deformation.

Glass fibers were modeled as linear, elastic and isotropic solids. Their mechanical properties (perpendicular to the fiber axis) were provided by the material supplier or measured by nanoindentation techniques. The matrix was represented by an isotropic and elasto-viscoplastic solid, following the plasticity model for quasi-brittle materials presented in Chapter 1. Its elastic constants are shown in Table 5.3, while the parameters of the pressure sensibility and the compressive strength are $\alpha = 0.13$ and $\sigma_{co} = 105$MPa, which were estimated by means of transverse compression tests of the laminate and nanomechanical characterization of the epoxy matrix (Chapter 3). The damage by interface fracture was included in the numerical model by interface cohesive elements (COH2D4) inserted between matrix and fibers. The interface strength of the interface under shear loading was experimentally measured by push-out test (Chapter 3) which provided a value of $S = 75$Mpa. This value was also considered an estimation for the tensile strength of the matrix $\sigma_{to} = S$. The normal strength of the interface was approximated as $N = 50$MPa. The toughness values for the matrix and the interfaces were respectively $G = 100\text{J/m}^2$ and $G = 150\text{J/m}^2$, which are representative values of the fracture energy of the fiber/matrix interfaces and epoxy resins (Zhou et al., 2001).

The actual displacements in the longitudinal and vertical directions measured by DIC on the external boundary of the model were applied to the finite element model.

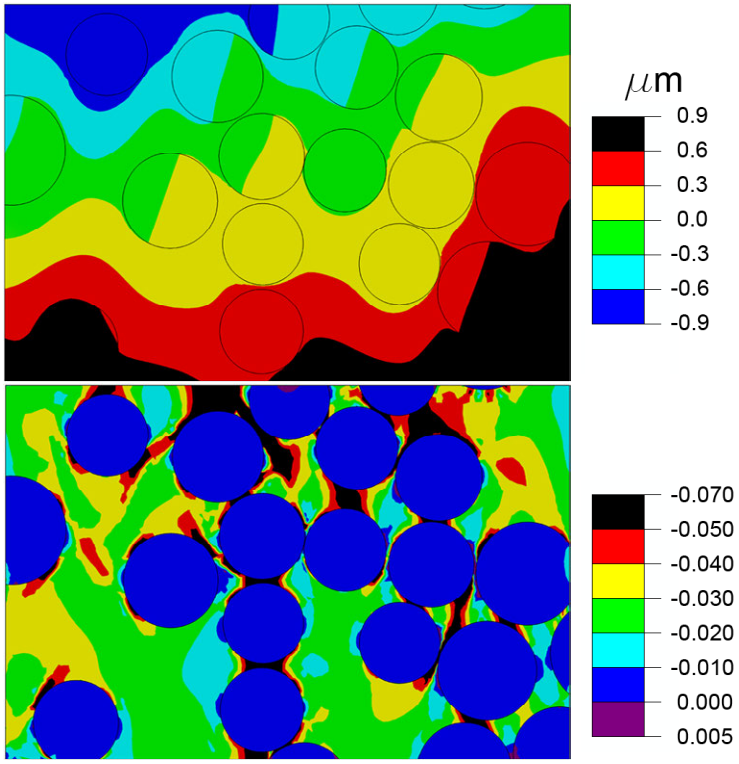

Figure 5.14: (a) Vertical displacement field obtained from the numerical simulation of a micrograph at 2000x for a compressive strain applied of $\bar{\epsilon}_2 = 1.8\%$. (b) Vertical strain field obtained from the numerical simulation of a micrograph at 2000x for a compressive strain applied of $\bar{\epsilon}_2 = 1.8\%$. Loading axis is vertical.

This ensured the displacement continuity with the composite outside of the region analyzed and introduced the deformation patterns experimentally observed into the model. The real problem is truly three dimensional and cannot be exactly simulated under plane strain or plane stress conditions. However, the exact response must be in between both cases and simulations in the two limiting conditions were carried out in Abaqus/Standard. The differences between them were negligible for the displacement and strain fields in the xy-plane.

5.4.1 Elastic deformation

The contour plots of the vertical displacement and of the vertical strain obtained from the finite element simulation of the microstructure at 2000x are shown in Figs.

5.14a and 5.14b, respectively. They can be compared with the DIC results in Figs. 5.9a and 5.10a. The displacement field provided by the numerical simulations was qualitatively equivalent to the experimental one obtained by DIC. Both strategies clearly showed that fibers acted as pinning points and that the iso-displacement lines were highly curved around the fibers. A better quantitative comparison can be obtained by plotting the magnitude of the vertical displacement field along a diagonal line from the upper left to the lower right corner (Fig. 5.15a). The general agreement between the experiments and simulations is fairly good, demonstrating the potential of DIC technique to reveal the displacement patterns at the microscopic scale.

The comparison of the numerical and experimental strain fields (Figs. 5.14b and 5.10a) follows the same trends although there were noticeable differences at the local level in the gradients near to the interfaces and regions with high strain concentrations. Generally speaking, agreement is good and the strain field trends are well captured even with the relatively large subset size used in this study (50 pixels, which corresponds to ≈ 6.5 μm at 2000x and ≈ 2.2 μm at 2000x), which are of the order of magnitude of the fiber diameter. Nevertheless, the strain fields given by DIC within the fibers presented unrealistic gradients, while the finite element simulations showed that the strain within the fibers was fairly constant. Obviously, these differences come about as a result of the smoothing of the large strain gradients at the fiber/matrix interface into the fibers due to the DIC subset size. A more detailed quantification of this effect can be found in Fig. 5.15b, in which the vertical strain is plotted along a diagonal line from the lower left to the upper right corner of the ROI. This plot shows the limitation of DIC to capture the sharp strain jumps at the fiber/matrix interface and the modification of the average strain in the fiber as a result of the smoothing of the sharp gradients. Nevertheless, it should be noted that the average fiber strain is generally well captured at the center of each fiber.

It is interesting to notice that the strain field given by the finite element simulations showed the incipient concentration of the deformation in narrow bands oriented at an angle of slightly higher than 45° with the plane perpendicular to the compression direction (y-axis).This strain concentration indicated the beginning of the yielding of the matrix in those regions of high stress, in the ligaments between ad-

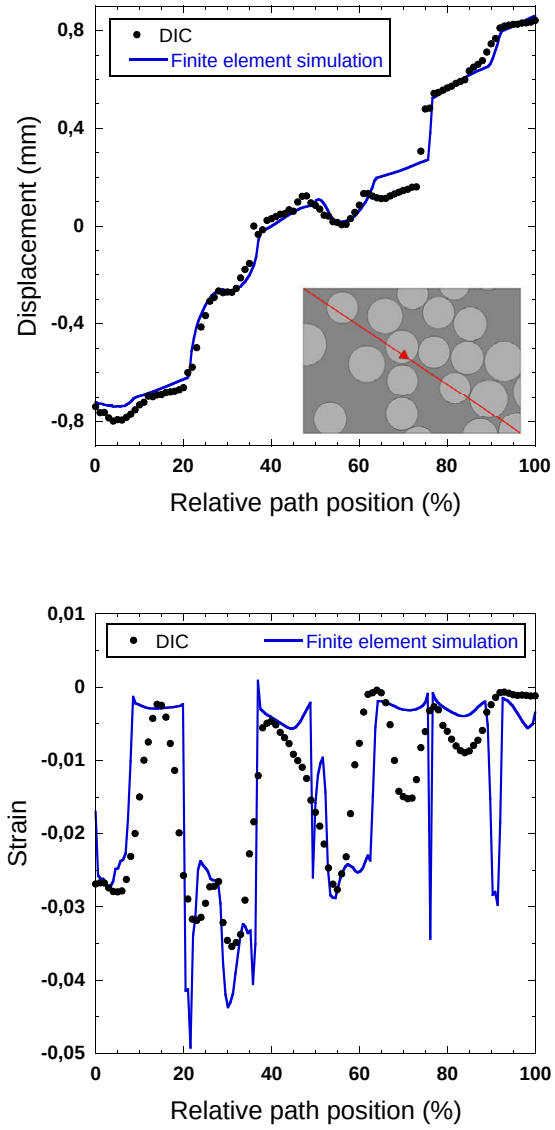

Figure 5.15: Comparison of digital image correlation measurements at 2000x and the corresponding finite element results along a diagonal path from the upper left to the bottom right corner of the ROI for a compressive strain applied of $\bar{\epsilon}_2 = 1.8\%$. (a) Vertical displacement. (b) Vertical strain.

jacent fibers. However, the initiation of the yielding is a very local process, and it couldn't be captured by the DIC analysis of the micrographs neither had any effect on the macroscopical response of the material. The evolution of the material degradation due to matrix yielding and fiber/matrix decohesion was studied by the simulation of the ROI deformation at higher compressive strains.

5.4.2 Inelastic deformation

The numerical simulations of the ROI deformations also provided important information on the development of the damage mechanisms at the microscopic level. The deformed shape of the simulated ROI and the scanning electron micrographs of the *in situ* compression test are plot in Figs. 5.16 and 5.17 for 2000x and 6000x magnification, respectively. Their overall comparison showed that the numerical patterns followed closely the experimental observations. As pointed before, damage by interface decohesion was always nucleated at the equator of the fibers, in the direction perpendicular to the compression. This nucleation points were reproduced in the simulations, which also revealed that the debonding process is initiated for very low strain levels (Fig. 5.17b). This effect, that could not be capture by the experimental setting due to resolution problems, indicates that the mismatch between the properties of the constituents and the fiber clustering lead to large stress concentrations at the interfaces, which enhance the initiation of the decohesion. Once the damage was nucleated, the crack advanced along the fiber/matrix interface, generating the experimentally observed decohesion pattern.

Furthermore, the numerical simulation of the ROI allowed to study the yielding of the epoxy matrix, whose observation in the SEM was not possible. Fig. 5.18 shows the development of the shear bands in the simulation of the transverse compression of the FRPs specimen. The yielding of the matrix started at a very low strain level, in the regions in contact with the fibers, approximately at the points equidistant from the poles and the equator (latitudes $\approx$ 45 S and 45 N), where the shear stress was maximum. Further deformations produced shear bands approximately oriented at 54° respect to the plane perpendicular to the compressive direction (the y-axis). For the final stages of the simulated compression test (Fig. 5.18c), the shear bands

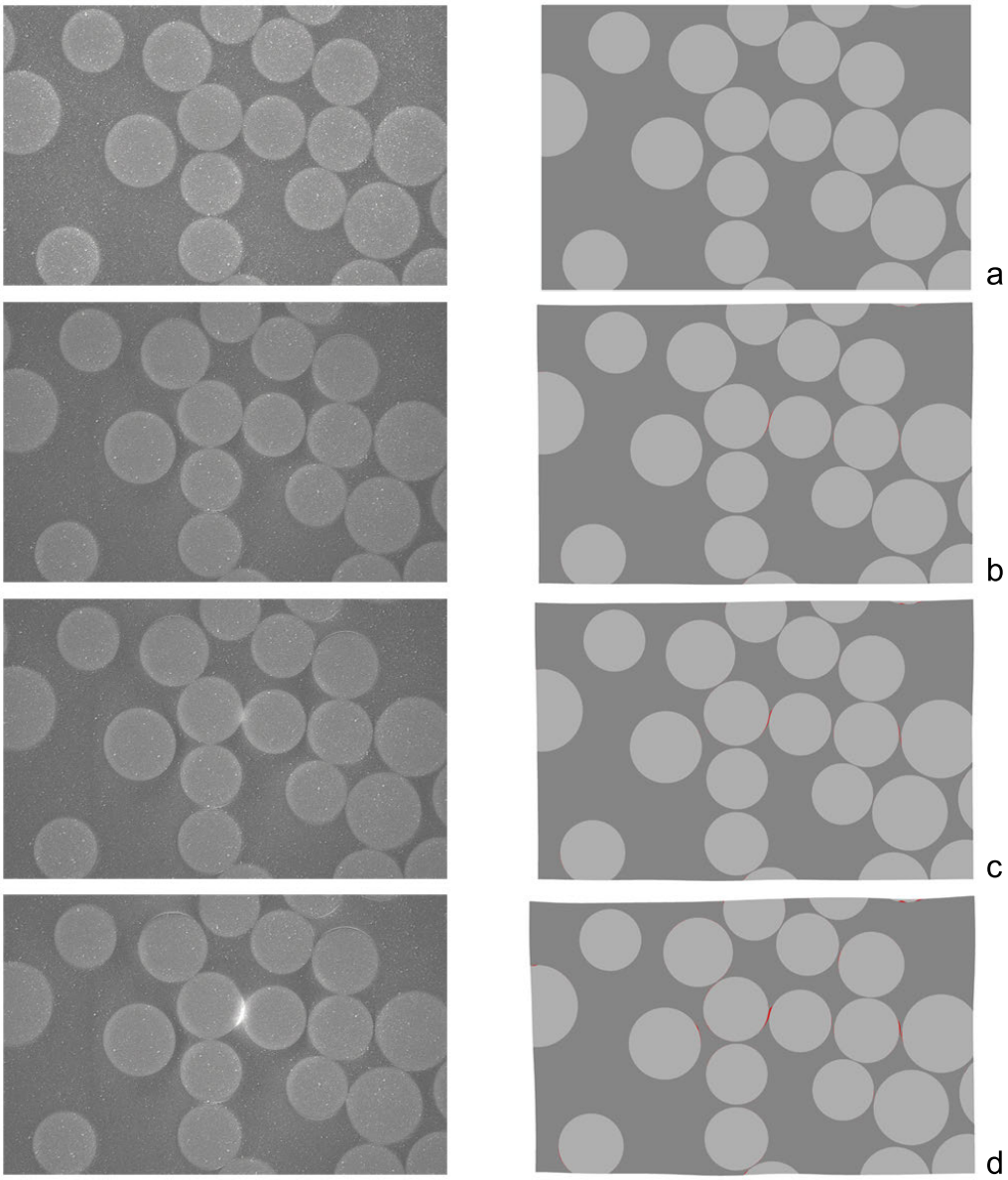

Figure 5.16: Scanning electron micrographs and deformed shape of the simulations of the ROI at 2000x showing the evolution of the interface decohesion through the compression test. Loading axis is vertical and the average applied strains correspond to: (a) $\bar{\epsilon}_2 = 0$, (b) $\bar{\epsilon}_2 = 0.018$, (c) $\bar{\epsilon}_2 = 0.026$ and (d) $\bar{\epsilon}_2 = 0.032$

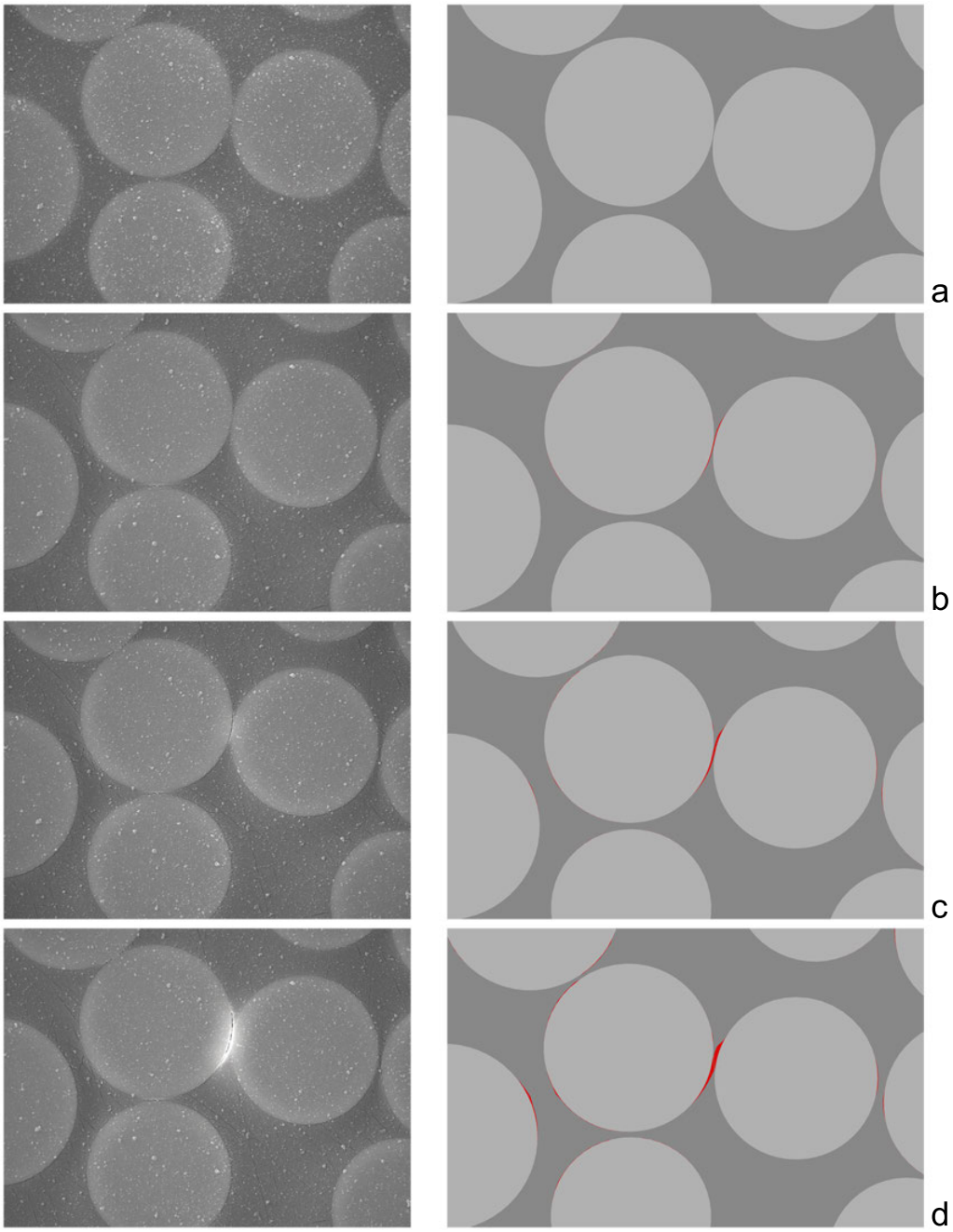

Figure 5.17: Scanning electron micrographs and deformed shape of the simulations of the ROI at 6000x showing the evolution of the interface decohesion through the compression test. Loading axis is vertical and the average applied strains correspond to: (a) $\bar{\epsilon}_2 = 0$, (b) $\bar{\epsilon}_2 = 0.018$, (c) $\bar{\epsilon}_2 = 0.026$ and (d) $\bar{\epsilon}_2 = 0.032$

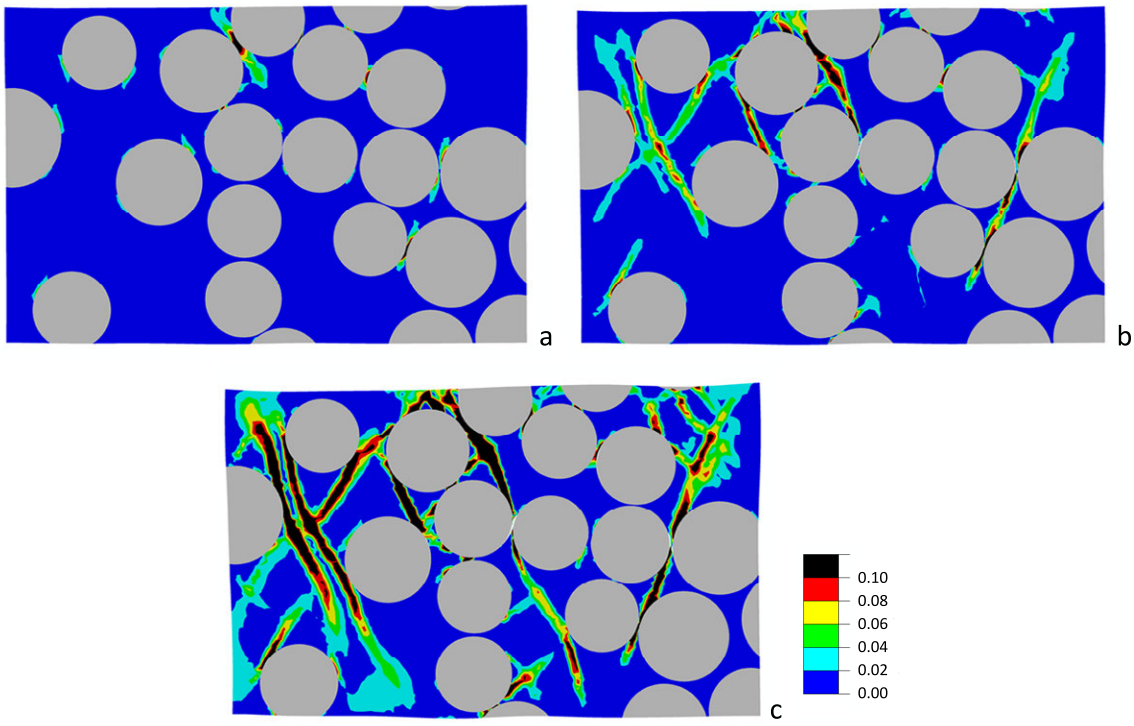

Figure 5.18: Contour plot of the effective plastic strain in the composite microstructure for the simulations of the ROI at 2000x. Loading axis is vertical and the average applied strains correspond to: (a) $\bar{\epsilon}_2 = 0.018$, (b) $\bar{\epsilon}_2 = 0.026$ and (c) $\bar{\epsilon}_2 = 0.032$

linked up the interface cracks in neighboring fibers and percolated the entire ROI. As a conclusion, the simulations confirmed that the combination of the interface crack and the matrix yielding produced the degradation of load-carrying capability and lead to the final failure of the specimen.

5.5 Concluding Remarks

The application of DIC to the analysis of the micromechanisms of deformation in fiber-reinforced composites was assessed from secondary electron micrographs obtained during mechanical tests inside the scanning electron microscope. The study was carried out using micrographs with low magnification (250x) and high magnification (2000x and 6000x). At low magnification, the fibers themselves acted as the speckle pattern and the short elastic interactions between fibers as well as the sharp strain gradients at the fiber/matrix interfaces were completely smoothed out from the strain maps. However, the long range fluctuations in strain within the ROI due to the presence of matrix-rich and fiber-rich zones were captured at this magnification. It should be noted that this information is important so as to assess the degree of fiber clustering in the composite microstructure, that has been identified as one of the dominant factors controlling the onset of damage in composites (Segurado et al., 2003). In addition, the average composite strain measured by DIC was in good agreement with the values expected from the applied load and the transverse elastic modulus of the composite.

At higher magnifications, the speckle pattern was provided by a dispersion of submicron alumina particles on the specimen surface. DIC was able to accurately capture the displacement fields throughout the ROI and the strain fields obtained with DIC qualitatively reproduce the expected pattern: strains in the fibers were much smaller than those found in the matrix. In addition, maximum strain concentrations were found in the matrix between fibers aligned in the loading direction, the applied strain being mainly accommodated by the matrix ligaments between the fibers.

Finally, the deformation of the ROI was studied by means of computational micromechanics. The real microstructure experimentally studied through *in situ* SEM

testing was replicated in a finite element model. The simulations revealed that DIC was not able to capture the average strain within each phase. It systematically underestimated the matrix strain while overestimating the fiber strain as a result of the smoothing of the sharp strain gradients at the fiber/matrix interface. However, the numerical model accurately reproduced the displacement fields obtained by DIC and the decohesion patterns experimentally observed during the compression test.

Chapter 6

Computational prediction of the failure locus

In this chapter, the failure locus of the unidirectional laminate of E-glass/MTM 57 composite under transverse normal loads and out-of-plane shear loading is computed by a computational micromechanical model of a representative volume element of the lamina. The deformation and failure mechanisms experimentally observed in the microconstituents and their mechanical properties were included in the computational model.

6.1 Introduction

Accurate and reliable failure criteria are necessary to take full advantage of the mechanical properties of advanced composites. However, the experimental assessment of the most widespread failure theories showed that many predictions differed significantly from the experimental results (particularly under multiaxial stress states involving matrix fracture and/or fiber compression) (Hinton et al., 2004). More precise regarding which particular theory is able to better reproduce the physical failure mechanisms as well as the mechanical strength were limited by the scarcity of experimental results for multiaxial stress states and by the experimental scatter. Evidently,

more experimental results will help to clarify the situation, but a fully experimental approach can be very complex to assess for multiaxial loading.

Another approach is resorting to virtual testing by means of computational micromechanics (Cox and Yang, 2006; Segurado and LLorca, 2005, 2006, 2004). This strategy is very well suited to determine the mechanical behavior of composite lamina until fracture, and it is based on the numerical simulation of a representative volume element (RVE) of the composite microstructure. Recent examples include the simulation of the fracture behavior perpendicular to the fiber of Ti/SiC composite panels at room and high temperature (González and LLorca, 2006, 2007b) or the prediction of the failure locus of a fiber-reinforced polymer lamina under transverse compression and out-of-plane shear (Totry et al., 2008a), and transverse tension and out-of-plane shear (Canal et al., 2009).

In this chapter, computational micromechanics is used to compute the failure locus of a composite lamina of E-glass/MTM57 epoxy resin, which is subjected to transverse compressive or tensile loads combined with out-of-plane shear, a biaxial stress state with highly complex experimental access. Finally, the numerical predictions for the failure locus are compared with the available experimental results and various failure criteria of composites.

6.2 Computational model

The mechanical behavior until fracture of a uniaxially reinforced composite lamina subjected to transverse tension (σ_2) and out-of-plane shear stresses perpendicular to the fibers (τ_{23}) can be obtained through the numerical analysis of a representative volume element (RVE) of the lamina (see Fig. 6.1). The RVE was a square two-dimensional section of the lamina of dimensions $L_0 \times L_0$ in the x_2x_3 plane (perpendicular to the fibers) which contained a random and homogeneous dispersion of 50 circular fibers embedded in a matrix . The fiber volume fraction within the RVE was 54%, the actual volume fraction of the experimentally studied E-glass/MTM 57 laminate. It was assumed that the lamina microstructure was given by an indefinite translation of this RVE along the x_2 and x_3 axis and, thus, the fiber positions

within the RVE kept this periodicity condition. This technique was pioneered by Brockenbrough et al. (1991), who showed that fiber shape and spatial distribution (either regular or random) modify the composite response to a large extent. Subsequent investigations focused on the minimum size of the RVE to reproduce the macroscopic behavior, which depends on the phase properties, but is usually surprisingly small (Drugan and Willis, 1996; Hine et al., 2002; Segurado and LLorca, 2002; Segurado et al., 2002; Segurado and LLorca, 2005). Nowadays it is widely accepted that accurate predictions of the elasto-plastic behavior of particle or fiber-reinforced composites can be obtained through the numerical analysis of RVE containing a few dozen reinforcements (González et al., 2004; Borbély et al., 2006; Chawla et al., 2006), particularly if periodic boundary conditions are enforced to remove the effect of free surfaces. Moreover, previous studies with similar RVEs subjected to transverse compression and shear showed that the results obtained with 30 fibers in the RVE were equivalent to those computed with 70 fibers in terms of the stress-strain curves and of the dominant failure micromechanisms (Totry et al., 2008a)

Numerical simulations of the RVE's mechanical response were carried out using the finite element method. The matrix and the fibers were automatically discretized with 6-node isoparametric modified triangles (CPE6M in Abaqus/Standard) with integration at three Gauss points and hourglass control. In addition, 4-node isoparametric interface cohesive elements (COH2D4 in Abaqus, Camanho and Dávila (2002)) were inserted along the fiber/matrix interface in each fiber to include the effect of interface decohesion. Finite element discretization was fine enough throughout the RVE to resolve the plastic shear bands in the matrix during deformation and comprised around 26000 elements and 73000 nodes.

Periodic boundary conditions were applied to the edges of the RVE to ensure continuity between neighboring RVEs. Simulations were carried out with Abaqus/Standard (Abaqus, 2010) under plane strain conditions and within the framework of the small deformations theory with the initial unstressed state as reference.

Glass fibers were modeled as linear, elastic and isotropic solids, their elastic constants were provided by the material supplier and they are compiled in Table 6.1. The epoxy matrix was represented by an isotropic, elasto-plastic solid. Its Young's mod-

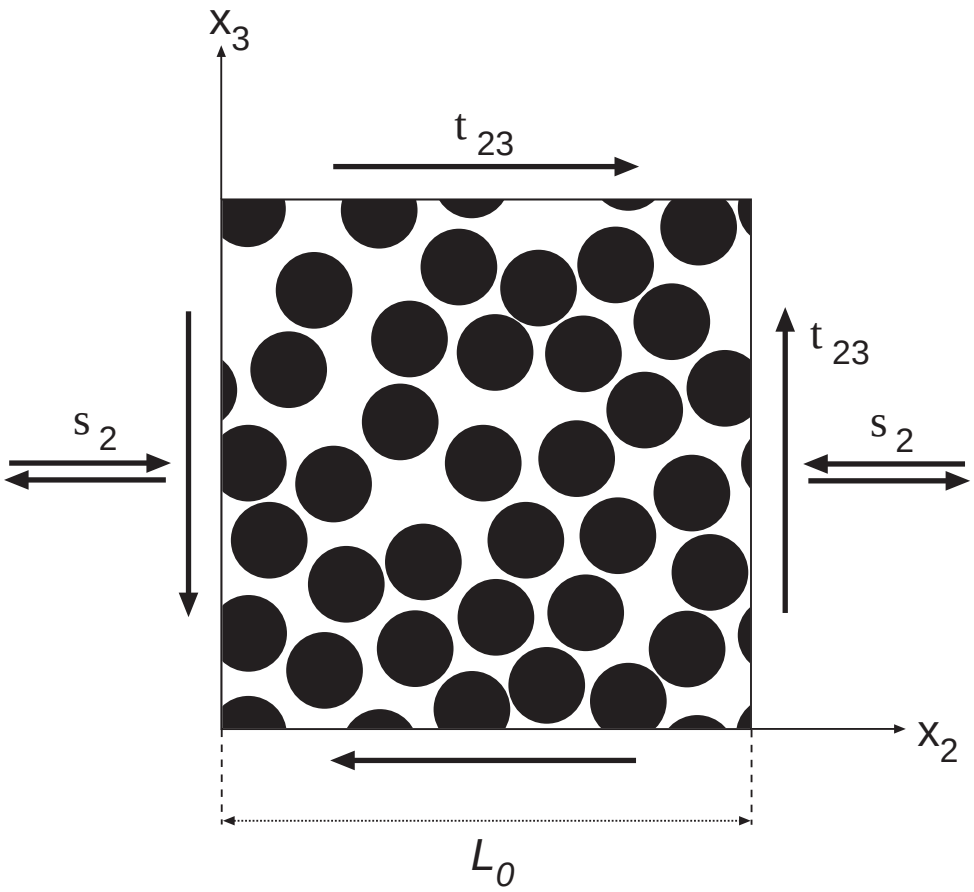

Figure 6.1: Schematic of the representative volume element of the lamina microstructure subjected to a biaxial stress state due to transverse tension and out-of-plane shear.

Table 6.1: Mechanical properties of the epoxy matrix and glass fibers employed in the numerical model.

E_m (GPa)	ν_m	E_f (GPa)	ν_f
3.5	0.35	74	0.2

ulus was experimentally determined by nanoindentation techniques and the Poisson ratio was provided by the material supplier. The elastic constants of the epoxy matrix employed in the simulations are also shown in Table 6.1. The plastic and damage of the matrix was represented by the model for quasi-brittle materials presented in Chapter 1,using a pressure sensitivity parameter of $\alpha = 0.13$ and material strengths of $\sigma_{\rm yt} = 75$MPa and $\sigma_{\rm yc} = 105$MPa as parameters in this model. The normal and shear strength employed to simulated the fiber decohesion were the same used in previous sections (N=50 and S=75 MPa). Finally, the values of the fracture energy for the matrix and the interfaces were those selected in Chapter 4 to reproduce the experimental load-CMOD curves ($G_f^{\rm interface} = 150{\rm J/m^2}$ and $G_f^{\rm matrix} = 100{\rm J/m^2}$).

6.3 Results

Uniaxial simulations

Three different fiber distributions were generated using the strategy described in the previous section. Their results were homogeneous, random and isotropic distributions of fibers in the RVE, which were statistically equivalent although the precise location of the fibers was different in each one. The stress-strain curves under uniaxial compression and pure shear are plotted together with the experimental results for the transverse compression in Fig. 6.2. The calculations were stopped after the maximum load was attained. The results for the different realizations of fibers within the RVE presented in this figure show very little scatter up to the yielding, indicating that the size of the RVE was large enough to compute the lamina strength.

The uniaxial compression of the RVEs showed an initial linear behavior which ended at compressive strains in the range of -1% to -2%. The plastic response contin-

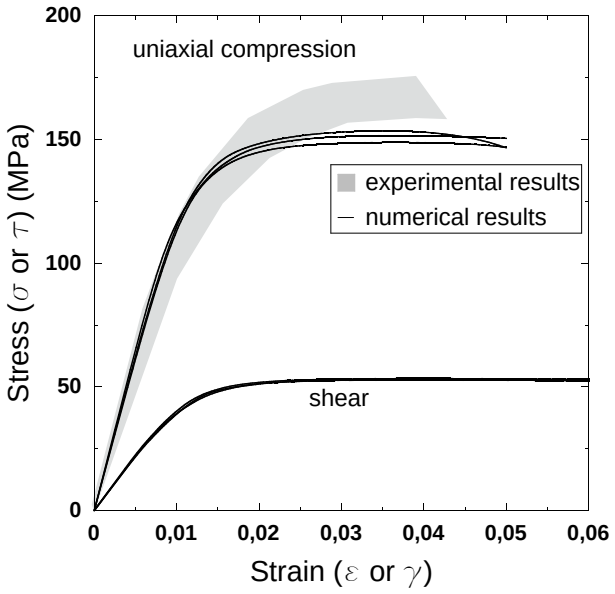

Figure 6.2: Stress-strain curves under uniaxial compression and out-of-plane shear for the RVEs. The absolute values of the stress and strain are used to plot the curves in compression.

ued with very little hardening as the localization of the plastic strain in the matrix led to the formation of numerous shear bands spread over the RVE. Further compressive deformation concentrated the plastic strain in a single shear band which percolated the RVE by the linking up of interface cracks in adjacent fibers. The RVEs loaded in uniaxial compression attained the maximum load for a compressive stress around 150MPa. The transverse compressive strength obtained through the numerical simulations was slightly lower than the experimentally obtained value (see Fig. 6.2), this mismatch could be probably caused by small inaccuracies in the experimental determination of the compressive strength of the matrix and the interface strength. The contour plot of the plastic strains in the matrix (Fig. 6.3) showed that failure took place by the propagation of a shear band in the matrix. The shear band cannot propagate though the fibers and surrounded them by breaking the interfaces, leading to slight variations in the orientation. The average orientation of the shear bands was $50^\circ \pm 4^\circ$, very close to the experimental measurements of the fracture plane in compressive specimens ($54^\circ \pm 2^\circ$, Chapter 2). It should be noted that the predictions of these numerical simulations for transverse compression were in excellent agreement with the experimental observations in terms of elastic behavior, ductility and the dominant failure mechanisms (Soden et al., 1998; Aragonés, 2007), and only small differences ($\approx 5\%$) were found in the compressive strength.

The stress-strain curve in shear are also represented in Fig. 6.2. These curves presented a wide plateau and the maximum was attained for shear strains in the range 4-6%. The analysis of the contour plot of the accumulated plastic strain in the matrix showed that failure also took place by the propagation of a dominant plastic shear band in the matrix in which most of the plastic strain was localized (Fig. 6.3).

Initially, the stress-strain curves in tension corresponding to three different RVEs are plotted in Fig. 6.4 together with the experimental results and the predictions of the embedded cell simulations performed in Chapter 4. Non-linearity appeared in the stress-strain curves for stress levels of the order of the interface normal strength (50 MPa) and the maximum stress was attained for strains in the range 2-3% providing a value of the strength ≈ 67 MPa.

Fig. 6.5 shows the deformed shape of the RVE under transverse tension load-

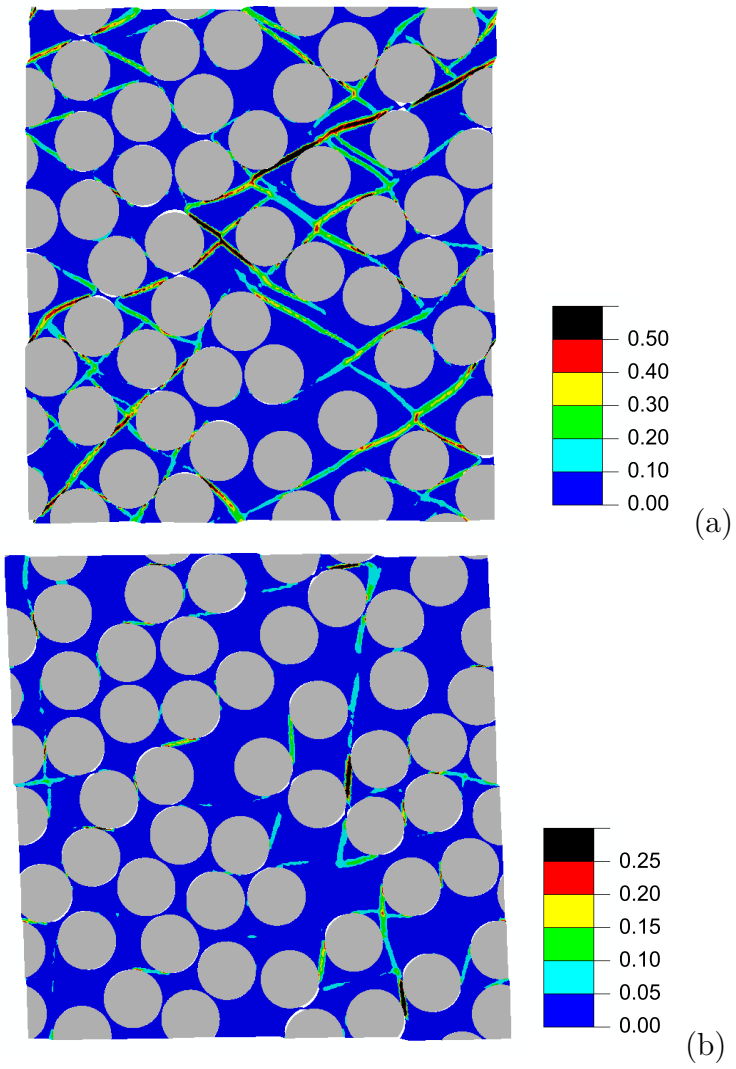

Figure 6.3: Contour plot of the accumulated plastic strain in the composite subjected to (a) uniaxial compression in the horizontal direction, (b) pure out of plane shear. The applied compressive and shear strains were 5%.

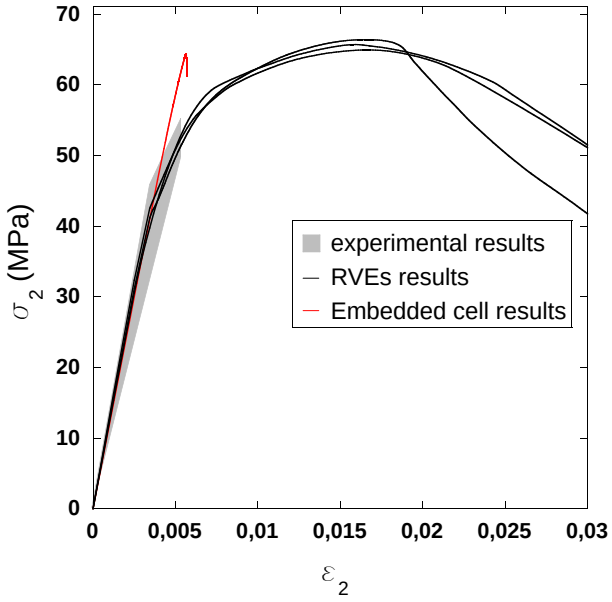

Figure 6.4: Stress-strain curves under uniaxial tension.

ing. Failure was initiated by the nucleation of interface cracks, responsible for the non-linear behavior at small strains, which grew along the interfaces. The stress concentrations at the interface crack tip promoted the failure of the matrix ligaments between debonded fibers. The damage progressed by cutting the RVE by the link-up of the interface cracks along a direction approximately perpendicular to the maximum principal stress.

It is important to notice that the behavior predicted by the RVEs was very ductile in comparison with the result of the embedded cell and the experimental measurements. This effect is caused by the periodic boundary conditions employed in the simulations. RVEs usually provide accurate predictions of the elastic-plastic behavior of the composite (Eckschlager et al., 2002; González et al., 2004). However, they fail to simulate the brittle failure of the material. Thus, a crack cutting the RVE cannot produce the sudden failure of the material when periodic boundaries are applied. Since the real material microstructure is supposed to be obtained by the infinite repetition of the RVE, a crack which crosses the unit cell from side to side will not

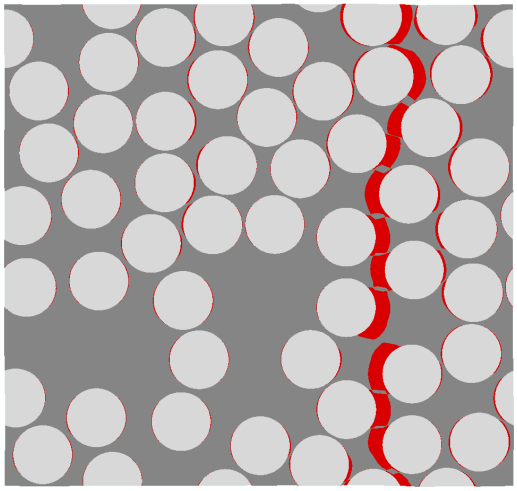

Figure 6.5: Deformed shape of the RVE subjected to uniaxial tension along the horizontal direction. The damaged interfaces have been colored in red to make evident the damage concentration. The applied tensile strain was 5%.

completely cut the real material unless the crack orientation were perfectly perpendicular to the loading direction. Therefore, when the initial point of the crack in one of the sides of the RVE does not match exactly the final point of the crack in the other side of the RVE, the periodic boundary conditions will allow the stress transfer, resulting in a ductile behavior. In spite of this, it should be noted that the maximum stress achieved in the simulations of the RVEs was equal to the stress predicted by the embedded cell approach. This fact showed that the numerical simulations with a RVE of the lamina microstructure can still be applied to obtain the strength of the material.

Multiaxial simulations

The mechanical response of the composite lamina under biaxial deformation (tension or compression perpendicular to the fibers and shear) is plotted in Fig. 6.6 in the $\sigma_2 - \tau_{23}$ stress space for different pseudo-radial loading paths characterized by the parameter δ_s/δ_n, where δ_s and δ_n stand for the imposed shear and normal displacements, respectively. The curves were initially linear indicating a fixed ratio

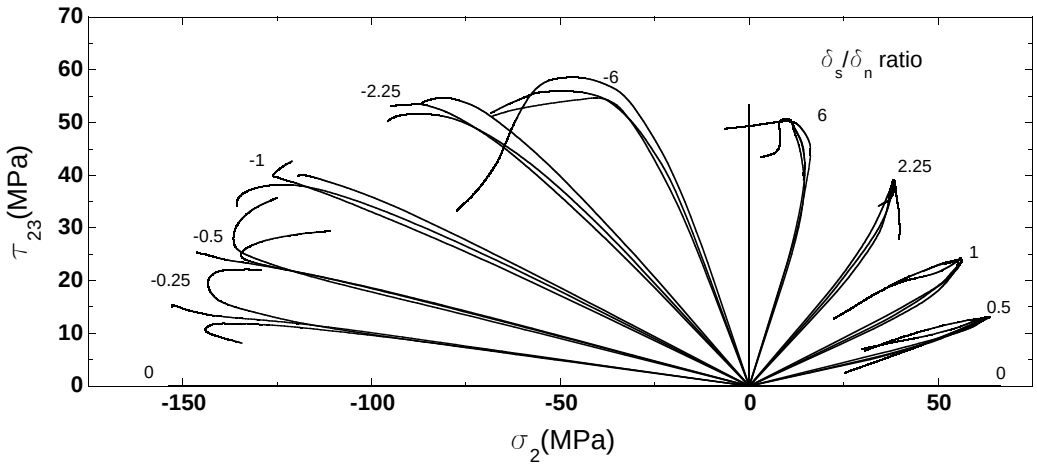

Figure 6.6: Mechanical response of the composite lamina interface under biaxial loading (transverse tension or compression stress and shear) plotted in the $\sigma_2 - \tau_{23}$ stress space.

between the shear and normal loading, at a given point the curves presented a sudden change in their slope, which marks the onset of the failure. The failure micromechanisms closely resemble those plotted in Figs. 6.3 and 6.5, they were controlled by the nucleation of interface cracks and the subsequent failure of the matrix ligaments.

The numerical simulations can be used to obtain the failure locus of the composite lamina under transverse tension and shear by linking the failure points, which are those where a sharp change of slope occurs in the $\sigma_2 - \tau_{23}$ curves in Fig. 6.6. It is interesting to compare these results with those provided by two classical failure models for composites developed by Hashin (1980) and Puck and Schürmann (2002). Hashin distinguished between fiber- and matrix-dominated fracture, and each one was further subdivided into tensile and compressive modes. Furthermore, he assumed that failure was due to the normal and tangential stresses acting on the fracture plane, which is parallel to the fibers in the case of matrix-dominated failure in tension. Taking into account that the composite lamina is isotropic in the 2-3 plane, Hashin (1980) proposed a failure criteria which can be expressed as

$$\left[\frac{\sigma_2}{Y_T}\right]^2 + \left[\frac{\tau_{23}}{S_T}\right]^2 = 1 \text{ for } \sigma_2 \geq 0 \tag{6.1}$$

$$\left[\left(\frac{Y_C}{2S_T}\right)^2 - 1\right]\frac{\sigma_2}{Y_C} + \left[\frac{\sigma_2}{2S_T}\right]^2 + \frac{\tau_{23}^2}{S_T^2} = 1 \text{ for } \sigma_2 < 0 \tag{6.2}$$

in the particular case of normal stresses perpendicular to the fibers (σ_2) combined with out of plane shears (τ_{23}) acting out of the lamina plane. In this equation, Y_T, Y_C and S_T stand for the lamina strength under transverse tension, compression and out-of-plane shear, respectively. Such strengths were obtained by means of the computational micromechanics models described above.

An analogous expression was derived by Hashin (1980) for transverse compression and in-plane shear, but the experimental data for this loading condition did not always agree with the model predictions (Hinton et al., 2004). In particular, Hashin's model did not capture the increase in shear strength in the presence of moderate compressive stresses. This limitation was attributed to the fact that Hashin's model did not determine the actual orientation of the fracture plane but assumed a quadratic interaction between the stress invariants. Puck and Schürmann (2002) improved this model by assuming that failure is caused by the normal (σ_n) and tangential (τ_t) stresses acting on the failure plane, which form an angle θ_f with the direction perpendicular to the tensile stresses. θ_f is explicitly determined for each combination of normal (σ_2) and shear (τ_{23}) stresses acting on the lamina and the corresponding failure criteria is expressed by

$$\sqrt{\left[\left(\frac{1}{Y_T} - \frac{2\mathrm{p}_{\perp\perp}(1+\mathrm{p}_{\perp\perp})}{Y_C}\right)\sigma_n(\theta_f)\right]^2 + \left[\frac{2(1+\mathrm{p}_{\perp\perp})}{Y_C}\tau_{nt}(\theta_f)\right]^2} + \\ + \frac{2\mathrm{p}_{\perp\perp}(1+\mathrm{p}_{\perp\perp})}{Y_C}\sigma_n(\theta_f) = 1 \quad \text{for } \sigma_n \geq 0 \tag{6.3}$$

$$\sqrt{\left[\frac{2(1+\mathrm{p}_{\perp\perp})}{Y_C}\tau_{nt}(\theta_f)\right]^2 + \left[\frac{2\mathrm{p}_{\perp\perp}(1+\mathrm{p}_{\perp\perp})}{Y_C}\sigma_n(\theta_f)\right]^2} + \\ + \frac{2\mathrm{p}_{\perp\perp}(1+\mathrm{p}_{\perp\perp})}{Y_C}\sigma_n(\theta_f) = 1 \quad \text{for } \sigma_n < 0 \tag{6.4}$$

Table 6.2: Failure strength under uniaxial deformation for the composite with a strong interface. Stresses are in MPa.

Y_C	S_T	Y_T
-175	55	65

with

$$\sigma_n(\theta_f) = \sigma_2 \cos^2\theta_f + 2\tau_{23} \sin\theta_f \cos\theta_f \quad (6.5)$$

$$\tau_t(\theta_f) = -\sigma_2 \sin\theta_f \cos\theta_f + \tau_{23}(\cos^2\theta_f - \sin^2\theta_f) \quad (6.6)$$

where Y_C stands for the failure stress of the lamina under transverse compression and $p_{\perp\perp}$ is the inclination parameter, which does not have a clear physical meaning and can be difficult to quantify. A value of $p_{\perp\perp} = 0.22$ was selected in this study, in the middle of the range 0.20-0.25, recommended by Puck et al. (2002) for GF/epoxy composites . The predictions of Puck's model have been largely consistent with the experimental results available for failure under transverse normal stresses and in plane shear (Hinton et al., 2004). Its validity for the particular case of normal and out of plane shear stresses is analyzed below.

The predictions of both models are based on the results of mechanical tests, which should provide the lamina strength under transverse tension, Y_T, and the lamina strength in shear, S_T, or in transverse compression, Y_C. In this study, these magnitudes were obtained from the computational micromechanical simulations, and they are presented in Table 6.2.

The predictions of the failure locus under transverse tension and out-of-plane shear provided by the phenomenological models of Hashin and Puck are compared with the numerical predictions in Fig. 6.7. Hashin's predictions overestimated the lamina strength in the regions dominated by the tension stresses, but underestimate the failure in presence of compressive loads. In addition, these predictions were based on the magnitude of S_T, the lamina strength under out-of-plane shear, which has a difficult experimental access, making very complicated the practical application of

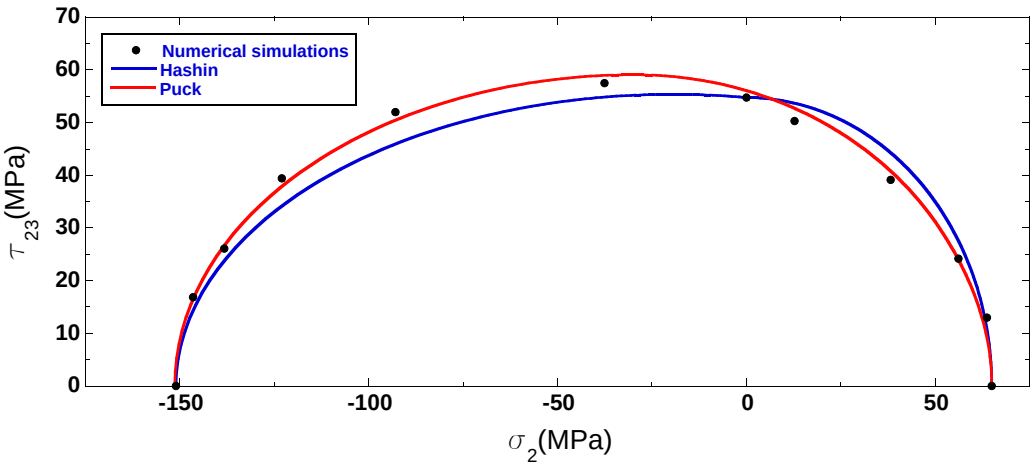

Figure 6.7: Predictions of the failure locus of the composite lamina under biaxial loading (transverse tension or compression stress and shear) plotted in the $\sigma_2 - \tau_{23}$ stress space.

this model. Therefore, these results showed that Hashin's model is not suitable to predict accurately the failure of the lamina under transverse normal stresses and out-of-plane shear. Regarding Puck's model, which is only based on the strength of the lamina under tension and compression, its predictions were in good agreement with the numerical simulations in the whole stress space. Therefore, Puck's failure criterion shown very good predictive capabilities.

6.4 Concluding Remarks

The mechanical behavior of E-glass/MTM 57 composite lamina under transverse normal stresses and out of plane shear has been studied by running numerical simulations of a RVE of the lamina microstructure. This strategy explicitly takes into account fiber and matrix spatial distribution within the lamina as well as the matrix, fiber and interfaces properties which were included in the simulations through the corresponding constitutive models. The results showed that this computational micromechanical strategy was able to reproduce the physical deformation and dam-

age mechanisms experimentally observed. The dominant failure mechanism was the interface decohesion rather than the shear yielding and the damage of the matrix. The final fracture of the lamina occurred by the link-up of the interface cracks nucleated at early stages of deformation. Finally, the failure locus under transverse normal stresses and shear was computed by subjectiong the RVE to several biaxial deformations with different displacement ratios. The results were compared with the predictions of Hashin and Puck's model of failure in composites. The results of the simulations were accurately fitted by the predictions of the Puck's model.

Chapter 7

Conclusions and future work

7.1 Conclusions

The following conclusions can be stablished:

- The macroscopic tensile and compressive behavior of an E-glass / MTM 57 unidirectional laminate has been studied in the direction perpendicular to the fibers by means of mechanical testing. It was found that under tensile loading the material showed a linear and elastic behavior until its brittle failure in a plane perpendicularly oriented to the load direction. On the contrary, under compression the material developed significant non-linear deformation before the maximum load, and the fracture was localized in a plane oriented slightly above 45° with respect to the through the thickness direction.

- The micromechanical properties which control the failure of the composite under transverse loads −strength of the matrix and fiber-matrix interfaces− were characterized by means of micromechanical testing techniques within the actual composite ply.

- The micromechanisms of deformation and damage developed in the cross section of unidirectional laminates were studied by performing compression and three-point bending tests inside the scanning electron microscope. It was found that

the main damage mechanisms were the yield and failure of the matrix and the decohesion of the fiber-matrix interfaces. Moreover, a new technique to measure the distribution of strain fields in the microstructure, based on DIC, was developed and assessed with numerical models.

- A numerical micromechanical model based on the observed damage mechanisms and the measured material properties of the constituents was developed. The model was able to reproduce the stress-strain curves (without fitting parameters), as well as the deformation and fracture mechanisms experimentally observed. In particular, the simulations of the compression tests reproduced the shear yield of the matrix and the nucleation of the decohesions, while the simulations of the tensile and three-point bending tests showed the beginning of the damage at the interfaces and the subsequent failure of the matrix ligaments.

- The micromechanical model developed was employed to predict the failure locus of the laminate under transverse loads and shear, and the results were compared with the predictions of Hashin and Puck's models. The comparisons showed that Puck's criterion is able to accurately predict the failure surface.

- The results presented in this work showed that computational micromechanics framework is able to reproduce the physical deformation and fracture mechanisms of laminates, together with the macroscopic behavior until the final failure. The work suggests the possibility of replacing (at least partially) mechanical tests by virtual ones, based on a complete characterization of the micro-constituents. These virtual tests present several advantages over the standard experimental approach, such as the full control of the composite microstructure and constituents properties, the potential to reproduce very complex stress states and the ability to carry out systematic parametric studies to optimize the composite properties.

7.2 Future work

We can mention several research lines in order to continue the present study:

7.2.1 Experimental work

- The micromechanical characterization of the composite constituents could be supplemented by a better estimation of their properties under tensile stresses. Focused ion beam could be an adequate technique to perform the experimental characterization of these properties.

- Regarding digital image correlation and its application to *in situ* tests micrographs, the available experimental information could be improved by the application of new image analysis techniques (X-DIC and 3D-DIC) and the tomographic inspection of the specimens during the tests.

- Laminates are mostly employed in multidirectional configurations which exihibit additional deformation and failure mechanisms (delamination, fiber fracture and buckling, etc). The extension of the experimental framework to study these failure mechanisms and their *in situ* microscopic observation would be of great interest.

7.2.2 Numerical model

- The use of X-FEM to deal with the fracture of the matrix and the material heterogeneities, would lead to less computationally expensive, more accurate and completely mesh-independent results.

- The current models are two-dimensional. The extension to 3D is obviously an important step. Three-dimensional models would allow a complete study of the deformation and failure of the laminate under any possible state of loads. However, due to the high computational cost of the micromechanical simulations, their extension to 3D is not feasible nowadays.

- Formulation of mesoscopic models based on the results obtained with the micromechanical simulations. These models should encompass both elastic and damage behavior.

Bibliography

Abaqus, 2010. Users' Manual, version 6.10. ABAQUS, Inc.

Aboudi, J., 1997. Micromechanical analysis of composites by method of cells. Applied Mechanical Review 42, 193–221.

Aboudi, J., 2004. The generalized method of cells and high-fidelity generalized method of cells micromechanical models. Mechanics of Advanced Materials and Structures 11, 329–66.

Amsterdam, E., De Hosson, J. T. M., Onck, P. R., 2006. Failure mechanisms of closed-cell aluminium foam under monotonic and cyclic loading. Acta Materialia 54, 4465–4472.

Anzelotti, G., Nicoletto, G., Riva, E., 2008. Mesomechanic strain analysis of twill-weave composite lamina under unidirectional in-plane tension. Composites Part A: Applied Science and Manufacturing 39, 1294 – 1301.

Aoki, S., Moriya, Y., Kishimoto, K., Schmauder, S., 1996. Finite element fracture analysis of wcco alloys. Engineering Fracture Mechanics 55, 275–287.

Aragonés, D., 2007. Fracture micromechanisms in C/epoxy composites under transverse compression. Master Thesis, Universidad Politécnica de Madrid.

Arslan, G., 2007. Sensitivity study of the drucker-prager modeling parameters in the prediction of the nonlinear response of reinforced concrete structures. Materials and Design 28, 2596–2603.

Bažant, Z. P., Oh, B. H., 1983. Crack band theory for fracture of concrete. Materials and Structures 16, 155–177.

Bažant, Z. P., Planas, J., 1998. Fracture and size effect in concrete and other quasibrittle materials. CRC Press LLC.

Berry, J. B., 1964. Brittle behavior of polymeric solids. In: Fracture process in polymeric solids. Interscience, New York.

Böhm, H., 1998. A short introduction to the basic aspects of continuum micromechanics. Institute of Lightweight Design and Structural Biomechanics (ILSB), Vienna University of Technology.

Böhm, H., Han, W., 2001. Comparisons between three-dimensional and two-dimensional statistics-based unit cell models for particle-reinforced MMCs. Modeling and Simulation in Materials Science and Engineering 9, 47–65.

Borbély, A., Kenesei, P., Biermann, H., 2006. Estimation of the effective properties of particle reinforced metal-matrix composites from microtomographic reconstructions. Acta Materialia 54, 2735–2744.

Bornert, M., Brémand, F., Doumalin, P., Dupré, J.-C., Fazzini, M., Grédiac, M., Hild, F., Mistou, S., Molimard, J., Orteu, J.-J., Robert, L., Surrel, Y., Vacher, P., Wattrisse, B., 2009. Assessment of digital image correlation measurement errors: Methodology and results. Experimental Mechanics 49, 353–370.

Brockenbrough, J. R., Suresh, S., Wienecke, H. A., 1991. Deformation of metal-matrix composites with continuous fibers: geometrical effects of fiber distribution and shape. Acta Metallurgica et Materialia 39, 735–752.

Camanho, P. P., Dávila, C. G., 2002. Mixed-mode decohesion finite elements for the simulation of delamination in composite materials. Report NASA/TM-2002-211737.

Camanho, P. P., Maimí, P., Dávila, C. G., 2007. Prediction of size effects in notched laminates using continuum damage mechanics. Composites Science and Technology 67, 2715–2727.

Campilho, R., Banea, M., Chaves, F., da Silva, L., 2011. extended finite element method for fracture characterization of adhesive joints in pure mode i. Computational Materials Science 50, 1543–1549.

Canal, L. P., González, C., Segurado, J., LLorca, J., 2011. In preparation.

Canal, L. P., Segurado, J., LLorca, J., 2009. Failure surface of epoxy-modified fiber-reinforced composites under transverse tension and out-of-plane shear. International Journal of Solids and Structures 46, 2265–2274.

Castañeda, P. P., 1991. The effective mechanical properties of nonlinear isotropic composites. Journal of the Mechanics and Physics of Solids 39, 45–71.

Castañeda, P. P., Suquet, P., 1998. Nonlinear composites. Advances in Applied Mechanics 34, 171–301.

Chawla, N., Sidhu, R. S., Ganesh, V. V., 2006. Three-dimensional visualization and microstructure-based modeling of deformation in particle-reinforced composites. Acta Materialia 54, 1541–1548.

Chen, T., 1997. Exact moduli and bounds of two-phase composites with coupled multifield linear responses. Journal of the Mechanics and Physics of Solids 45, 385–398.

Cheng, Y. T., Cheng, C. M., 2004. Scaling, dimensional analysis, and indentation measurements. Materials Science and Engineering: R 44, 91–149.

Cherry, B. W., Thomson, K. W., 1981. The fracture of highly crosslinked polymers. Journal of Material Science 16, 1925–1934.

Cox, B., Yang, Q., 2006. In quest of virtual tests for structural composites. Science 314, 1102–1107.

D7078, 2003a. D638 Standard Test Method for Tensile Properties of Plastic. ASTM International.

D7078, 2003b. D695 Standard Test Method for Compressive Properties of Rigid Plastics. ASTM International.

Dávila, C., Camanho, P. P., Rose, C. A., 2005. Failure criteria for FRP laminates. Journal of Composite Materials 39, 323–345.

Diehl, T., 2008. On using a penalty-based cohesive-zone finite element approach, part ii: Inelastic peeling of an epoxy-bonded aluminum strip. International Journal of Adhesion and Adhesives 28, 256–265.

Doumalin, P., Bornert, M., 2000. Micromechanical applications of digital image correlation technique. In: Jacquot, P., Fournier, J. (Eds.), Interferometry in Speckle Light: Theory and Application. Springer, pp. 67–74.

Drucker, D. C., Prager, W., 1952. Soil mechanics and plastic analysis or limit design. Quarterly of Applied Mathematics 10, 157–165.

Drugan, W. J., Willis, J. R., 1996. A micromechanics-based nonlocal constitutive equation and estimates of the representative volume element size for elastic composites. Journal of the Mechanics and Physics of Solids 44, 497–524.

Dugdale, D. S., 1960. Yielding of steel sheets containing slits. Journal of the Mechanics and Physics of Solids 8, 100–108.

Dvorak, G. J., 1992. Transformation field analysis of inelastic composite materials. Proceedings of the Royal Society of London A, 311–327.

Dvorak, G. J., Laws, N., 1987. Analysis of progressive matrix cracking in composite laminates ii. first ply failure. Journal of Composite Materials 21, 309–329.

Eckschlager, A., Han, W., Böhm, H. J., 2002. A unit cell model for brittle fracture of particles embedded in a ductile matrix. Computational Materials Science 25, 85–91.

Eshelby, J. D., 1957. The determination of the elastic field of an ellipsoidal inclusion and related problems. Proceedings of the Royal Society of London A252, 376–396.

Fang, X. J., Yang, Q. D., Cox, B. N., Zhou, Z. Q., 2011. An augmented cohesive zone element for arbitrary crack coalescence and bifurcation in heterogeneous materials. International Journal for Numerical Methods in Engineering.

Fowkes, F. M., 1987. Role of acidbase interfacial bonding in adhesion. Journal of Adhesion Science and Technology 1, 7–27.

Gao, Y. F., Wang, L., Bei, H., Nieh, T. G., 2011. On the shear-band direction in metallic glasses. Acta Materialia 59, 4159–4167.

Ghadbeigi, H., Pinna, C., Celotto, S., Yates, J. R., 2010. Local plastic strain evolution in a high strength dual-phase steel. Materials Science and Engineering A 527, 5026–5032.

Godara, A., Gorbatikh, L., Kalinka, G., Warrier, A., Rochez, O., Mezzo, L., Luizi, F., van Vuure, A. W., Lomov, S. V., Verpoest, I., 2010. Interfacial shear strength of a glass fiber/epoxy bonding in composites modified with carbon nanotubes. Composites Science and Technology 70, 1346–1352.

González, C., LLorca, J., 2000. A self-consistent approach to the elasto-plastic behavior of two-phase materials including damage. Journal of the Mechanics and Physics of Solids 48, 675–692.

González, C., LLorca, J., 2006. Multiscale modeling of fracture in fiber-reinforced composites. Acta Materialia 54, 4171–4181.

González, C., LLorca, J., 2007a. Mechanical behavior of unidirectional fiber-reinforced polymers under transverse compression: microscopic mechanisms and modeling. Composites Science and Technology 67, 2795–2806.

González, C., LLorca, J., 2007b. Numerical simulation of the fracture behavior of Ti/SiCcomposites between 20°C and 400°C. Metallurgical and Materials Transactions A 38, 169–179.

González, C., Segurado, J., LLorca, J., 2004. Numerical simulation of elasto-plastic deformation of composites: Evolution of stress microfields and implications for homogenization models. Journal of the Mechanics and Physics of Solids 52, 1573–1593.

Griffith, A. A., 1921. The phenomenon of rupture and flow in solids. Philosophical Transactions, Royal Society of London, Series A221, 163–198.

Gurson, A. L., 1977. Continuum theory of ductile rupture by continuum void nucleation and growth. part I: yield criteria and flow rules for porous ductile media. Journal of Engineering Materials and Technology 99, 2–15.

Gusev, A. A., 1997. Representative volume element size for elastic composites: a numerical study. Journal of the Mechanics and Physics of Solids 45, 1449–1459.

Hashin, Z., 1980. Failure criteria for unidirectional fiber composites. Journal of Applied Mechanics 47, 329–334.

Hashin, Z., Shtrikman, S., 1963. A variational approach to the theory of elastic behavior of multiphase materials. Journal of the Mechanics and Physics of Solids 11, 127–140.

Hill, R., 1952. The elastic behavior of a crystalline aggregate. Proceedings of the Royal Society of London A 65, 349–354.

Hilleborg, A., Modeer, M., Peterson, P. E., 1976. Analysis of crack formation and crack growth in concrete by means of fracture mechanics and finite elements. Cement and Concrete Research 6, 773–782.

Hine, P. J., Lusti, H. R., Gusev, A. A., 2002. Numerical simulation of the effects of volume fraction, aspect ratio and fibre length distribution on the elastic and thermoelastic properties of short fibre composites. Composites Science and Technology 62, 1445–1453.

Hinton, M. J., Soden, P. D., Kaddour, A. S., 2004. Failure criteria in fiber-reinforced polymer composites: the World Wide Failure exercise. Elsevier.

Hoa, S. V., 2009. Principles of the manufacturing of composite materials. DESTECH.

Inglis, C. E., 1913. Stresses in a plate due to the presence of cracks and sharp corners. Transactions of the Institute of Naval Architects 55, 219–241.

Irwin, G. R., 1948. Fracture dynamics. Fracturing of Metals, ASM publication, 147–166.

Jeong, H.-Y., 2002. A new yield function and a hydrostatic stress-controlled void nucleation model for porous solids with pressure-sensitive matrices. International Journal of Solids and Structures 39, 1385–1403.

Jiang, H., Xie, Y., 2011. A note on the mohr-coulomb and drucker-prager strength criteria. Mechanics Research Communications 38, 309–314.

Kachanov, L. M., 1958. Rupture time under creep conditions. Izvestija Akademii Nauk SSSR, Otdelenie Techniceskich Nauk 8, 26–31.

Kang, J., Ososkov, Y., Embury, J. D., Wilkinson, D. S., 2007. Digital image correlation studies for microscopic strain distribution and damage in dual phase steels. Scripta Materialia 56, 999–1002.

Kelly, A., Tyson, W. R., 1965. Tensile properties of fiber-reinforced metals: copper/tungsten and copper/molybdenum. Journal of the Mechanics and Physics of Solids 13, 329–350.

Kharrat, M., Carpentier, L., Chateauminois, A., Kapsa, P., 1997. Evaluation of the fibre/matrix interfacial strength of a glass fibre reinforced polymer composite using a microindentation test. Composites: Part A 28, 39–46.

Kinloch, A. J., Young, R. J., 1983. Fracture Behavior of Polymers. Elsevier Applied Science.

Kroner, E., 1958. Berechnung der elastischen konstanten des vielkristalls aus den konstanten der einkristalls. Z. Physik 151, 504–518.

Ladevèze, P., Lubineau, G., 2001. On a damage mesomodel for laminates: micro-meso relationships, possibilities and limits. Composites Science and Technology 61, 2149–2158.

Lagattu, F., Bridier, F., Villechaise, P., Brillaud, J., 2006. In-plane strain measurements on a microscopic scale by coupling digital image correlation and an in situ sem technique. Materials Characterization 56, 10–18.

Lee, J., Fenves, G. L., 1998. Plastic-damage for cyclic loading of concrete structures. Journal of Engineering Mechanics 124, 892–900.

Lemaitre, J., 1984. How to use damage mechanics. Nuclear Engineering and Design 80, 233–245.

LLorca, J., 2000. Void formation in metal matrix composites. In: Comprehensive Composite materials, Vol. 3. Metal-matrix composites. Pergamon, Amsterdam, pp. 91–115.

LLorca, J., González, C., 2011. 1st world congress on integrated computational materials engineering. The Minerals, Metals and Materials Society, Warrendale, PA.

Lomov, S., Boisse, P., Deluycker, E., Morestin, F., Vanclooster, K., Vandepitte, D., Verpoest, I., Willems, A., 2008a. Full-field strain measurements in textile deformability studies. Composites Part A: Applied Science and Manufacturing 39, 1232–1244.

Lomov, S. V., Ivanov, D. S., Verpoest, I., Zako, M., Kurashiki, T., Nakai, H., Molimard, J., Vautrin, A., 2008b. Full field strain measurements for validation of meso-fe analysis of textile composites. Composites part A 39, 1218–1231.

López-Pamiés, O., Ponte-Castañeda, P., 2006. On the overall behaviour, microstructure evolution, and macroscopic stability in reinforced rubbers at large deformations: I: Theory. Journal of the Mechanics and Physics of Solids 54, 807–830.

Lubliner, J., Oliver, J., Oller, S., Oñate, E., 1989. A plastic-damage model for concrete. International Journal of Solids and Structures 25, 299–329.

Maimí, P., Camanho, P. P., Mayugo, J. A., Dávila, C. G., 2007. A continuum damage model for composite laminates: Part I constitutive model. Mechanics of Materials 39, 897–908.

Mazars, J., 1986. A description of micro and macroscale damage of concrete structures. International Journal of Fracture 25, 729–737.

Metha, P., Monteiro, P. J. M., 1993. Concrete:Structure, properties and materials. Prentice-Hall, Englewood Cliffs, N. J.

Michel, J. C., Moulinec, H., Suquet, P., 1999. Effective properties of composite materials with periodic microstructure: a computational approach. Computational Methods in Applied Mechanical Engineering 172, 109–143.

Mittal, K. L., 1995. Adhesion measurement of films and coatings: a commentary. VSP.

Mogi, K., 1971. Fracture and flow of rocks under high triaxial compression. Journal of Geophysical Research 76, 1255–1269.

Molina-Aldareguía, J. M., Rodríguez, M., González, C., LLorca, J., 2011. An experimental and numerical study of the influence of local effects on the application of the fibre push-in test. Philosophical Magazine 91, 1293–1307.

Mori, T., Tanaka, K., 1973. Average stress in the matrix and average elastic energy of materials with misfitting inclusions. Acta Metallurgica et Materialia 21, 571–574.

Nemat-Nasser, S., Hori, M., 1999. Micromechanics: Overall properties of heterogeneous materials. North-Holland.

Ogihara, S., Koyanagi, J., 2010. Investigation of combined stress state failure criterion for glass fiber/epoxy interface by the cruciform specimen method. Composites Science and Technology 70, 143–150.

Oliver, J., 1989. A consistent characteristic length for smeared cracking models. International Journal for Numerical Methods in Engineering 28, 461–474.

Oliver, W. C., Pharr, G. M., 1992. An improved technique for determining hardness and elastic modulus using load and displacement sensing indentation experiments. Journal of Materials Research 7, 1564–1583.

Orowan, E., 1955. Energy criterion of fracture. Welding Journal 34, 1575–1605.

Patrick, R. L., 1973. The use of scanning electron microscopy. In: Treatise on adhesion and adhesives. Dekker, New York.

Peters, W. H., Ranson, W. F., 1982. Digital imaging techniques in experimental stress analysis. Optical Engineering 21, 427–431.

Pettermann, H., Plankensteiner, A., Böhm, H., Rammerstorfer, F., 1999. A thermo-elasto-plastic constitutive law for inhomogeneous materials based on an incremental mori-tanaka approach. Computers and Structures 71, 197–214.

Pettermann, H., Suresh, S., 2000. A comprehensive unit cell model: a study of coupled effects in piezoelectric 13 composites. International Journal of Solids and Structures 37, 5447–5464.

Pietruszczak, S., Mroz, Z., 1981. Finite element analysis of deformation of strain-softening materials. International Journal for Numerical Methods in Engineering 17, 327–334.

Pinho, S. T., Iannucci, L., Robinson, P., 2006. Physically-based failure models and criteria for laminated fibre-reinforced composites with emphasis on fibre-kinking. Part I: development. Composites: Part A 37, 63–73.

Planas, J., Elices, M., Guinea, G., Gómez, F. J., Cendón, D. A., Arbilla, I., 2003. Generalizations and specializations of cohesive crack models. Engineering Fracture Mechanics 70, 1759–1776.

Puck, A., Kopp, J., Knops, M., 2002. Guidelines for the determination of the parameters in puck's action plane strength criterion. Composites Science and Technology 62, 371–378.

Puck, A., Schürmann, H., 2002. Failure analysis of FRP laminates by means of physically based phenomenological models. Composites Science and Technology 62, 1633–1662.

Quinson, R., Perez, J., Rink, M., Pavan, A., 1997. Yield criteria for amorphous glassy polymers. Journal of Materials Science 32, 1371–1379.

Rabotnov, Y. N., 1968. Creep rupture. In: 12th International Congress of Applied Mechanics. Stanford.

Réthoré, J., Tinnes, J.-P., Roux, S., Buffière, J.-Y., Hild, F., 2008. Extended three-dimensional digital image correlation (X3D-DIC). Comptes Rendus Mécanique 336, 643–649.

Ridruejo, A., González, C., LLorca, J., 2011. Micromechanisms of deformation and fracture of polypropylene nonwoven fabrics. International Journal of Solids and Structures 48, 153–162.

Rodríguez, M., Molina-Aldareguía, J. M., González, C., LLorca, J., 2011. In preparation.

Rudnicki, J. W., Rice, J. R., 1975. Conditions for the localization of deformation in pressure-sensitive dilatant materials. Journal of the Mechanics and Physics of Solids 23, 371–394.

Sancho, J. M., Planas, J., Cendón, D. A., Reyes, E., Gálvez, J. C., 2007. An embedded crack model for finite element analysis of concrete fracture. Engineering Fracture Mechanics 74, 75–86.

Sautter, M., Dietrich, C., Poech, M., Schmauder, S., Fischmeister, H., 1993. Finite element modelling of a transverse-loaded fibre composite: Effects of section size and net density 1 (Computational Materials Science), 225–233.

Segurado, J., González, C., LLorca, J., 2003. A numerical investigation of the effect of particle clustering on the mechanical properties of composites. Acta Materialia 51, 2355–2369.

Segurado, J., LLorca, J., 2002. A numerical approximation to the elastic properties of sphere-reinforced composites. Journal of the Mechanics and Physics of Solids 50, 2107–2121.

Segurado, J., LLorca, J., 2004. A new three-dimensional interface finite element to simulate fracture in composites. International Journal of Solids and Structures 41, 2977–2993.

Segurado, J., LLorca, J., 2005. A computational micromechanics study of the effect of interface decohesion on the mechanical behavior of composites. Acta materialia 53, 4931–4942.

Segurado, J., LLorca, J., 2006. Computational micromechanics of composites: the effect of particle spatial distribution. Mechanics of Materials 38, 873–883.

Segurado, J., LLorca, J., González, C., 2002. On the accuracy of mean-field approaches to simulate the plastic deformation of composites. Scripta Materialia 46, 525–529.

Smits, A., Hemelrijck, D. V., 2005. Digital image correlation results on beam and cruciform specimens. Tech. rep., OPTIMAT BLADES.

Soden, P. D., Hinton, M. J., Kaddour, A. S., 1998. Lamina properties, lay-up configurations and loading conditions for a range of fibre-reinforced composite laminates. Composites Science and Technology 58, 1011–1022.

Sun, L. Z., Ju, J. W., Liu, H. T., 2003. Elastoplastic modeling of metal matrix composites with evolutionary particle debonding. Mechanics of Materials 35, 559–569.

Sutton, M., Orteu, J., Schreier, H., 2009. Image correlation for shape, motion and deformation measurements: basic concepts, theory and application. Springer Verlag.

T. C. Chu, W. F. Ranson, M. A. S., Peters, W. H., 1985. Applications of digital-image-correlation techniques to experimental mechanics. Experimental Mechanics 25, 232–244.

t. J. Vaughan, 2011. Micromechanical modelling of damage and failure in fiber reinforced composites under loading in the transverse plane, Ph.D. thesis. University of Limerick.

Torquato, S., 1991. Random heterogeneous media: Microstructure and improved bounds on effective properties. Applied Mechanics Reviews 44, 37–76.

Torquato, S., 2001. Random heterogeneous materials. Springer.

Totry, E., González, C., LLorca, J., 2008a. Failure locus of fiber-reinforced composites under transverse compression and out-of-plane shear. Composites Science and Technology 68, 829–839.

Totry, E., González, C., LLorca, J., 2008b. Influence of the loading path on the strength of fiber-reinforced composites subjected to transverse compression and shear. International Journal of Solids and Structures 45, 1663–1675.

Totry, E., González, C., LLorca, J., 2008c. Prediction of the failure locus of c/peek composites under transverse compression and longitudinal shear through computational micromechanics. Composites Science and Technology 68, 3128–3136.

Totry, E., González, C., LLorca, J., Molina-Aldareguía, J. M., 2009. Mechanisms of shear deformation in fiber-reinforced polymers: Experiments and simulations. International Journal of Fracture 158, 197–209.

Totry, E., Molina-Aldareguía, J. M., González, C., LLorca, J., 2010. Effect of fiber, matrix and interface properties on the in-plane shear deformation of carbon-fiber reinforced composites. Composites Science and Technology 70, 970–980.

Trias, D., 2005. Analysis and Simulation of Transverse Random Fracture of Long Fiber Reinforced Composites, Ph. D. thesis. University of Girona.

Tvergaard, V., Needleman, A., 1984. Analysis of the cup-cone fracture in a round tensile bar. Acta Metallurgica 32, 157–169.

Vendroux, G., Knauss, W. G., 1998. Submicron deformation field measurements: Part 2. improved digital image correlation. Experimental Mechanics 38, 86–92.

Wang, Y., Cuitiño, A. M., 2002. Full-field measurements of heterogeneous deformation patterns on polymeric foams using digital image correlation. International Journal of Solids and Structures 39, 3777–3796.

Wright, P., Fu, X., Sinclair, I., Spearing, S. M., 2008. Ultra high resolution computed tomography of damage in notched carbon fiber-epoxy composites. Journal of Composite Materials 42, 1993–2002.

Wulf, J., Steinkopff, T., Fishmeister, H., 1996. FE-simulation of crack paths in the real microstructure of an Al(6061)/SiC composite. Acta materialia 44, 1765–1779.

Xia, Z., Curtin, W., Peters, P., 2001. Multiscale modeling of failure in metal matrix composites. Acta Materialia 49, 273–287.

Y. T. Kim, M. J. Lee, B. C. L., 2011. Simulation of adhesive joints using the superimposed finite element method and a cohesive zone model. International Journal of Adhesion and Adhesives 31, 357–362.

Yamini, S., Young, R., 1980. The mechanical properties of epoxy resins. part i: mechanism of plastic deformation. Journal of Material Science 15, 1814–1822.

Yang, Q., Tang, L., Chen., H., 1994. Self-consistent finite element method: A new method of predicting effective properties of inclusion media. Finite Elements in Analysis and Design 17, 247–257.

Yee, A. F., Du, J., Thouless, M. D., 2000. Toughening of epoxies. In: Polymer Blends. John Wiley & Sons, Inc., pp. 225–267.

Yongqi, S., Corletto, C., Bradley, W. L., Tian, J., 1996. Direct measurement of microscopic strain distribution near a crack tip. Experimental Mechanics 36, 193–198.

Young, R. J., Thongpin, C., Stanford, J. L., Lovell, P. A., 2001. Fragmentation analysis of glass fibres in model composites through the use of raman spectroscopy. Composites: Part A 32, 253–269.

Zhandarov, S., Mäder, E., 2005. Characterization of fiber matrix interface strength: applicability of different tests, approaches and parameters. Composites Science and Technology 65, 149–160.

Zhang, L., P. Cao, K. R., 2010. Evaluation of rock strength criteria for wellbore stability analysis. International Journal of Rock Mechanics and Mining Sciences 47, 1304–1316.

Zhao, Y. H., Weng, G. J., 1996. Plasticity of a two-phase composite with partially debonded inclusions. International Journal of Plasticity 12, 781–804.

Zhou, X.-F., Nairn, J. A., Wagner, H. D., 1999. Fiber-matrix adhesion from the single-fiber composite test:nucleation of interfacial debonding. Composites: Part A 30, 1387–1400.

Zhou, X.-F., Wagner, H. D., Nutt, S. R., 2001. Interfacial properties of polymer composites measured by push-out and fragmentation tests. Composites: Part A 32, 1543–1551.

List of Figures

LIST OF FIGURES